in vivo patient dose verification of volumetric modulated arc therapy including stereotactic body radiation treatment applications using portal dose images

by

Peter Michael McCowan

A thesis submitted to the Faculty of Graduate Studies of

The University of Manitoba

in partial fulfillment of the requirements for the degree of

DOCTOR OF PHILOSOPHY

Department of Physics & Astronomy

University of Manitoba

Winnipeg, Canada

ACKNOWLEDGEMENTS

This work would not have been completed without financial support. I have received funding for my research from the CancerCare Manitoba Foundation, the University of Manitoba's Faculty of Science, and the University of Manitoba's Faculty of Graduate Studies.

I would like to thank my advisory committee: Dr. John Lewis, Dr. Francis Lin, Dr. Daniel Rickey, Dr. Lawrence Ryner, and Dr. Gabriel Thomas for their help and support over past five years. More importantly, I would like to thank my supervisor Dr. Boyd McCurdy for introducing me to the field of radiation physics as well as his enthusiasm, dedication, insight, friendship, and leadership during the course of my PhD studies.

I would like to thank some CCMB staff: Ken Allen and Chris Dyke from nuclear electronics, Bob Miller and Todd Boyer from the fabrication shop, staff physicists Dr. Eric vanUytven, Dr. Ryan Rivest, and Dr. Dave Sasaki for their help in acquisition, analysis, and trouble-shooting.

I would like to thank the past and present students whom I've had the chance to meet during the course of my PhD: Dr. Jorge Alpuche, Dr. Ganiyu Asuni, Heather Champion, Tamar Chighvinadze, Dr. Krista Chytyk-Praznik, Hongyan Sun, and Troy Teo. A special thanks as well to Timothy Van Beek for his intelligent contributions and code writing expertise.

I would like to very much thank my parents, Rudi and Janet, and my brothers Alexander, Angus, and James for their support and encouragement over the years. I would like to especially thank my fiancée Jennifer Vancuren for her love, understanding, patience and overall amazingness over these past years. Finally, a thank you to my good friends Rylan Page, Devyn Rolke, Jason Senyk, and Chad Slobodian for keeping me level and sane throughout.

ABSTRACT

The complexity of radiation therapy delivery has increased over the years due to advancements in computing and technical innovation. A system of dose delivery verification has the potential to catch treatment errors and therefore improve patient safety. The goal of this thesis was to create a portal image-based *in vivo* dose reconstruction model for volumetric modulated arc therapy (VMAT) deliveries, specifically for stereotactic body radiation therapy (SBRT). This model-based approach should be robust and feasible within a clinical setting. VMAT involves the modulation of dose rate, gantry speed, and aperture shaping while the treatment gantry (i.e., x-ray beam) rotates about the patient. In this work, portal images were acquired using an amorphous silicon electronic portal imaging device (a-Si EPID).

A geometrical characterization of the linear accelerator (linac) during VMAT delivery was performed. The effect of gravitational sag on the EPID imager and EPID support arm was experimentally determined to be a reproducible effect and thus correctable. The angular accuracy of the EPID images acquired during a VMAT arc was investigated and found to be erroneous by as much as 3°. An angle adjustment method was determined which improves each EPID's angular accuracy to within ±1° of the true physical angle. An accurate EPID image angle improves the accuracy of our *in vivo* dose reconstruction.

An *in vivo* patient dose reconstruction model for conventional intensity modulated radiation therapy and, more recently, VMAT has been developed. This thesis focuses on

adapting the model for SBRT-VMAT treatments. SBRT delivers large doses over fewer fractions than conventional radiotherapy, therefore, any error during an SBRT delivery will have a greater impact on the patient. This strongly encourages an *in vivo* dosimetry verification system. In this work, a robust, model-based SBRT-VMAT dose reconstruction verification system using EPID images was developed. This was validated using seven different patient plans delivered to an anthropomorphic phantom as well as two plans delivered to patients. The model was determined to be clinically feasible.

Each EPID image saved by the clinical computer is the average of an integral number of frames. The accuracy of a 3D *in vivo* dose reconstruction, using all the EPID images acquired during treatment, is sensitive to the chosen frame averaging per EPID image: the greater the frame averaging, the larger the reconstruction error. However, the more EPID images, the greater the calculation time. Optimization of the EPID frame averaging number as a function of average linac gantry speed and dose per fraction were determined.

The EPID-based *in vivo* dose reconstruction model for SBRT-VMAT developed here was determined to be robust, accurate, and clinically feasible as long as adjustments were made in order to correct for EPID image geometrical errors and frame-averaging errors.

TABLE OF CONTENTS

LIST OF TABLES

LIST OF FIGURES

CHAPTER EIGHT (APPENDIX)

LIST OF COPYRIGHTED MATERIAL

CONTRIBUTION TO SCIENCE

The following is a brief summary of the scientific contributions of each chapter from this thesis.

In Chapter Three, a measurement-based approach was performed in order to characterize the EPID's support arm 'flex' or 'sag' due to gravity. This effect was never investigated prior to this study. The linear accelerator gantry and attached EPID support arm have a significant mass which affects the EPID's positional accuracy, thus affecting overall dose reconstructions using these images. For the newer Varian linac's equipped with an E-arm, it was found that the flex was a negligible effect in the x-axis of the EPID while the y-axis exhibited roughly a 1mm maximum shift. This work was awarded a 2nd place poster prize at the Canadian Organization of Medical Physicists (COMP) annual meeting in 2010.

Every EPID image acquired during beam-on delivery has an associated header storing pertinent real-time delivery information, including the image's gantry angle. No significant analyses were performed in order to establish the accuracy of this angle. In Chapter Four, an in-depth characterization of the linac's gantry angle accuracy was performed and compared to the accuracy of the EPID image header's angle. Furthermore, additional methods were investigated in order to adjust the header angle to be more accurate to the true physical gantry angle. This was important in order to accurately reconstruct the 3D patient dose from a set of EPID images acquired circularly about the patient. The linac's gantry analog potentiometer, which is accessible during treatment, was accurately verified using an in-house constructed angle phantom as well as a digital rotary encoder. It was also found that EPID image header angles could be incorrect by

as much as ±3° with respect to the gantry potentiometer. It was found that a simple box-smoothing function applied to the vector of header angle data per arc allowed for EPID header angle adjustments to always be within ±1° with respect to the potentiometer. Similarly, a treatment console log file could be used to correct the angle to within ±0.2°, but was not easily accessible.

In Chapter Five, a SBRT linac beam model was developed in order to predict both the 3D patient dose as well as portal images. This work was based on the work of Chytyk *et al*. (2009, 2013). This involved Monte Carlo modeling of an SBRT linac beam and validation of the simulation results with water tank measurements. The prediction model was important in creating an EPID image-based *in vivo* patient dose reconstruction model for SBRT-VMAT delivery. The VMAT reconstruction algorithm was based on our work performed roughly the same time (vanUytven *et al*., 2015). The reconstruction model also incorporated the EPID flex and angle corrections established from Chapters 3 and 4 respectively. The model was rigorously tested using clinical patient plans delivered to an anthropomorphic phantom as well as two plans with the patient present. Comparisons with the Eclipse treatment planning system were carried out and provided clinically acceptable χ-test pass rates using a 3%/3mm criterion. This work was awarded 3rd place at the COMP annual meeting's prestigious J.R. Cunningham Young Investigators Symposium in 2014.

In Chapter Five, a stringent 2%/2mm criterion for the χ-tests was also used which provided in-depth information on the accuracy of our reconstruction algorithm in order to determine any errors. One reason for significantly lower pass rates at 2%/2mm was the

difference between our dose calculation algorithm and Eclipse's. These are both reported in detail in the Appendix of this thesis. Furthermore, a significant error was also introduced into our reconstruction result if the frame averaging of each EPID image was set too high. This led to an investigation into the optimization of the frame averaging number as a function of the treatment type.

In Chapter Six, an in-depth analysis was performed in order to optimize the frame averaging number per EPID image as a function of the linac's average gantry speed. Prior to treatment, the user can input an integer number of frames to be averaged for every acquired EPID image. Varying treatments of regular VMAT and SBRT-VMAT plans were analyzed. Single EPID frames were acquired using a designated frame-grabber package and then manually frame-averaged to create image data sets of varying frame average numbers. The single frame-averaged EPID reconstruction, considered to be the most accurate, was compared to the higher frame-averaged EPID reconstructions for every plan in order to eliminate the algorithmic differences determined from Chapter five. A frame-average optimization curve, which could be used to choose the optimal frame average number as a function of average gantry speed, dose per fraction, and/or disease site, was determined.

CHAPTER ONE: RATIONALE

1.1 OVERVIEW OF RADIATION THERAPY

Cancer is the leading cause of death in Canada. At present, roughly 2 in 5 Canadians will develop cancer in their lifetime, and about 1 in 4 Canadians will die of cancer. In 2014, the Canadian Cancer Society estimated that nearly 190,000 Canadians will develop cancer, while 76,000 will die of cancer[1].

The three main types of therapies used to treat cancer are surgery, radiation therapy, and chemotherapy (i.e. cytotoxic drugs). Roughly 60% of all diagnosed cancers are treated with radiation therapy either by itself or in combination with other therapies. Treatments of varying combination and degree are created in order to prevent further growth of the cancer, or, if possible, to kill the cancer. The treatment regimen is dependent on the severity and biology of cancer and the medical condition of the patient.

The overall goal of radiation therapy is to maximize a dose of radiation to the tumour while minimizing the dose to the surrounding normal healthy tissue. Dose delivered to normal tissues can result in future complications such as lung pneumonitis, spinal cord injury, loss of organ function, etc. A typical radiation therapy treatment course consists of daily treatments over 5 to 8 weeks, delivering roughly 1 to 2 Gy (Gy = Gray = Joule/kg) per day, 5 times a week. One treatment delivery is termed a ‘fraction’ since it delivers only a fraction of the total prescribed dose. The approach of fractionating the treatment course is

based on radiobiological advantages. The regimen can also be 'hypofractionated' where larger doses are delivered over fewer fractions, which is typically done in a specialized technique known as stereotactic body radiation therapy (SBRT). This technique usually involves 1-8 fractions of 6-20 Gy per fraction.

In order to develop a customized radiation treatment plan, one must have a three-dimensional (3D) map of the patient's anatomy. Prior to the 1970's patient planning was carried out by contouring a 2D transverse slice of the patient shape and size onto water phantoms. Dosimetry within the patient was then estimated from dose-to-water look up tables. After the 1970's the development of magnetic resonance imaging (MRI) and computed tomography (CT) greatly improved the anatomical diagnosis of the patient. MRI has superior soft tissue contrast while CT has excellent bony anatomy contrast. Presently, one or both of these imaging modalities are used in order to diagnose and delineate the diseased tissue or tumour and the surrounding organs-at-risk (OARs). The resolution and contrast of these modalities has improved with the advancements in computer and imaging technologies. Furthermore, the CT patient dataset is also used to accurately predict the dose delivered to the tumour and surrounding area. The CT dataset can be converted into a 3D map of densities (physical or electron) which are needed to accurately calculate radiation doses delivered to the patient by the radiation treatment beams. The patient's anatomical map is also used to optimize the planned treatment delivery in order to spare OARs without a significant loss of tumour dose. This can be achieved by collimating the treatment beams to the shape of the tumour and angling the beams to avoid OARs as much as possible, a method known as 3D conformal radiation therapy (3DCRT). This is usually performed using a set of

3-6 beams entering from various angles about the patient, all directed at the tumour. In order to compensate for the differing shapes and sizes of patients and tumours, beam modifying devices such as wedges or tissue compensators are sometimes inserted into the beam path to help ensure uniform and conformal dose delivery. For 3DCRT, which is still used widely today for simple treatments, a human operator optimizes the dose distribution in the patient.

With improvements in both computer and medical linear accelerator (linac) technology, specifically the linac's beam shaping multi-leaf collimators (MLCs), advancements were made in the precision and automation of 3D-CRT delivery. In the 1990's intensity modulated radiation therapy (IMRT) was developed[2-6] and was widely implemented in the 2000's. The technique uses MLCs to modulate the fluence of the beams entering the patient. It uses a set of 5 – 9 beams, MLC shaping, and fluence modulation in order to deliver a more conformal dose to tumours and limit dose to OARs moreso than can be achieved by 3DCRT. Instead of manual optimization, computerized algorithms automatically optimize the fluence patterns of each beam. IMRT fields typically deliver high dose gradients in order to achieve a dose to the patient that conforms to the shape of the tumour, highlighting the need for accurate patient positioning during delivery. The CT dataset is used by the radiation oncologist to delineate the tumour and normal tissues. Dose objectives and dose constraints are set for the delineated structures identifying the target tissues and the OARs. The treatment planning system uses this information to derive an optimal fluence pattern that will be delivered by a set of treatment unit parameters such as gantry angles, MLC positions, dose rate, etc.

In 2008, Karl Otto derived a feasible optimization method for the delivery of IMRT beams during continuous gantry rotation, now called volumetric modulated arc therapy (VMAT)[7]. His approach broke the 360 degree full gantry rotation into a series of hundreds of 'control points' representing separate angles, and used a 'coarse-to-fine' technique to optimize the dose rate and MLC aperture position. This method has proven to be a highly efficient adaptation of IMRT delivery and is presently used for the majority of IMRT treatments in Canada. This high adoption rate is because it takes less time to deliver and has comparable if not better dosimetric coverage than static IMRT[8-11].

1.2 DOSIMETRIC ACCURACY

In 1976 the International Commission on Radiation Units and Measurements (ICRU) stated that the maximum acceptable dose uncertainty in radiation therapy delivery is ± 5%. This was based on what was achievable during treatment and what was perceived as most effective[12]. The error in dose could be due to, but not limited to, patient misalignment or improper linac beam quality assurance (QA). More recent estimates of required accuracy, based on radiobiological considerations, are in the 3-4% range, as described below.

The radiobiological effect of radiation on cancerous and normal tissues is approximated by sigmoidal curves like the ones shown in Fig. 1.1 using terms of tumour control probability (TCP) and normal tissue complication probability (NTCP). These terms describe the relationship between the delivered radiation dose and the chance of tumour control (in the

case of TCP) and the chance of a complication occurring (in the case of NTCP). These relationships can be estimated for specific tissues from clinical and experimental observations. In general, a higher dose delivered to the tumour results in a higher probability for tumour control, but when a higher dose is delivered to a neighbouring organ, it results in a higher probability of causing a complication in that organ. For successful treatment one wants to maximize the tumour control and minimize the normal tissue complication – in other words deliver a large dose to the tumour while delivering only low doses to the surrounding tissues. For the TCP, the relative steepness of its slope is defined as the required dose needed to increase the TCP from 50% to 75% control probability denoted as $\Delta 50/75_{TCP}$. The NTCP uses a similar definition for curve steepness, defined as $\Delta 25/50_{NTCP}$. For planning one prefers a large value for the $\Delta 25/50_{NTCP}$ and a small value for the $\Delta 50/75_{TCP}$, i.e., a small dose increment greatly improves the TCP and has a minimal effect on the NTCP. From these definitions many studies have been performed on how the dose uncertainty affects the TCP and NTCP and in general found that limiting the maximum dose uncertainty to around 3% results in a maximum TCP and minimal NTCP[13-15]. Although these uncertainties were determined prior to the introduction of complex deliveries such as IMRT and VMAT, Thwaites *et al.* (and references within) determined that they still are applicable to present day technologies and may only require a higher precision when dealing with more complex hypofractionated treatments[15]. Based on this literature, a baseline for achievable dosimetric accuracy of ≤ 3% for radiation therapy and therefore also radiation therapy verification was defined.

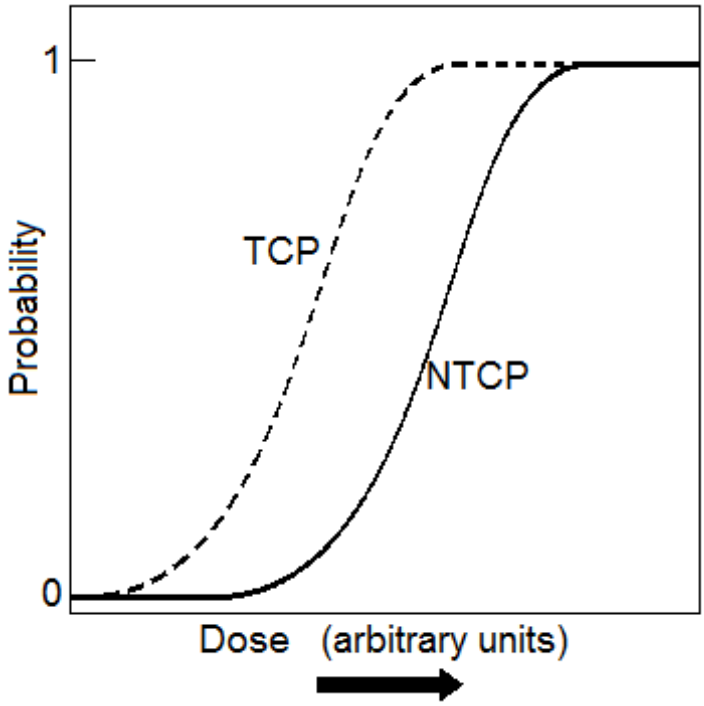

Fig.1.1 [TCP vs NTCP]: an example of TCP and NTCP sigmoidal probability curves plotted as a function of radiation dose.

1.3 ACCIDENTS AND ERRORS IN RADIATION THERAPY

Accidents resulting in an overdose or under-dose to patients have occurred throughout the history of radiation therapy delivery. For example, incorrect decay curves were used to calibrate a Cobalt-60 linac resulting in an overdosing of 426 patients[17]. In another case, a Therac-25, one of the first computer-controlled linacs, exhibited multiple software failures and non-responsive interlocks which resulted in substantial overdosing to several patients, causing serious injury and three deaths[18]. In 1990, a clinic in Zaragoza, Spain improperly calibrated an electron accelerator that went unchecked for over a year and resulted in the deaths of 25 patients[19].

Even though present day commercial linacs come equipped with much improved error-catching technologies, serious accidents continue to be reported. In 2001, a clinic in Poland delivering breast radiation therapy with a linac, overdosed 5 patients who all required skin grafts afterwards[20]. In 2005, a clinic in New York overdosed a patient due to improper MLC data transfer by the planning software. Only three erroneous fractions were delivered, but the patient experienced serious suffering for a year and eventually died[21].

With more complex and hypofractionated treatments, like SBRT, the impact on the patient from any delivery error is magnified due to the higher doses delivered per fraction. A Florida clinic overdosed 77 SBRT patients between 2004 and 2005 due to a calibration error on the linac[22]. Identical types of errors involving the incorrect measuring of linac output factors in Toulouse, France affected 145 SBRT patients between 2006 and 2007[23]. More recently, between 2004 and 2009, 152 SBRT patients at a clinic in Springfield, Missouri were over dosed by 50% due to a linac commissioning error[24].

All of these accidents could have been avoided if an independent patient dose verification program was in place. Even after a measurement-based, pre-treatment, quality assurance or QA measurement (the current standard QA approach for IMRT/VMAT treatments), there may still be problems, albeit very rare, due to an unanticipated delivery error or malfunctioning interlocks[25]. Significant weight loss/gain or tumour shrinkage/growth within the patient during the course of radiotherapy can also result in dosimetric errors. An *in vivo* dosimetric verification of the delivered radiation is the only way to positively confirm the

dose delivered to the patient after each fraction. The term *in vivo* dosimetry is commonly used in this field to describe a measured estimate of delivered dose within the living patient.

1.4 *in vivo* DOSE VERIFICATION FOR RADIATION THERAPY

It is evident from the above discussions that any clinic would benefit greatly from a dose verification routine for all patients treated with radiation therapy. This not only provides the clinic more consistently correct (and therefore better) treatment, but also increases patient safety. Dose verification, specifically using a linac's amorphous silicon electronic portal imaging device (EPID), can measure the entire treatment delivery and catch significant errors[25,26]. In 2010, Mans *et al*. reported the results of a large *in vivo* EPID verification project where 17 of 4337 patients were found to have serious delivery errors requiring intervention[25]. Recently, it was demonstrated that *in vivo* dose verification is one of the most important quality control checks[27] and is also recommended by several radiotherapy organizations to increase patient safety[28].

1.5 HYPOTHESIS

Use transmission EPID images acquired during SBRT-VMAT treatments in order to reconstruct and verify the *in vivo* dose delivered to the patient.

REEFERENCES

1. Canadian Cancer Society: http://www.cancer.ca/~/media/cancer.ca/cw/cancer%20 information/cancer%20101/canadian%20cancer%20statistics/canadian-cancer-statistics-2014-en.pdf.
2. Webb, S., *Optimization of conformal radiotherapy dose distributions by simulated annealing*, Phys Med Biol, 1989, **34**, p.1349-1370.
3. Bortfeld, T., Burkelbach, J., Boesecke, R., and Schlegel, W., *Methods of image reconstruction from projections applied to conformation radiotherapy*, Phys Med Biol, 1990, **35**, p.1423-1434.
4. Convery, D. J. and Rosenbloom, M. E., *The generation of intensity-modulated fields for conformal radiotherapy by dynamic collimation*, Phys Med Biol, 1992, **37**, p.1359-1374.
5. Bortfeld, T., Kahler, D. L., Waldron, T. J., and Boyer, A. L., *X-ray field compensation with multileaf collimators*, Int J Radiat Oncol Biol Phys, 1994, **28**, p.723-730.
6. Ling, C. C., Burman, C., Chui, C. S., Kutcher, G. J., Leibel, S. A., LoSasso, T., Mohan, R., Bortfeld, T., Reinstein, L., Spirou, S., Wang, X. H., Wu, Q., Zelefsky, M., and Fuks, Z., *Conformal radiation treatment of prostate cancer using inversely-planned intensity-modulated photon beams produced with dynamic multileaf collimation*. Int J Radiat Oncol Biol Phys, 1996, **35**(4), p.721-30.
7. Otto, K., *Volumetric modulated arc therapy: IMRT in a single gantry arc*, Med Phys, 2008, **35**(1), p.310-318.
8. Holt, A., *et al*., *Multi-institutional comparison of VMAT vs IMRT for head-and-neck cancer: a planning study*, Radiother Oncol, 2013, **8**(26), doi:10.1186/1748-717X-8-26 Quan E.M., *et al*., *A comprehensive comparison of IMRT and VMAT plan quality for prostate cancer treatment*, Int J Radiat Oncol Biol Phys, 2012, **83**(4), p.1169-78.
9. Abbas, A.S., Moseley, D., Kassam, Z., Kim, S.M., and Cho, C., *Volumetric-modulated arc therapy for the treatment of a large planning target volume in thoracic esophageal cancer*, J Appl Clin Med Phys, 2013, **14**(3), p.192-202.
10. Peters, S., Schiefer, H., and Plasswilm, L., *A treatment planning study comparing Elekta VMAT and fixed field IMRT using the varian treatment planning system eclipse*, Radiother Oncol, 2014, **9**(153), doi: 10.1186/1748-717X-9-153
11. Mijnheer, B.J., Battermann, J.J., and Wambersie, A., *What degree of accuracy is required and can be achieved in photon and neutron therapy?* Radiother Oncol, 1987, **8**(3), p.237-52.
12. Wambersie, A., *What accuracy is required and can be achieved in radiation therapy* (review of radiobiological and clinical data). Radiochim Acta, 2001, **89**, p.255-264.
13. Brahme, A., *Dosimetric precision requirements in radiation therapy*. Acta Radiol Oncol, 1984, **23**(5), p.379-91.
14. International Commission on Radiation Units and Measurements, *Determination of absorbed dose in a patient irradiated by beams of X or gamma rays in radiotherapy procedures*, ICRU Report 24, International Commission on Radiation Units and Measurements: Washington. 1976.
15. Thwaites, D., *Accuracy required and achievable in radiotherapy dosimetry: have modern technology and techniques changed our views?*, Journal of Physics: Conference Series, 20130, 444, 012006.

16. Valentin, J., *Case histories of major accidental exposures in radiotherapy*, Annals of the ICRP, 2000, **30**, p.23-29.
17. Leveson, N.G., Turner, C.S., *An investigation of the Therac-25 accidents*, IEEE Computer, 1993, **26**, p.18-41.
18. "El accidente del Clínico de Zaragoza, una cadena de fallos humanos única en el mundo, según los expertos". El País (in Spanish). October 12, 1991. Archived from the original on October 10, 2012.
19. *Accidental Overexposure of Radiotherapy Patients in Bialystok*, International Atomic Energy Agency: Vienna. 2004.
20. Bogdanich, W., *Radiation Offers New Cures, and Ways to Do Harm*, The New York Times, January 23, 2010,
21. Borius, P.Y., Debono, B., Latorzeff, I., *et al*. *Dosimetric stereotactic radiosurgical accident: Study of 33 patients treated for brain metastases*, Neurochirurgie, 2010, **56**, p.368-373.
22. Derreumaux, S., Etard, C., Huet, I.C., *et al*. *Lessons from recent accidents in radiation therapy in France*, Rad. Prot. Dosim., 2010, **131**, p.130-135.
23. Gourmelona, P., Bey, E., De Revel, T., *et al*. *The French radiation accident experience: emerging concepts in radiation burn and ARS therapies and in brain radiopathology. Radioprotection*, 2008, **43**, p.23-26.
24. Mans, A., *et al*., *Catching errors with in vivo EPID dosimetry*, Med Phys 2010, **37**(6), p.2638-44.
25. Ford, E., Terezakis, S., Yang, Y., Harris, K., and Mutic, S., *A quantification of the effectiveness of standard QA measures at preventing errors in radiation therapy and the promise of in vivo EPID-based portal dosimetry* (abstract). Med Phys, 2011, **38**, p.3808.
26. Ford, E., Terezakis, S., Souranis, A., Harris, K., Gay, H., and Mutic., *Quality Control Quantification (QCQ): A tool to measure the value of quality control checks in radiation oncology*, Int J Radiat Oncol Biol Phys., 2012, **84**(3), 263-9.
27. World Health Organization Radiotherapy Risk Profile: http://www.who.int/patientsafety/activities/technical/radiotherapy_risk_profile.pdf

CHAPTER TWO: INTRODUCTION

Presently, state-of-the-art external beam radiotherapy provides complex, conformal dose distributions using a sophisticated medical linear accelerator (or 'linac'). For VMAT, the modulation of linac gantry rotation speed, beam shaping, and dose rate are planned and optimized prior to delivery to the patient. In the following sections discussions will include: the general operation of a typical linac, focusing on the beam production and collimation systems, the Monte Carlo techniques involved in modeling a linac, how dose is predicted (calculated) within a patient by both the Eclipse treatment planning system (TPS) (Varian Medical Systems, Palo Alto, CA), and the in-house developed CancerCare Manitoba (CCMB) dose prediction model. A brief description on the dosimetric devices used to verify beam output and VMAT delivery and a review of electronic portal imaging devices (EPIDs) and how they perform as dosimetric devices will be discussed.

2.1 LINEAR ACCELERATOR OPERATION

The main components of a typical medical linear accelerator are illustrated in Fig. 2.1. Electrons produced by a filament gun are accelerated to relativistic speeds through the linac's accelerating waveguide. The radio frequency (RF) fields used for electron acceleration within the waveguide are produced by accelerating and decelerating electrons in retarding potentials within evacuated devices called klystrons (or magnetrons). The accelerating waveguide restricts the RF field waves to propagate in one-dimension, and in essence reflect back and

forth like a standing wave through a series of variably spaced disks called irises. Each subsequent iris section has an increased wave power and therefore there is an increase in the acceleration given to the electrons. The electrons, now at high energy, are ejected from the waveguide towards a steering magnet. This steering magnet (usually a quadrupole magnet) bends the high energy electron beam 270° so that it is directed towards the x-ray target. It is the interaction of this high energy electron beam with a thick, high atomic number target that generates x-rays for the therapeutic beam.

As high energy electrons interact with the thick target, they undergo collisions and decelerations. A small fraction of the decelerating electrons produce bremsstrahlung ('braking ray') x-rays. The bremsstrahlung x-ray energy spectrum is continuous and ranges from 0 to the maximum electron energy, E^{e}_{max}. Fig. 2.2 shows a 6MV bremsstrahlung photon spectrum produced by a typical medical linac. The average energy of the x-ray spectrum produced by a medical linac is roughly $E^{e}_{max}/3$ (Appendix 8.1.1 discusses this process in more detail).

The radiation yield of high energy photons increases with higher atomic number absorbers. Targets made of tungsten are popular because the large atomic number (Z=72) provides a high bremsstrahlung radiation yield. Tungsten is also a good choice due to its high melting point, making it more robust to heat produced through collisions. Multiple collisions between high energy electrons and the absorbing medium atoms can produce a substantial amount of heat and in most cases dedicated target cooling systems are also required to prevent physical damage of the target. Water lines fixed to a copper base under the target

allow for efficient cooling. The higher the energy of the incident electrons the more forward-peaked and more intense the resulting bremsstrahlung radiation is. For example 90% of the bremsstrahlung intensity produced by 5 MeV electrons (velocity of 0.997c) are confined to a conical spread of $\theta_{90\%}$= 20° downstream of the tungsten target. The bremsstrahlung intensity of 5 MeV electrons is roughly 10^5 times greater than 1 MeV electrons (v = 0.941c) which has a $\theta_{90\%}$= 70°. Currently at CancerCare Manitoba all VMAT treatments are delivered using a common linac platform (Clinac 2300ix systems, Varian Medical Systems, Palo Alto, CA) employing a 6 MV polyenergetic spectrum of x-rays produced by a nominal 6 MeV electron beam incident on a tungsten target 2.46 mm thick.

The 'head' of the linac, highlighted in yellow in Fig. 2.1, contains several components which are used to shape, collimate, and monitor the photon beam. The primary collimator is a tungsten cylinder hollowed out in in the shape of a cone and is used to restrict the initial bremsstrahlung x-ray beam produced in the target.

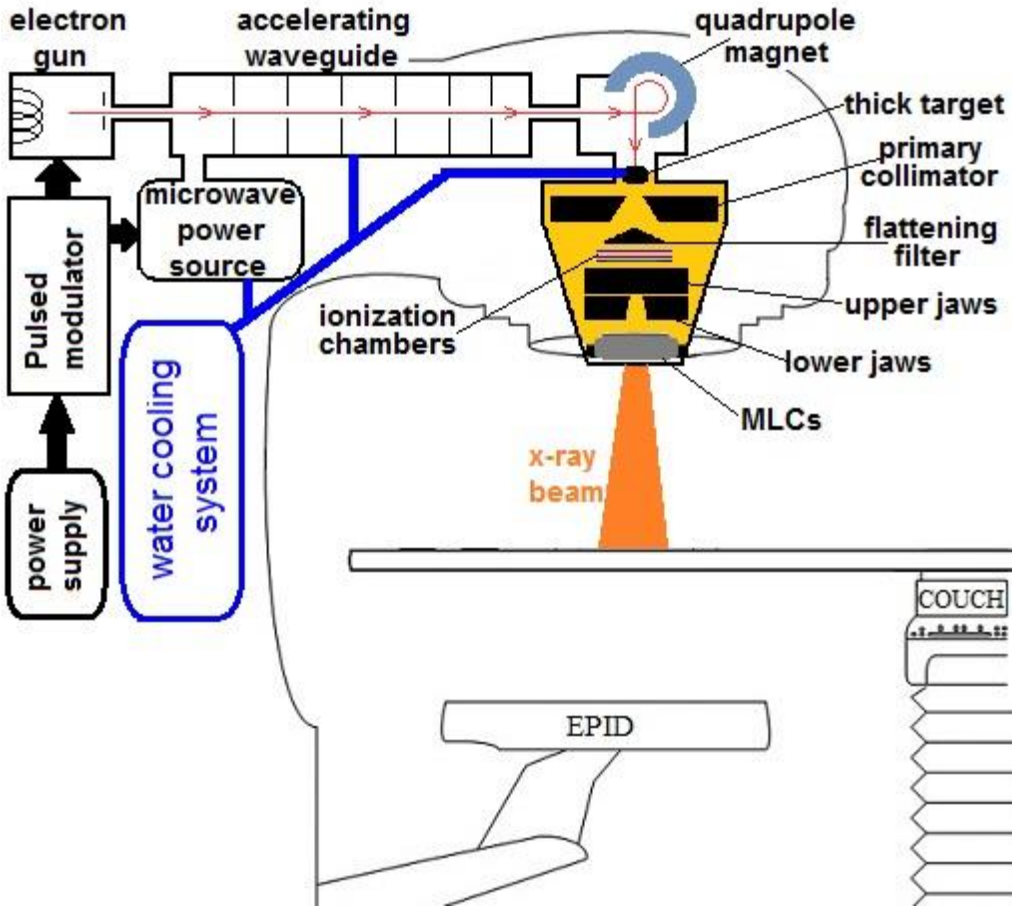

Fig. 2.1 [Linear Accelerator]: The main components of a typical medical linear accelerator (not to scale).

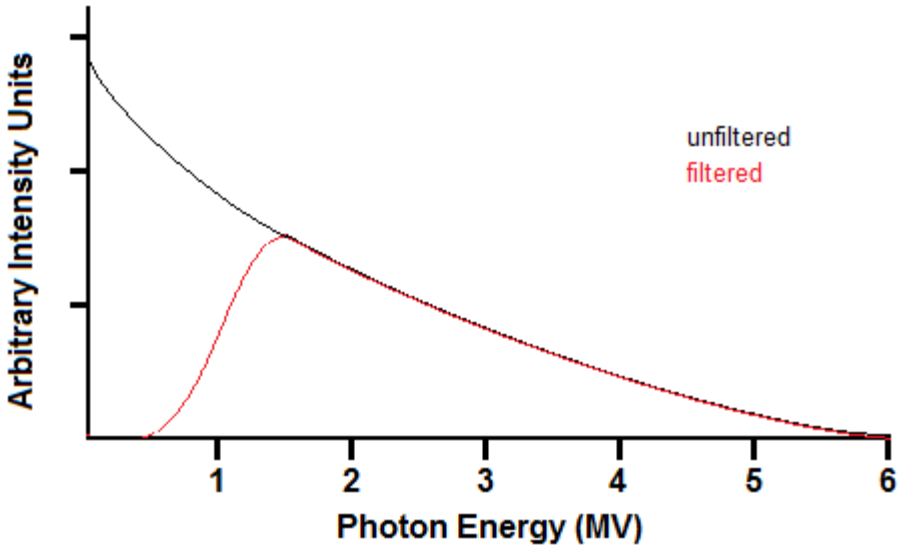

Fig. 2.2 [Bremsstrahlung Spectrum]: A filtered (red) bremsstrahlung photon spectrum produced by a typical medical linac and un-filtered spectrum (black).

A flattening filter is commonly used to 'flatten' the beam intensity of the initially forward-peaked x-ray beam. Recently (~2010), linac manufacturers have provided an option for a 'flattening filter free' beam, where the flattening filter is removed and the beam intensity profile is solely modified by MLC modulation, allowing higher dose rates deliverable to the patient. X-ray beam profiles with and without a flattening filter are illustrated in Fig. 2.3. The conical shape of the filter results in more attenuation of the central x-ray beam and less attenuation of the outer x-ray beam. By design, this produces a more uniform and 'flattened' beam intensity within the patient. However, the flattening filter also preferentially absorbs more of the lower energy x-rays in the beam creating an effect on the energy spectrum called 'beam hardening'. Beam hardening increases the x-ray beam's average energy and thus its overall penetrating power, relative to an un-flattened beam. In general, the greater the atomic number and thickness of the flattening filter the greater the hardening effect on the beam spectrum; however, this also lowers the beam intensity. There are numerous studies determining the best materials for a flattening filter and typically

aluminum, steel, or tungsten is used. For conventional 6 MV delivery with the Varian 2300ix linacs at CancerCare Manitoba, a flattening filter comprised of steel and copper is used while for SBRT delivery a smaller tungsten flattening filter is used.

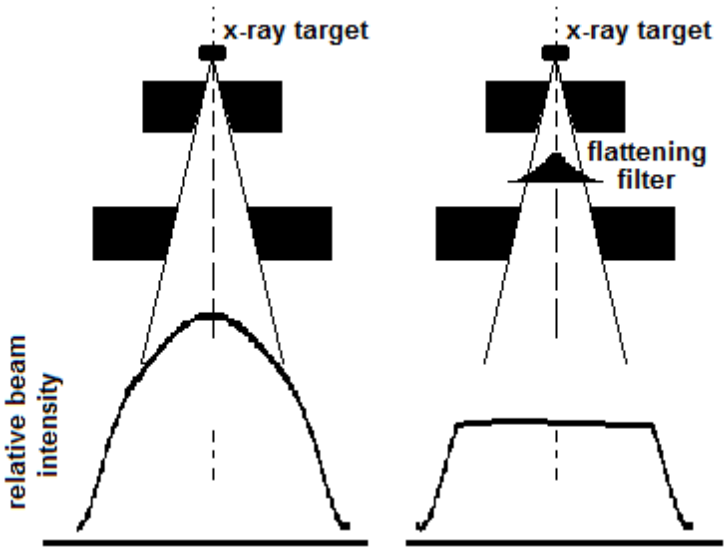

Fig. 2.3 [Flattening Filter Effect]: Beam intensity profiles for a flattening filter free (left) and flattening filter included (right) linac head. The flattening filter 'flattens' the x-ray beam's intensity.

As discussed, the conical shape of most flattening filters results in preferential beam hardening on the central axis compared to points further off axis. Due to this energy spectrum difference, the beam profile can only be exactly flat at one depth (usually a depth of 10 cm below the surface). Dose profiles at shallower depths are under-flattened while dose profiles at deeper depths are over-flattened. The under-flattened profiles are said to have 'beam horns'. This is illustrated in Fig. 2.4

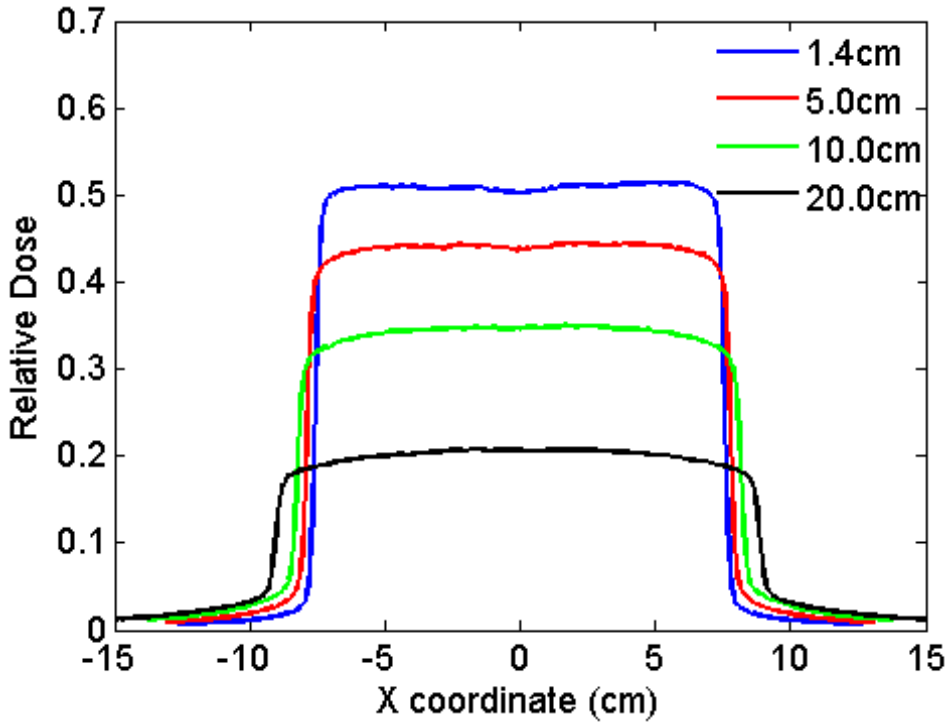

Fig. 2.4 [Water Tank Profiles] 15x15 cm^2 6 MV water tank profiles of varying depths. Slight horns are visible at depths less than 10 cm.

After the flattening filter the therapeutic x-ray beam encounters a layer of ionization chambers (with negligible attenuation) which measure and confirm the dose rate being delivered by the linac. After the ionization chambers, a set of simple, solid *x* and *y*-plane jaws, usually made of tungsten, are used to further form and/or restrict the beam. A set of motorized and computer controlled multi-leaf collimators (MLCs) comprised of 'fingers' of tungsten are used to further shape and conform the radiation beam either statically or dynamically during treatment in order to reduce radiation to organs-at-risk within the patient. The MLC can consist of anywhere between 60 up to 120 individual leaves, each of which are computer controlled by electronic motors. The leaves allow for precise fluence shaping required by the treatment plan.

If an incident bremsstrahlung photon interacts with any of the above-mentioned components it can produce secondary electrons and/or photons. This is defined as the 'extra-focal' beam intensity or fluence, and is sometimes also referred to as 'head scatter'. In contrast, the 'focal' beam fluence is defined as the non-interacting photons produced by the target.

2.2 MODELING LINAC FLUENCE

2.2.1 Monte Carlo linac simulation

Due to the complexity of the linac head components and the stochastic nature of photon interactions, the most accurate way to model the fluence exiting the linac head is through Monte Carlo style, radiation transport calculations[1]. Monte Carlo methods are versatile and can accurately determine the dose distribution of nearly any scenario. Due to improved computing power over the past decade, Monte Carlo techniques can now be incorporated into the treatment planning of radiotherapy beams[2-5]. Although the Monte Carlo approach is the most accurate, it still requires substantially longer calculation times than other calculation methods.

There are numerous software and codes available which can perform Monte Carlo simulations of modern linacs. We will limit the discussion here to EGSnrc (electron gamma shower, National Research Council of Canada)[6] which is the most popular code used in the radiotherapy community. The original code (EGS4)[7] was a radiotherapy extension of the

code used for simulation of high energy particle physics experiments at the Stanford Linear Accelerator Centre. The code was recently overhauled for improved accuracy in simulating therapeutic and diagnostic radiation beams, primarily by Kawarakow *et al*.[6] and Rogers *et al*.[8,9] while working at the National Research Council of Canada. This code version, now named EGSnrc, simulates photon interactions within the linac head components, phantoms or patients (via imported CT data sets), and measurement devices such as ionization chambers. The core of the code can be divided into two components: a linac head simulation software called BEAMnrc, and a patient/phantom Cartesian coordinate simulation software called DOSXYZ (a polar coordinate code is also available, called DOSRZ).

BEAMnrc has a simple user interface which utilizes the EGSnrc code in the background to simulate linac head components in detail. The user can input precise geometric specifications and material densities based on manufacturer design blueprints. There are numerous options within the code to allow relatively easy modeling of linac components with complex geometries, such as the flattening filter.

Photon and electron interactions within the linac head are governed by the interaction cross-sections which are a function of the photon energy and atomic number of the interacting material. Specific interaction types are discussed in greater detail in the thesis Appendix, Section 8.1.2. EGSnrc accesses individual interaction cross-sections for specific particles, energies, and materials via data files. Random number generator calls, scaled to the cross-sectional probabilities provided by the data files, determine the interaction type on a per-particle basis. If new, secondary particles are generated, these are also simulated using

the same cross-sectional probability functions. Energy deposition is determined and tracked, and both magnitude and spatial location recorded. Thus the trajectory of each initial particle is simulated, as well as secondary particle(s) produced. The process continues until each particle's (photon or electron) energy falls below a user-set threshold, in which case the particle history terminates in local energy deposition (in most cases an electron and photon cutoff energy of 0.521 MeV and 0.01 MeV respectively are used to simulate therapeutic beam interactions). Rayleigh and Compton scattering as well as the photoelectric effect and pair production are all possible interactions within the EGSnrc code. The loss of kinetic energy from low energy electrons produced in these interactions deposits dose in the medium. For therapeutic 6 MV beams the mean energy transferred to the electrons from photon interactions in the patient (primarily by the Compton effect) is generally equal to the mean energy absorbed by the medium (dose), i.e., the released electrons have a negligible bremsstrahlung yield since the patient is mainly composed of low *Z* tissues.

BEAMnrc produces a phase space file as its output, which describes all the photon and electron particles at any user-defined plane downstream of the linac head. This file can be processed by utility program BEAMdp (or other user-written software) to determine various parameters of interest, such as the fluence exiting the linac. The phasespace files can also be used as input for the DOSXYZ code in order to determine dose deposition within a medium downstream of the phase space plane. DOSXYZ can construct precise homogeneous or heterogeneous slab phantoms, or import a patient's volumetric CT data set. The EGSnrc code is then used to simulate the radiation transport in the phantom/patient and determine the 3D dose distribution at a specified voxel resolution.

2.2.2 Dual source modeling

The EGSnrc software has the ability to separately track the dose deposited due to the focal fluence and extra-focal fluence. This is an important tool to help create analytical functions that can model these fluence distributions for treatment planning systems. Many physical models have also been investigated in order to estimate the focal and extra-focal fluence separately[10-17]. These models were validated with Monte Carlo methods. The work of Jaffray *et al.* determined that the modeled focal fluence is the largest contributor to the total fluence and is independent of field size while the extra-focal fluence is a small contributor to total fluence (<12%) and dependent on the field size[15], with larger field sizes allowing more extra-focal fluence to contribute to patient dose.

Work by Sharpe *et al.* further characterized the extra-focal fluence component through precise experimental measurement and validated convolution-superposition calculations of dose that accurately predicted the separate fluence components of a linac[16]. The convolution-superposition approach is an accurate, model-based dose calculation method which involves the convolution of TERMA (total energy released per unit mass), derived from the linac head fluence, with spatially invariant dose deposition kernels. Improved accuracy can be achieved if the dose deposition kernels are modified on a voxel-by-voxel basis to account for regional variations in densities, in which case they are no longer spatially invariant and therefore a superposition is performed[18,19]. They also demonstrated accurate modeling of the relationship between increasing field size and increasing extra-focal fluence.

2.2.3 Eclipse treatment planning system

The Eclipse Treatment Planning System (TPS) was developed by Varian Medical Systems (Palo Alto, CA) to plan customized radiation treatments and calculate predicted dose distributions within the patient[20]. A 3D, pencil-beam, convolution-superposition algorithm (named 'anisotropic analytical algorithm' or AAA) calculates dose within the patient. The AAA algorithm was originally developed by Ulmer and Harder[21,22]. Eclipse is the main TPS currently used clinically at CancerCare Manitoba.

For the AAA algorithm, any collimated photon beam incident on the patient is separated into a number of infinitesimal, narrow "pencil beams" or beamlets. Each of these beamlets deposits dose along its central axis "ray-line" depending on the intensity and spectrum of the beam incident on the patient. Each beamlet's intensity and spectrum is defined by beam limiting devices such as the collimating jaws and MLCs. Dose deposition kernels are derived from Monte Carlo data matched to measured data in water. Each beamlet's fluence (comprising of focal, extra-focal, electron, and patient scatter) is converted to TERMA and undergoes an analytic convolution (reduces calculation time) with its respective dose deposition kernel.

Primary (focal) and extra-focal photons, as well as contaminant electrons exiting the linac head, are each modeled independently via Monte Carlo simulation. Spatially-variant Monte Carlo derived convolution scatter kernels are employed to calculate the patient scatter dose. Thirteen lateral scatter kernels per beamlet allow for anisotropic patient scatter calculation. In order to correct for tissue inhomogeneities, a radiological scaling of the dose deposition

kernels and electron density-based scaling of the scatter kernels is performed for each beamlet based on the patient's CT data. A summation of the photon and electron convolution results (i.e. dose contributions) provides the final 3D dose distribution within the patient.

2.2.4 CCMB models

Over the last 15 years the EPID dosimetry research group at CancerCare Manitoba (CCMB) has been developing robust, physics-based models which can (i) predict the fluence at any plane downstream of the linac head, (ii) calculate dose deposited in a patient or phantom, and (iii) calculate dose deposited to an EPID[23-31]. The fluence model was originally based on that of the Pinnacle[32] TPS (Philips Medical Systems, Amsterdam, Netherlands) but has several enhancements to increase accuracy. Patient dose prediction is accomplished with an in-house implementation of the 'collapsed cone convolution' algorithm, based on the work of Ahnesjo[33]. This is the most accurate model-based patient dose calculation available[34-37]. The EPID dose is calculated with a pencil-beam style algorithm that has been shown to accurately model the complex energy response of the EPID[27-30]. The individual models can be implemented together in two different configurations: 1) A 'forward' approach, where fluence, patient dose, and EPID dose are predicted sequentially, and 2) an 'inverse' approach, which takes measured EPID images as input and incorporates forward-predicted information to estimate fluence entering the EPID that is then back-projected to calculate the patient dose. The two approaches will be discussed here. A more detailed description of the physical processes involved in modeling a SBRT-VMAT linac beam is provided in Chapter 5.

i) *Forward model*

A Clinac 2100ix linear accelerator head (Varian Medical Systems, Palo Alto, CA) was modeled using the BEAMnrc software package. The phase-space file output of the simulation was input into DOSXYZ to calculate dose in a large cube of water in order to validate the Monte Carlo modeling against measured water tank data. Chytyk *et al*. performed an in-depth analysis using Monte Carlo data in order to model both the focal and extra-focal fluence independently[27]. Analysis of the extra-focal energy spectrum, profile, and contributions from the various linac head components determined that a Pearson VII function best fit the fluence profile. Although similar to the Gaussian, the Pearson VII function has an extra fitting parameter (three in total) which determines the tail decay of the peak (see Fig. 2.5). Similar to a Gaussian function, the other two parameters define peak height and width. The focal fluence profile was also analyzed and was determined to fit a Gaussian shape. The optimization iteratively compared predicted EPID image profiles through central axis to measured EPID image profiles. A nonlinear least squares optimization based on the interior point method determined the fitting parameters. The objective functions for the focal and extra-focal fluence predictions were based on the sum of the squared differences between the CAX normalization values of the measured and predicted EPID images. The specific EPID measurements performed for this optimization are discussed in Chapter 5.

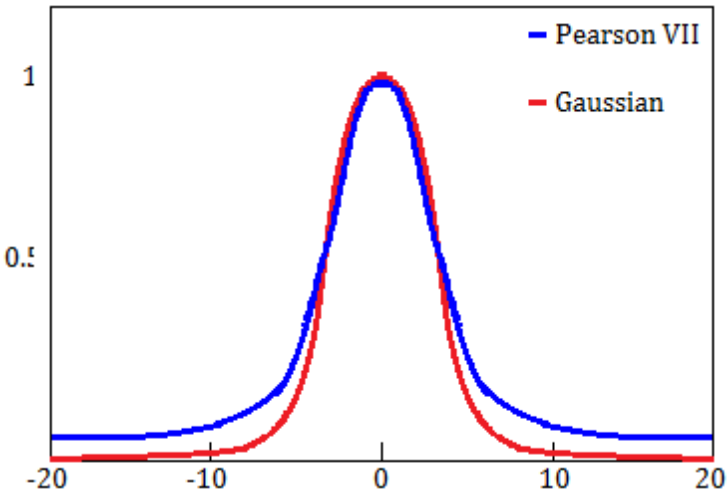

Fig. 2.5. [Fluence Functions]: Sample profiles of a Pearson VII function (blue), for modeling extra-focal fluence, and a Gaussian function (red), for modeling focal fluence. The Pearson VII has a longer decaying tail which better fits the extra-focal fluence.

As discussed in Section 2.1, when present, the linac's flattening filter directly impacts the profile shape of the focal fluence incident on the patient. The flattening filter and the primary collimator are both circularly symmetric, and therefore the focal fluence shape is modeled with a radially symmetric function. The radially-symmetric attenuation and the off-axis softening of the focal fluence by the flattening filter are modeled explicitly with ray tracing through the flattening filter (note that this requires the flattening filter shape and material specifications from the manufacturer). The extra-focal radial energy spectrum is not softened off-axis. Both the focal and extra-focal energy fluence exiting the linac head were determined by ray-tracing and attenuating the respective fluence through the jaws and MLCs. This also requires knowledge of the MLC shape (i.e., geometries) and materials from the manufacturer.

The predicted energy fluence exiting the linac head is then further modified by the patient (or phantom) before interacting with the EPID. The primary radiation beam traversing the

patient is attenuated, while photon scatter generated in the patient will also reach the detector. The model uses a superposition of patient scatter fluence kernels to account for the patient scatter at the EPID plane. A library of radially symmetric patient scatter fluence kernels were generated with BEAMnrc using a 6 MV pencil beam of fluence, perpendicularly incident on a homogeneous solid water phantom. These were calculated for a range of air gaps (distance between the patient and EPID), and phantom thicknesses. Photon scatter occurring within the air gap was considered to be negligible.

To utilize this library of scatter kernels, the model employs an 'equivalent homogeneous phantom' (EHP) concept. This concept replaces the heterogeneous patient CT data set with a phantom of uniform, water equivalent density, that possess the same radiological water thicknesses as the original CT data set as determined by ray-tracing[38] from the bremsstrahlung target through the patient to every pixel in the EPID plane.

The energy fluence incident on the EPID is determined in two components: a primary fluence, Φ_P, which consists of the photons from the focal and extra-focal sources of the linac, and a patient scatter fluence, Φ_S, which consists of the scattered photons generated within the patient. Both primary and scatter energy fluences are a function of the 2D position defined in a plane perpendicular to the beam's axis. They are also a function of the photon energy. The energy bin sizes (fifteen in total), ranging from 0.1 to 6.0 MeV, are specifically chosen to preferentially sample lower energies and therefore provide an accurate model of the low energy sensitivity of the EPID's energy response. The primary fluence at the plane of the

EPID, Φ_P, is calculated by taking the total incident energy fluence on the patient, Φ_I, predicted from the head model, and attenuating it by the radiological pathlength of the EHP

$$\Phi_P = \Phi_I \cdot e^{-\left(\frac{\mu}{\rho}\right)_{water} \cdot \rho_{water} \cdot RPL_{EHP}} \cdot \frac{1}{r^2} \quad [2.1]$$

where $\left(\frac{\mu}{\rho}\right)_{water}$ is the energy dependant mass attenuation coefficient for water (μ is the linear attenuation coefficient of water), ρ_{water} is the density of water, RPL_{EHP} is the EHP radiological pathlength, and the $\frac{1}{r^2}$ term accounts for the inverse square effect with r being the distance between the incident fluence plane and the EPID. The total patient scatter fluence at the EPID is determined via a superposition between the total incident fluence and the patient scatter fluence kernels:

$$\Phi_S = \sum_{x,y} \Phi_{I,rel} \cdot K_s^{g,l} \cdot \Delta x \Delta y \quad [2.2]$$

where $\Phi_{I,rel}$ is the total incident fluence relative to the associated rayline yielding the patient scatter fluence distribution at the plane of the EPID, K_S is a patient scatter fluence kernel selected for the specific air gap (g) and EHP pathlength (l), and $\Delta x \Delta y$ account for the discretized step size of the integration, i.e., the resolution of the calculation in the EPID plane.

The total fluence at the plane of the EPID is a summation of the primary and patient scatter fluences

$$\Phi_{EPID} = \Phi_P + \Phi_S \quad [2.3]$$

The total dose at the EPID is calculated via a series of convolutions (symbolized by '⊗') of the total fluence entering the EPID with Monte Carlo generated, mono-energetic dose deposition kernels, K_d. This is summed over all energy bin contributions, E_i, at every x and y position on the EPID plane (i.e. at each EPID pixel).

$$D_{EPID}(x,y) = \sum_i \Phi_{EPID}(x,y,E_i) \otimes K_d(x,y,E_i) \quad [2.4]$$

Additional EPID dose effects due to photon backscatter from the EPID support arm (aS500 and aS1000 models, Varian Medical Systems) is added via a measurement-based model determined by Rowshanfarzad *et al.*[29]. To correct for EPID optical glare, a convolution of the backscatter corrected EPID dose, $D_{EPID}(x,y)$, with a spatially invariant, optical photon point spread function was performed. The optical glare point spread function was based on the work of Kirkby and Sloboda[39], and is known to be a small effect (<2%). Both are given in more detail in the following section.

For VMAT, all delivery parameters are given as a function of gantry angle and are discretely defined by the TPS as 'control points' (CPs). Typically, there are 178 CPs per 360° used to control VMAT delivery on Varian linac's. Each CP defines the MLC position and the amount of fluence to be delivered since the previous CP. Fluence is quantified in terms of monitor units or MU's – a measure of the magnitude of x-ray fluence delivered by the

linac, in practice it determines how long the x-ray beam is 'on' at a given dose rate. This treatment plan data are used by the forward model in order to predict both the magnitude of fluence and MLC shape per EPID image as a function of gantry angle. The prediction can be performed at the same native angular resolution of the TPS (i.e. 178 CPs) or interpolated in order to produce EPID images at lesser or greater angular resolution.

ii) *Inverse model*

The CCMB inverse dose model combines the ability to predict fluence entering the EPID and dose deposited in the EPID from the forward model with information contained in a measured EPID image. This is described in detail by VanUytven *et al.*[31] and will be only briefly discussed here.

The forward model independently determines the focal and extra-focal energy fluence components exiting the linac head. Therefore at the plane of the EPID the total predicted energy fluence, $\Phi^{pred}_{Total,EPID}$, is defined as the sum of the focal, Φ^{pred}_{f}, and extra-focal, Φ^{pred}_{ef}, predicted components due to the primary beam transmission plus the patient scatter energy fluence:

$$\Phi^{pred}_{Total,EPID} = \left[\Phi^{pred}_{f} + \Phi^{pred}_{ef}\right]_{Prim} + \left[\Phi^{pred}_{f+ef}\right]_{Scat} \quad [2.5]$$

The total predicted dose at the plane of the EPID is then given as:

$$D^{pred}_{Total,EPID} = \left\{\left[D^{pred}_{f} + D^{pred}_{ef}\right]_{Prim} + \left[D^{pred}_{f+ef}\right]_{Scat} + D^{pred}_{bs}\right\} \otimes K_{glare} \quad [2.6]$$

where K_{glare} is a spatially invariant point spread function which corrects for optical glare within the scintillator determined by Kirkby and Sloboda[39] to have the form:

$$K_{glare} = e^{-49.3r} \quad [2.7]$$

where r is the radial distance from the central axis of the EPID and the decay parameter, -49.3, is for a 6 MV spectrum. D_{bs}^{pred} is the predicted additional dose component due to the backscatter of photons from the EPID's support arm determined by Rowshanfarzad *et al*.[29]. It has the form:

$$D_{bs}^{pred} = \left\{\left(\left[D_f^{pred} + D_{ef}^{pred}\right]_{Prim} + \left[D_{f+ef}^{pred}\right]_{Scat}\right) \cdot M_{bs}\right\} \otimes K_{bs} \quad [2.8]$$

where the selected form of K_{bs} that best agreed with both experimental and Monte Carlo data had the form:

$$K_{bs} = 6.912exp\left[\frac{-(r+1.394)^2}{90.696}\right] \quad [2.9]$$

where r is the radial distance from the central axis of the EPID and M_{bs} is a mask matrix which models the support arm area downstream of the EPID.

A measured EPID image will inherently contain the sum of the individual dose components given in Eq. 2.6. However, using the independently predicted dose components from the forward model, an estimate of the measured EPID primary focal dose can be

isolated. The predicted primary focal energy fluence at the plane of the EPID, $\left[\Phi_{f,EPID}^{pred}\right]_{Prim}$, is then adjusted by the ratio of measured primary focal dose and predicted primary focal dose:

$$\left[\Phi_{f,EPID}^{pred}\right]'_{Prim} = \left[\frac{D_{EPID}^{meas} - \left\{\left[D_{ef}^{pred}\right]_{Prim} - \left[D_{f+ef}^{pred}\right]_{Scat} - D_{bs}^{pred}\right\} \otimes K_{glare}}{\left[D_{f}^{pred}\right]_{Prim} \otimes K_{glare}}\right] \cdot \left[\Phi_{f,EPID}^{pred}\right]_{Prim} \qquad [2.10]$$

where $\left[\Phi_{f,EPID}^{pred}\right]'_{Prim}$ is the adjusted predicted primary focal energy fluence at the EPID and D_{EPID}^{meas} is the measured EPID dose image. This adjustment is performed iteratively, based on the work of McNutt *et al.*[40,41], in order to match the predicted and measured primary focal fluence to within 1% of each other. A 1% tolerance was arbitrarily chosen which, for VMAT, converges to a solution of only one iteration.

The final estimate of the primary focal energy fluence at the EPID is then back-projected to a plane above the patient accounting for attenuation and the inverse square effect.

$$\left[\Phi_{f,z}^{pred}\right]'_{Prim} = \left[\Phi_{f,EPID}^{pred}\right]'_{Prim} \cdot e^{\left(\frac{\mu}{\rho}\right)_{water} \cdot \rho_{water} \cdot RPL_{EHP}} \cdot z^2 \qquad [2.11]$$

where $\left[\Phi_{f,z}^{pred}\right]'_{Prim}$ is the adjusted predicted primary focal fluence back-projected to a plane above the patient that is a distance z from the EPID plane and the rest are defined as in Eq. 2.1. The predicted extra-focal fluence (also considered part of the primary beam because the

back-projected plane is above the patient) is added to the result of Eq. 2.11 to define the estimated fluence incident on the patient:

$$\Phi_{I,z}^{pred} = \left[\Phi_{f,z}^{pred}\right]'_{Prim} + \left[\Phi_{ef,z}^{pred}\right]_{Prim} \quad [2.12]$$

Note that the step of using the predicted extra focal fluence to estimate the measured extra focal fluence assumes that there is no significant error in the extra focal fluence distribution. This assumption should be valid in most situations, as the extra focal fluence changes very slowly with changing MLC aperture as compared to the focal fluence which changes dramatically with changing MLC aperture. The fluence calculated from Eq. 2.12 is converted to TERMA (total energy released per unit mass) within the patient followed by a 3D superposition for heterogeneous media with Monte Carlo calculated point-based dose kernels. TERMA is equal to the product of the mass-attenuation coefficient and the energy fluence. This method is based on the work of Ahnesjo[33] whose implementation incorporates a collapsed cone convolution (CCC) to handle the superposition mathematics. The CCC method uses an analytical kernel represented by a set of cones, where the energy deposited in the cone is collapsed onto the central rayline of the cone and deposited into any intersecting voxels defined in the calculating volume.

Unlike Ahnesjo's patient dose calculation method, Eclipse's 'pencil beam'-based algorithm does not take into account any secondary electron transport. The secondary electrons set into motion by higher energy photons will travel further creating other photons and also deposit more dose. Furthermore, CCC's heterogeneity density-scaling is performed

using both physical density and electron density values from the patient's CT data. This leads to significantly larger dose errors from AAA at tissue boundaries and is magnified when two adjacent tissues have substantially different densities. The one major advantage the Eclipse AAA model has over the Ahnesjo CCC approach is its low calculation time. Although there is a loss of accuracy for heterogeneous calculations, a pencil beam convolution algorithm is substantially faster than a CCC calculation. A more in-depth analysis of Eclipse's AAA, our CCC, and Monte Carlo dose calculations are provided in Appendix 8.3.

2.3 VMAT DOSIMETRY DEVICES

Dosimetric verification of linac VMAT delivery parameters is crucial for patient-specific quality assurance (QA). VMAT typically incorporates complex MLC modulations which create steep dose gradient regions in the patient. Furthermore, the correct fluence is not easily inferred due to the dynamic, rather than static, MLC defined apertures. Because these field apertures can sometimes be quite small, this requires detectors to have a good spatial resolution in order to reduce volume averaging effects (i.e., the detector's cross-sectional area is larger than the field gradient thereby averaging high and low doses into a single point measurement)[42,43]. However, a reduction to the active detector volume will result in a poorer signal-to-noise ratio. An ideal detector should be able to measure in absolute dose units, have a linear response to dose and dose rate (for simplicity), track the dose accurately over small time intervals (for dynamic treatment deliveries), and also accurately integrate the cumulative dose of the entire treatment.

There are two ways one *can* perform patient-specific dosimetry: pre-treatment (prior to the treatment regimen being delivered to the patient) or during treatment (*in vivo*). In current practice, the pre-treatment approach is the most common routine QA method, while *in vivo* dosimetry is used infrequently, typically consisting of a single measurement point at the skin surface of the patient often near a critical structure of interest (such as the eye). At CancerCare Manitoba (CCMB) every VMAT plan undergoes a pre-treatment QA verification without the patient present and this is only done once prior to the treatment regimen. Point and planar dose measurements are acquired using ion chambers or diode detectors and radiographic films respectively inserted into specialized QA phantoms. Currently at CCMB, the specialized phantom for pre-treatment QA is a homogeneous, solid water phantom that allows for the insertion of sheets of film and an ionization chamber. This approach is used for the pre-treatment QA of all SBRT-VMAT treatments at our institute (approximately fifty patients per year). Non-SBRT VMAT pre-treatment QA is done using the COMPASS system (see Section 2.3.3) from IBA Dosimetry (Swarzenbruck, Germany), handling about 800 patients/year. COMPASS measures fluence above the patient plane and employs a CCC calculation of 3D dose with an imported TPS CT data set. Point and 3D (or 2D in the case of SBRT-VMAT) patient dose estimates are compared to the TPS calculation using a γ-evaluation method[44] in order to verify that the linac delivered the plan correctly (see Appendix 8.2 on dose comparison techniques such as the 3D γ-evaluation). Many commercial ion chamber or diode arrays are available for 2D, pre-treatment, patient-specific QA, and polymer gel dosimetric devices can be used for 3D, pre-treatment, patient-specific QA. EPIDs can also be used for 2D and 3D QA[45-52] and are already available on most commercial linacs although the software available is very limited and/or of poor accuracy.

Only three commercial packages exist: Dosimetry Check™ (Math Resolutions LLC), Epiqa (EPIdos s.r.o., Ivanka pri Dunaji, Slovakia), and Varian's PortalVision™ (Varian Medical Systems, Palo Alto, CA), the latter of which is strictly a predictive portal image software package. EPID dosimetry is discussed in Section 2.5. The advantages and disadvantages of each QA method will be discussed in the following sections.

2.3.1 Point-based measurement devices

Cylindrical ionization chambers are a common choice for point-based measurements and are commonly placed within a specialized phantom. They possess a linear response with dose, good signal stability, are insensitive to orientation and beam quality, generally are small in size, and can be calibrated to a standard chamber[53] for comparative results in absolute dose units. However, ionization chambers should be positioned away from regions of steep dose gradients in order to avoid measurement errors. If the chamber is too large with respect to the dose gradient it is placed within, it may suffer volume averaging effects[42]. For these reasons ionization chambers are generally placed in regions of slowly varying dose.

Solid state detectors such as diodes, metal oxide semiconductor field effect transistors (MOSFETs), and diamond detectors are also available for point measurements. The major advantage over ion chambers is that they have a smaller sensitive volume making them less prone to volume averaging effects and therefore better for 'small field' dosimetry. Diode detectors are generally quite accurate for central axis measurements but not as accurate for off-axis measurements due to their increased sensitivity to low energy photons (due to their higher atomic number compared to water-equivalent detectors)[54]. A recent study by Dieterich

and Sherouse determined that diode detectors will also over-respond for larger field sizes due to the increase in phantom/patient scatter[55]. Diodes are directionally dependent (errors as large as 3%[42]) and can be permanently damaged from radiation. MOSFETs are also small in size, have a directional dependence (errors as large as 2.5%), and have a linear response to dose[56]. Diamond detectors have an atomic number very similar to tissue but have a density of roughly three to four times larger. They exhibit much smaller directional dependence errors (generally <1%[57]) and have a greater resistance to radiation damage than diodes. However, they are dose-rate dependent and are therefore generally unsuitable for VMAT measurements.

2.3.2 Two-dimensional devices

Radiographic films exhibit high spatial resolution which makes them suitable for accurate modeling of high dose gradient regions, such as VMAT beam penumbra. Unfortunately the process of setting up and chemically processing radiographic film is cumbersome and time consuming. They lack reliable absolute dosimetry and exhibit an over-sensitivity to low energy photons due to the silver content in the emulsion layer. Radiochromic films are somewhat better than radiographic films for dosimetry, since they do not require chemical processing and are tissue-equivalent. However, they require a long wait time before data readout after irradiation (typically 8-12 hours). Conversion to absolute dose for films can be an inconvenient and labour intensive procedure, usually requiring the use of an ion chamber for calibration. This adds time and possible error to the overall setup and calibrated data readout.

Amorphous silicon (aSi) EPIDs have been used for the QA of intensity modulated radiation therapy (IMRT) beams[47,58,59] and have recently been implemented for VMAT[49-52]. EPIDs are digital radiation imagers that can operate in real-time. They have a linear response to dose, and possess a relatively high spatial resolution (<1 mm^2 pixels). Currently, commercially available EPIDs measure the dose delivered to a phosphor layer, as opposed to water, and can only be placed downstream from the patient/phantom (not upstream), and require somewhat complex calculations or corrections in order to determine the *in vivo* patient/phantom dose from measured transmission images. Alternatively to estimating *in vivo* patient dose, one can compare predicted EPID transmission images to actual measured EPID transmission images in order to perform patient transit QA and this approach is discussed further in Section 2.5.

2.3.3 Commercial devices for VMAT QA

There are multiple devices commercially available for VMAT QA. The more common devices will be discussed focussing on individual accuracies.

i) The DELTA4® (ScandiDos AB, Uppsala) system consists of two orthogonal planar arrays of diode detectors encased within a cylindrical polymethylmethacrylate (PMMA) phantom. It also has an inclinometer for independent gantry angle measurement. Each 20x20 cm^2 array has diodes spaced 10mm apart except for the 6x6cm^2 central ones which are 5mm apart. Bedford *et al.* determined VMAT dosimetric accuracy was within 2.5% of ionization chamber measurements but also outlined that it was a complex device and required careful benchmarking[60].

ii) The OCTAVIUS® (PTW, Freiburg, Germany) system consists of a single 2D array of ion chambers encased in an octagonal polystyrene phantom. The ion chambers have active volumes of 0.125 cm^3 and are separated by a center-to-center spacing of 10mm. Overall the system was found to perform quite well with minimal setup time and can also perform a 3D reconstruction of volume dose. Van Esch *et al.*, performed a 3D 2%/2mm γ-comparison with Eclipse and determined that the most recent OCTAVIUS model (1500 2D detector) produced γ fail-rates no lower than 6%. It was also found that there was a significant directional dependence producing lateral ('out-of-target') dose deviations[61].

iii) The COMPASS (IBA dosimetry, Schwarzenbruck, Germany) system consists of an array of 1020 ion chambers, each with volume 0.08 cm^3 at a spacing of 7.62 mm, and an independent gantry angle sensor. The array and angle sensor are physically attached to the linac gantry using a custom jig, and output is measured perpendicularly to the radiation beam. The measured planar dose is converted to an estimate of incident fluence which can then be used to calculate dose to the patient CT data set via a CCC style algorithm. Boggula *et al.* determined that COMPASS performed relatively well when compared to the TPS (percentage dose differences within 2.5% for the high dose regions and within 9% for the low dose regions) for VMAT treatments[62]. This system is currently employed for all non-SBRT VMAT pre-treatment QA at CCMB.

iv) The ArcCHECK (Sun Nuclear, Melbourne, FL, USA) system consists of a 2.5D array of diode detectors (10mm spacing and 0.64 mm^2 active size) placed in a spiral geometry within a 21 cm diameter cylindrical acrylic phantom. The diodes are

arranged in a non-overlapping arrangement with respect to the beam's-eye-view. There is an auxiliary insert in the center of the phantom with a cavity for ion chamber placement for absolute dose measurement and calibration. ArcCHECK can measure radiation in real time and saves all dose data (relative and absolute) as a function of time. Chaswal *et al.* determined a 2%/2mm γ-pass rate accuracy no lower than 95% with the TPS for VMAT plans, although they had no MLC modulation which is unrealistic for VMAT delivery[63]. Li *et al.* determined a minor directional dependence for VMAT deliveries with this device[64].

v) The Epiqa™ (EPIdos s.r.o., Ivanka pri Dunaji, Slovakia) is a software based system which utilizes the EPID on the linac. Using the GLAaS algorithm[65,66] it constructs 2D planar absolute dose maps from the integrated image of a full VMAT arc or IMRT field. The GLAaS algorithm employs calibration data sets, using ion chambers, in order to reconstruct planar dose maps in solid water at varying depths. These dose maps can then be compared to reference dose distributions (i.e., from the TPS) to verify treatment delivery. The software package is primarily used as a 2D IMRT/VMAT γ-analysis tool, however, it is mentioned (on the website: http://epidos.eu) that it is possible to utilize the software for 3D analysis of VMAT although no support is given.

A study performed by Fredh *et al.* compared the error detection accuracy of all these systems (except for ArcCHECK which was not operational due to technical difficulties) [67]. This was performed by manually introducing errors into delivered VMAT plans and comparing each system's result with the TPS prediction of the same plan without the error.

Errors included various types of incorrect MLC positions and dose rates. The Epiqa software detected all twenty of the introduced errors using a 2%/2mm analysis. The DELTA4 system was able to detect 15 of 20, COMPASS detected 11 of 20 and the OCTAVIUS system was only able to detect 8 of 20 (the authors suggest this was due to an improper CT scan of the OCTAVIUS 'seven29' phantom). Overall these systems can perform pre-treatment QA but also require software implementation and complex phantom setup and calibration. They also have limited resolutions $\leq$ 5-10 mm (except for Epiqa). Furthermore, due the better resolution of the Epiqa system potentially linked to improved error sensitivity (at least in one study by Fredh *et al*) this strongly encourages an EPID-based QA approach.

2.3.4 Three-dimensional detectors

Polymerizing polyacrimide gels (PAGs) are a type of 3D dosimeter which undergoes a molecular polymerization when exposed to radiation that is proportional to the absorbed dose. A polymer is a chain of essentially identical molecules. Exposing specific polymers to radiation induces cross-chain polymerization, which modifies the magnetic resonance signal of the solution (and optical scattering capabilities as well). One major disadvantage of the PAG gel is that their chemical composition is affected by oxygen so they need to be stored and manufactured in a hypoxic environment[68]. Fricke gel dosimeters[53] consist of ferrosulphates and need to be scanned within 2 hours of irradiation otherwise the dose distributions fade as the molecules return to their relaxed state. Both types of gels are analysed either by MR or optical CT scanning. Presently, gel dosimetry is explored mainly in a research capacity but has shown promise as an effective dosimeter for VMAT

treatments[68,69]. Other 3D dosimeters such as radiochromic polymers[70], polyurathene dosimeters[71], and plastic scintillators (plenoptic cameras)[72] have also shown promise.

2.4 PORTAL IMAGING

A portal image is defined as any digital or film-based image which captures the attenuated treatment field, or portal, exiting the patient. When first implemented in clinics they were primarily used to align the patient on the treatment couch before treatment. This was performed crudely by matching the bony anatomy visible in the portal image with planning images from radiographs constructed from the patient's CT data or planar radiographs taken at time of simulation (e.g. before CT simulation was routinely available). They were also used to verify aperture shaping of treatment fields.

Film cassettes were used as portal imagers in the mid-1970s through to the 1990's. Although they have good spatial resolution they required several minutes to process and interpret which allowed for some patient movement. Also, the contrast of the film was dependent on the dose delivered to the film, which required the technicians to select appropriate linac dose settings depending on patient thickness and film positioning. EPIDS were clinically implemented in the 1990's in order to overcome the disadvantages of film[73-75]. EPIDs exhibit near real-time output allowing for quicker patient repositioning. The first generation of EPIDs were camera-based for Elekta and Siemens linacs, while Varian used a scanning liquid ionization chamber (SLIC) EPID. In the early 2000's, Varian, followed by

Elekta and Siemens, released EPID designs based on active-matrix flat-panel imager (AMFPI) technology, which continues to be the standard EPID design on linacs today.

2.4.1 First generation EPIDs: Cameras & SLICs

Camera-based EPIDs were large and cumbersome, due to the camera's sensitivity to radiation damage. This required shielding and positioning the camera away from the primary x-ray beam, and also a light-tight enclosure surrounding the entire optical chain. They used a scintillating phosphor (typically gadolinium oxysulphide) layer to convert x-ray energy into optical photons. A thin layer of metal (~1 mm of brass or copper was common) was placed immediately upstream of and in contact with the scintillator to increase the number of interactions of incident photons and therefore increase the amount of radiation energy deposited in the scintillator. The scintillating layer would be located in the primary beam and mirrors were used to reflect the optical photons to the camera located outside the primary beam, shielded within the main gantry. All components in the optical chain would be enclosed in a light–tight box to ensure no leakage of converted optical photons and no intrusion of outside optical photons. These types of cameras exhibited relatively low detective quantum efficiency (DQE) around 1% (i.e., signal output efficiency from incident radiation) due to the long optical path between mirror and camera. Furthermore, the unwanted optical glare effect (sometimes known as veiling glare), due to optical photons scattering throughout the optical chain, could account for up to 25% of the total signal[76].

In the mid-1980s a group based out of the Netherlands Cancer Institute developed the SLIC EPID[77-81]. The basic construction consisting of two orthogonal 256x256 electrode planes (spaced at 1.27 mm) separated by an iso-octane liquid mixture and a plastoferrite

plate. X-rays would interact with the plastoferrite plate releasing electrons which would then ionize the liquid mixture and be collected by the electrodes. It had the advantage of being a compact device with no geometric distortion in the resulting image, but had a low DQE (on the order of 0.5%). Furthermore, due to a slow 'row-by-row' readout of the electrodes (roughly 5 seconds for a full frame) a lot of the generated signal in the liquid was lost and led to poor image quality.

2.4.2 Second generation EPIDs: AMFPIs

Active matrix flat-panel imagers are currently the standard EPIDs equipped on all commercially available linacs[73-75]. AMFPI EPIDs consist of a 1 mm metal buildup plate (usually copper) that absorbs incident x-ray photons and emits recoil electrons predominantly by the Compton and photoelectric effects. A 0.4 mm, terbium-doped, gadolinium oxysulphide (Gd_2O_2S:Tb) phosphor layer lies behind the metal plate and converts the generated electrons into visible photons. The phosphor screen is backed by an array of amorphous silicon (aSi) photodiodes coupled to thin film transistors (TFTs). The charge is integrated in the photodiodes until the TFT is triggered and read by the acquisition electronics. This charge is converted to grayscale signal per pixel (i.e., per photodiode), therefore providing an image proportional to the radiation intensity interacting with the metal plate and phosphorescent screen. The AMFPI EPID data is also acquired in a row-by-row fashion, about 0.105-0.133 seconds/frame, a much faster rate than the SLIC EPID[28,82].

AMFPI EPIDs have a low system noise (~1%), a high DQE (70-80% better than camera-based EPIDs), and spatial resolutions better than camera-based EPIDs[74,83,84]. The proximity

of the phosphor layer to the diode detectors dramatically reduces optical glare and increases optical photon collection efficiency. Currently, the standard commercial EPID in use at CCMB has a 1024x768 pixel array on a 40x30 cm^2 panel providing a pixel resolution of 0.39 x 0.39 mm^2. Varian and Elekta have both recently introduced newer EPIDs incorporating a physically larger panel (40x40 cm^2) with a1024x1024 pixel array.

The AMFPI aSi EPIDs are resistant to radiation damage as long as the circuitry components outside the active pixel area are not irradiated. They have been shown to be very stable and provide reproducible response over time[82,85]. One minor issue with the aSi EPID is an artefact known as 'ghosting' which occurs when charge still remains in the photodiodes after frame acquisition and is then added to subsequent frames[85,86]. In general this is a monitor unit (MU) dependant artefact and is more severe for smaller MU deliveries to the EPID. This can lead to a 1-2% over prediction of dose by the aSi EPID[86]. In general this effect is neglected due to the higher MU of clinical beams[87], although simple correction strategies can be employed[88]. Furthermore, using an EPID with a higher frame acquisition rate limits the number of MUs acquired per EPID frame.

The energy response of the detector is over-sensitive to lower energy photons (< 1 MeV) as compared to a water-equivalent detector[25,89]. This requires a correction method[90,91] or appropriate modeling, as described in Chapter 5 of this thesis, in order to use the EPID for water-equivalent dosimetry applications.

The a-Si EPID exhibits a linear response to dose and dose-rate which is desirable for dosimetry applications[25,28,82]. Each acquired EPID image, $I(x,y)$, is corrected by the dark-field (*DF* – accounting for pixel activity with the beam off) and flood-field (*FF* - compensates for the sensitivity differences between individual pixels). This is performed automatically within the clinical software and has the form:

$$I(x,y) = [I_{raw}(x,y) - DF(x,y)] \cdot \frac{FF_{mean}}{FF(x,y)} \qquad [2.13]$$

where FF_{mean} is the mean value of the flood-field image and I_{raw} is the raw image. Unfortunately, this method of flood field correction is undesirable for dosimetry applications as it removes beam-specific dosimetric information such as beam horns and off-axis profile shape. This dosimetric information can be recovered while still correcting for the pixel sensitivities using a technique proposed by Greer[92]. This involves isolating the DF corrected raw image, by simply multiplying Eq. 2.13 by $\left(\frac{FF(x,y)}{FF_{mean}}\right)$, and dividing it by an experimentally determined pixel sensitivity matrix (*PSM*)

$$I'(x,y) = \frac{I_{raw}(x,y) - DF(x,y)}{PSM(x,y)} \qquad [2.14]$$

Greer measured the PSM by irradiating the EPID with 10x25 cm^2 fields in 2.5 cm increments along the x-axis of the EPID. Assuming the ratio of the flood-field (one dimensional) and PSM profile (one dimensional) is radially symmetric (which it should be), the PSM can

easily be extended to two dimensions and then applied to the raw image, as in Eq. 2.14 in order to produce a flood field corrected image $I'(x,y)$.

EPID images for dosimetric applications are typically acquired using either an integrated mode, which sums all frames during irradiation into one EPID image, or a continuous mode (cine-mode, sometimes known as movie mode), whereby individual EPID frames are discretely frame-averaged into a series of EPID images over the duration of the irradiation. In order to acquire the time-dependent information of a VMAT delivery, cine-mode images must be used. The dosimetric accuracy of the EPID while operating in cine-mode was verified by McCurdy and Greer[28], although it was demonstrated that a small amount of signal was lost at the beginning and/or end of the irradiation. However for clinically relevant irradiations (VMAT deliveries usually involve >300 MUs), this small amount of lost dose becomes insignificant (<1%).

2.5 PORTAL DOSIMETRY

Using the EPID for patient dose verification (often termed 'portal dosimetry') can be performed in two ways: 'forward' methods and 'inverse' methods. From the definitions of Section 2.2.4, a forward model can theoretically predict expected EPID images (using the treatment plan data and possibly a CT representation of the patient) and then compare them to the actual measured images. The inverse model calculates the measured dose within the patient by back-projecting a fluence estimate at the EPID (derived from the EPID

measurement of dose). The dose calculated within the patient is usually compared to the treatment planning system calculated dose for verification. Both methods can be further divided into a pre-treatment (non-*in vivo*) or during treatment (*in vivo*) techniques. Pre-treatment involves the verification of the treatment plan before actual delivery to the patient and can be performed via a forward prediction (like the TPS) or an EPID measured ('inverse') reconstruction, the latter delivers the plan with no patient or phantom present while acquiring EPID images. The focus of this thesis is *in vivo* verification using an inverse model approach.

The forward calculation approach can be performed with or without a patient in the beam. Treatment beams are delivered to an EPID, and then the measured EPID images are compared to the predicted ones. For VMAT delivery this can be done as one full integrated image per arc (of limited use for VMAT, as this approach integrates all time dependent information) or with many sub-arc, frame-averaged EPID images[49-52,93-95]. The treatment plan breaks up the VMAT delivery into a series of 'control points' which describe the delivery in terms of MUs and MLC positions as a function of linac gantry angle, and a time-dependent series of predicted EPID images needs to be able to utilize this information. This approach can also include a homogeneous or anthropomorphic phantom in the beam in order to verify transit dosimetry[24,30,93,94,96-98].

There are numerous ways one can perform a forward dose prediction. Liu *et al.*[49], created an adjusted patient plan using control points defined from the angular resolutions and fractional MUs of each measured EPID image (defined in the image header) acquired

without the patient in the beam. This plan was imported back into the TPS in order to create an adjusted set of predicted images (using Varian's PortalVision^{TM} software) which were then compared in 2D and 3D to the measured ones. Woodruff *et al.*[93] integrated a predicted set of EPID images based on an independent forward model (i.e., the CCMB forward model) and compared these to the integrated measured EPID images. Fuangrod *et al.* also showed that a real-time comparison of forward predicted EPID images and measured cine-mode EPID images during VMAT delivery can also be used to verify MLC positions in real-time[99].

For VMAT, the inverse approach can be applied to both pre-treatment[94,95,107] and *in vivo* dosimetry[100-111]. At CCMB, dose reconstructions for the pre-treatment cases are carried out using the patient's planning CT data. The process is similar to the *in vivo* approach but the EPID images are acquired without a patient in the beam. The dose measured in an EPID image is converted to incident fluence, corrected for non-primary beam components (such as patient scatter), then back-projected to a plane above the patient (accounting for the inverse square effect and attenuation). This fluence estimate is then used to calculate dose to the patient CT data.

Inverse EPID *in vivo* dosimetry for VMAT has really only been reported by two other groups in the world, one based out of Rome, Italy at the Instituto di Fisica, Università Cattolica del Sacro Cuore, who estimate point doses at isocentre, and another from The Netherlands Cancer Institute-Antoni van Leeuwenhoek Hospital, in Amsterdam performing full 3D dose estimates. Both will be discussed in the following sections respectively.

2.5.1 Instituto di Fisica, Università Cattolica del Sacro Cuore model

This Italian group have developed an inverse EPID method which calculates an *in vivo* isocentre and mid-plane point dose[100]. The mid-plane dose calculation is derived via a number of empirically determined correlation functions. These functions are derived from the ratios of EPID measured transit signals (average of the 25 central pixels) to water phantom doses measured by an ion chamber. The chamber was placed at isocentre for varying phantom thicknesses and square field sizes. The EPID transit signals were converted to calibrated units using Varian's PortalVision software. Data from varying field sizes and phantom thickness were then fitted to a 3rd order polynomial given as a function of square field length. From these measurements, an empirically derived scatter contribution to the transit signal was determined as a function of field size and patient-to-EPID distance. An inverse square effect is also included. Heterogeneities were accounted for by adding an equivalent water thickness to the inverse square distance. The isocentre dose was calculated using the same derived empirical function except tissue-maximum ratios were used instead of just the inverse square law. The isocentre mid-plane point doses were then compared to the TPS calculated doses at the same points.

Application to VMAT delivery was determined by completing the same measurements over a range of gantry angles. Piermattei *et al*. compared the isocentre dose determined by their model to the TPS for a partial arc VMAT lung SBRT patient. The isocentric dose calculated within the patient was always within ± 5% of the dose determined by the TPS[101]. Fidanzio *et al.* determined the same isocentric dosimetric accuracy with the TPS by comparing the model to prostate, pancreas, and head-and-neck VMAT plans[102]. Peca and

Brown built on the original model developed by Piermattei *et al.* and investigated the variability of the EPID transit signal to patient isocentre dose ratio in water phantoms of varying thickness and field sizes to design a field edge dose correction factor[103], allowing for a 2D planar dose calculation at isocentre. However, this was limited to simple fields with no MLC modulation.

Overall, this model is not very robust, has no volumetric dosimetry information, and can only be applied to very simplistic delivery scenarios. Furthermore, the calculations are derived entirely from empirical correlation factors determined at a single point in time. There is no modeling of the MLC modulation and only an interpolation of the central MLC leaves (either open or closed) for the isocentric dose calculation. Although the model can quickly calculate an isocentric and isoplanar dose, it lacks a 3D calculation option, thus limiting its clinical usefulness.

2.5.2 Antoni van Leeuwenhoek Hospital inverse EPID in vivo model

The Dutch group at the Antoni van Leeuwenhoek hospital have developed an inverse EPID model that can calculate both 3D *in vivo* and pre-treatment doses for VMAT. They have significant experience in this field and thus warrant a more in-depth discussion. The core *in vivo* back-projection model was developed for IMRT treatments using SLIC EPIDs[97] and was later adapted for IMRT treatments using aSi EPIDs[105,106]. Recently, it has been adapted for VMAT treatments using an aSi EPID[107-111]. The basic model incorporates a large set of empirical correction factors which account for: (i) the dose response of the EPID, (ii) the lateral scatter within the EPID, (iii) the scatter from the patient (or phantom) to the EPID,

(iv) the scatter within the patient, and (v) the attenuation of the beam through the patient. Empirically fit functions to central axis profiles measured with ion chambers provided the correction factors for (i), (ii), and (iv). The general processing of each EPID image that is used to reconstruct the *in vivo* dose is discussed below.

The measured EPID image is converted from grayscale to dose via the correction factor (i). The lateral scatter within the EPID dose image is handled by a deconvolution with an EPID scatter kernel, K_1, which was determined via point dose measurements. In order to better model the out-of-field profile effects at the plane of the EPID (i.e., penumbra) a second convolution with a different EPID scatter kernel, K_2, was performed on the deconvolution result. The K_1 kernel was determined from matching central axis values of ion chamber measurements to EPID images and the K_2 kernel was derived from the comparison of EPID dose profiles and film measurements. The scatter factor due to the patient was determined by a transmission ratio of the EPID dose image with the patient to the EPID dose image without the patient and correcting for attenuation. This required another EPID image to be taken without the patient present in order to determine the primary dose to the EPID. This primary dose was back-projected to a midpoint plane within the patient via attenuation and inverse square correction. The patient scatter component of the total patient dose was determined by the convolution of an empirical kernel with the back-projected primary dose.

An extension to calculate the 3D *in vivo* dose was implemented by the group[106]. The process described above was calculated for multiple patient planes which could be summed to provide a 3D dose. For this approach, a water thickness was used, determined from

contours of the patient's CT data. This unfortunately did not account for patient heterogeneities. Beam hardening was modeled as an attenuation correction and depth dependence was added to the function which determined scatter within the patient. Furthermore, in order to improve the overall accuracy, an empirically-based entrance dose build-up model was also added.

Adaptation to VMAT required sampling multiple images as opposed to just 5 or 9 EPID images required for standard IMRT[107]. Time-dependent, gantry angle resolved images are required in order to accurately reconstruct a VMAT *in vivo* dose. Furthermore, dose rate modulations and continuous gantry movement make the transmission ratio approach to remove patient scatter in the EPID, described above, impossible for VMAT. Since the transmission depends on the gantry angle it is recalculated for every frame (i.e., every gantry angle) directly from a radiological pathlength calculation using ray-tracing through planning CT data. The CT data used to calculate the radiological thicknesses consisted entirely of water and were contoured to the same shape of the patient's planning CT data. The primary transmission, T^{prim}, to the EPID is then calculated using:

$$T^{prim} = e^{-(\mu \cdot t + \sigma \cdot t^2)} \qquad [2.15]$$

where μ is linear attenuation coefficient, t is the radiological thickness, and σ is a beam hardening correction factor. These transmissions are calculated for every pixel on the EPID.

In order to continue using the same water-based reconstruction model and handle heterogeneities each measured EPID image was converted to an image that would have been measured if the same patient had consisted entirely of water[108]. As described in Eq. 2.15 the radiological pathlength through the patient's CT volume provides the EPID transmission. The *geometrical* pathlength through the same CT volume consisting entirely of water determines the EPID transmission of a water-like patient. A transmission conversion factor (TCF) matrix equal to the ratio of the transmission matrix due to the actual patient CT data and the transmission matrix due to the water is calculated. This TCF matrix is multiplied by the measured primary portal dose image to produce an in-water primary portal dose image. The process described above is performed on every image acquired, back-projected to multiple patient planes as described above, and then each contributing image dose is summed up in the patient in order to determine the total *in vivo* 3D dose. This dose is then compared to the TPS calculated dose for verification.

This Dutch group's model performs reasonably well and has been reported on in literature for many different types of IMRT/VMAT deliveries and heterogeneities[107,108,110]. They have just recently started to implement an automatic dose verification system in their clinic for all treatment-types which would deliver dose reports minutes after a treatment[109,111]. However, the majority of their prediction method is derived from empirical fits to measured data as opposed to model-based methods utilizing fundamental radiation physics. A model-based approach should provide a more robust system that could be easily generalized to accurately handle more complex patient hetereogeneities and geometries.

The approach used in this thesis, described in detail in Section 2.2.4, is a model utilizing underlying radiation physics to estimate *in vivo* dose reconstruction in the patient using on-treatment EPID images. It incorporates several Monte Carlo derived data sets and utilizes our thorough understanding of the underlying physics of the radiation transport through the linac, patient, and imaging system, to provide an accurate, robust, and easily generalizable model to estimate 3D dose to the patient, based on measured transmission EPID images. MLC interleaf leakage and rounded leaf tips are accurately modeled based on manufacturer schematics. The attenuation of the beam through the patient is calculated directly through radiological pathlengths determined from the patient's CT data in order to accurately account for heterogeneities. The patient scatter incident on the EPID is determined via Monte Carlo determined patient scatter fluence kernels. The dose deposition at the EPID is also calculated from Monte Carlo determined EPID-specific dose kernels. The predicted fluences to the EPID from our physical model are used to analyse the actual measured EPID doses and provide an accurate estimate of delivered dose to the patient.

2.6 THESIS SUMMARY

VMAT delivery is a complex treatment delivery method involving dose-rate and MLC modulation while the linac gantry rotates around the patient. An *in vivo* verification of each delivered fraction would be beneficial to overall patient safety. This benefit is magnified when delivering SBRT-VMAT treatments, which use substantially higher doses per fraction

than conventional VMAT, because any error during delivery could be more detrimental to the patient. This model is used for both offline and real-time verification applications.

In Chapter three, a measure of the linac's EPID support arm mechanical 'sag' was investigated. Due to the mass of the support arm, it's positioning is affected by gravity and this creates a 2D imager spatial offset that varies with gantry angle. Because the dose data provided in a measured EPID image is required, any geometrical offset in the image data will systematically affect the dose reconstruction model. EPID in-plane (*y*-axis) and cross-plane (*x*-axis) sag corrections were determined. The *x*-axis sag was found to be negligible, while the in-plane sag required a correction which was implemented into the reconstruction model. This was a joint investigation performed with our collaborators located at the Calvary Mater Newcastle Hospital located in Newcastle, Australia. This correction was incorporated into our *in vivo* patient dose reconstruction model.

In Chapter four, an investigation of the accuracy of the EPID image's associated gantry angle is discussed. The linac's gantry is continuously rotating during VMAT delivery and a precise angle per EPID image is required in order to accurately reconstruct the dose to the patient. An inaccurate gantry angle will limit the geometric accuracy of our back-projection calculation. Similar to Chapter 3, this is an important characterization of the linac's geometry during VMAT delivery. Each EPID image acquired by the clinical software has a gantry angle written in its header, but these were found to be incorrect by as much as ±3°. Using an in-house constructed phantom, an incremental encoder, and acquiring the linac's actual gantry angle signal from a potentiometer, provided an accurate characterization of the linac's

gantry angle. This allowed us to create an angle adjustment correction algorithm which improves the angle accuracy of each EPID image to within ±1° of the true gantry angle. Many methods of correction were investigated but the simplest approach was to correct for an initial timing offset and then apply a smoothing function to the header angle data of each arc. This approach was also incorporated into our *in vivo* patient dose reconstruction model. The results of Chapters three and four characterized the linac's geometry during VMAT delivery.

Chapter five, the most important chapter in the thesis, answers the hypothesis by describing the processes involved in creating and validating an SBRT-VMAT linac prediction model, using EPID images, for *in vivo* dose verification. This was required as the SBRT beam, although nominally 6MV, utilizes a different flattening filter compared to the non-SBRT 6 MV beam, and has significantly different dosimetric properties. This includes Monte Carlo modeling of the linac and validation with experimental data, optimization of the focal and extra-focal fluence functions via measured EPID data, and finally a validation of the created model with patient data. From the first two steps, a forward model of an SBRT linac beam was created. Validation for the last step was carried out by comparing the inverse reconstructed dose of seven different types of SBRT-VMAT patient plans delivered to an anthropomorphic phantom and two patient plans to the Eclipse TPS dose calculation. Comparisons were carried out using a χ-comparison criteria of 2% dose difference and 2mm distance-to-agreement.

In Chapter six, an investigation into the optimization of EPID frame averaging is discussed. Each EPID *image* acquired in cine-mode is an average of a select number of EPID

frames. The number of frames to be averaged into an image can be adjusted by the user. This was investigated using a dedicated "frame-grabber" PC connected to the frame processing board of the treatment computer. The frame-grabber acquires single frames for an entire arc and saves them to the computer. Various amounts of frame-averaging were emulated using in-house software. An inverse patient dose reconstruction was performed for each frame-averaged EPID image set for twelve different VMAT and SBRT-VMAT plans. The motivation for this work was to determine a frame averaging value, as a function of treatment type and disease site that maintains an adequate level of accuracy in the patient dose reconstruction. A benefit of increased frame averaging (i.e., less overall EPID images per arc) is a decrease in the dose reconstruction calculation time because the calculation time is linearly dependent on the number of EPID images acquired per treatment.

Chapter seven summarizes the thesis and discusses future investigations building on the work done in this thesis and its applicability to the CCMB EPID dosimetry group.

The appendix (Chapter 8) contains elaborations of some topics of potential interest to the reader. These topics include a brief description of electron- and photon-matter interactions relevant to medical physics, a discussion on image comparison techniques (i.e., γ and χ-comparisons), an in-depth analysis and validation of our model's implemented collapsed cone convolution patient dose algorithm, and a glossary of commonly used terms.

REFERENCES

1. Verhaegen, F. and Seuntjens, J. *Monte Carlo modelling of external radiotherapy photon beams,* Phys Med Biol, 2003, **48** p.R107-R164.

2. Ma, C. M., Mok, E., Kapur, A., Pawlicki, T., Findley, D., Brain, S., Forster, K., and Boyer, A. L., *Clinical implementation of a Monte Carlo treatment planning system.* Med Phys, 1999, **26**(10), p. 2133-43.
3. Ma, C. M., Li, J. S., Pawlicki, T., Jiang, S. B., Deng, J., Lee, M. C., Koumrian, T., Luxton, M., and Brain, S., *A Monte Carlo dose calculation tool for radiotherapy treatment planning*, Phys Med Bio., 2002, **47**(10), p. 1671-89.
4. Fragoso M., Wen N., Kumar S., Liu D, Ryu S, Movsas B., Munther A., and Chetty IJ., *Dosimetric verification and clinical evaluation of a new commercially available Monte Carlo-based dose algorithm for application in stereotactic body radiation therapy (SBRT) treatment planning*, Phys Med Biol., 2010, **55**(16), p.4445-64.
5. Jia X., Gu X., Graves Y.J., Folkerts M., and Jiang, S.B., *GPU-based fast Monte Carlo simulation for radiotherapy dose calculation*, Phys Med Biol, 2011, **56**(22), p.7017-31.
6. The EGS4 Code System, Stanford Linear Accelerator Center: Stanford, California.1985.
7. Kawarakow, I., Mainegra-Hing, E., Rogers, D. W. O., Tessier, F., and Walters, B. R. B., *The EGSnrc code system: Monte Carlo simulation of electron and photon transport*, Ionizing Radiation Standards, National Research Council of Canada, 2010.
8. Rogers, D. W. O., Faddegon, B. A., Ding, G. X., Ma, C. M., We, J., and Mackie, T. R., *BEAM: a Monte Carlo code to simulate radiotherapy treatment units*. Med Phys, 1995. **22**(5), p. 503-24.
9. Sheikh-Bagheri, D. and Rogers, D. W. O., *Monte Carlo calculation of nine megavoltage photon beam spectra using the BEAM code*. Med Phys, 2002. **29**(3), p. 391-402.
10. Ahnesjo, A., *Analytic modeling of photon scatter from flattening filters in photon therapy beam*, Med Phys, 1994. **21**(8), p. 1227-35.
11. Ahnesjo, A., *Collimator scatter in photon therapy beams,* Med Phys, 1995. **22**(3), p. 267-78.
12. Ahnesjo, A., Saxner, M., and Trepp, A., *A pencil beam model for photon dose calculation*, Med Phys, 1992, **19**(2), p. 263-73.
13. Ahnesjo, A., Weber, L., Murman, A., Saxner, M., Thorslund, I., and Traneus, E., *Beam modeling and verification of a photon beam multisource model.* Med Phys, 2005, **32**(6), p. 1722-37.
14. Ahnesjo, A., Weber, L., and Nilsson, P., *Modeling transmission and scatter for photon beam attenuators.* Med Phys, 1995, **22**(11, Pt. 1), p. 1711-20.
15. Jaffray, D. A., Battista, J. J., Fenster, A., and Munro, P., *X-ray sources of medical linear accelerators: focal and extra-focal radiation.* Med Phys, 1993, **20**(5), p. 1417-27.
16. Sharpe, M. B., Jaffray, D. A., Battista, J. J., and Munro, P., *Extrafocal radiation: a unified approach to the prediction of beam penumbra and output factors for megavoltage x-ray beams.* Med Phys, 1995, **22**(12), p. 2065-74.
17. Liu, H., Mackie, T.R., McCullough, E.C., *A dual source photon beam model used in convolution/superposition dose calculations for clinical megavoltage x-ray beams*, Med Phys, 1997, **24**(12), p.1960-74.
18. Mackie, T. R., Scrimger, J. W., and Battista, J. J., *A convolution method of calculating dose for 15-MV x rays*, Med Phys, 1985, **12**(2), p. 188-96.
19. Papanikolaou, N., Mackie, T. R., Meger-Wells, C., Gehring, M., and Reckwerdt, P., *Investigation of the convolution method for polyenergetic spectra*, Med Phys, 1993, **20**(5), p. 1327-1336.

20. Sievinen, J., Ulmer, W. and Kaissl, W., *AAA photon dose calculation model in Eclipse*, Varian Medical Systems, RAD#7170A.
21. Ulmer, W. and Harder., D, *A triple Gaussian pencil beam model for photon beam treatment planning*, Med Phys, 1995, **5**, p. 25-30.
22. Ulmer, W. and Harder., *Application of a triple Gaussian pencil beam model for photon beam treatment planning*, Med Phys, 1996, **6**, p. 68-74.
23. McCurdy, B.M., and Pistorius, S., *Photon scatter in portal images: accuracy of a fluence based pencil beam superposition algorithm*, Med Phys, 2000, **27**(5), p.913-22.
24. McCurdy, B.M., and Pistorius, S., *A two-step algorithm for predicting portal dose images in arbitrary detectors*, Med Phys, 2000, **27**(9), p. 2109-16.
25. McCurdy, B.M., Luchka, K., and Pistorius, S., *Dosimetric investigation and portal dose image prediction using an amorphous silicon electronic portal imaging device*, Med Phys, 2001, **28**(6), p. 911-24.
26. Chytyk, K., and McCurdy B.M., *Investigation of tilted dose kernels for portal dose prediction in a-Si electronic portal imagers*, Med Phys, 2006, **33**(9), p. 3333-9.
27. Chytyk, K., and McCurdy, B.M., *Comprehensive fluence model for absolute portal dose image prediction*, Med Phys, 2009, **36**(4), p. 1389-98.
28. McCurdy B.M., and Greer, P.B., *Dosimetric properties of an amorphous-silicon EPID used in continuous acquisition mode for application to dynamic and arc IMRT*, Med Phys, 2009, **36**(7), p. 3028-39.
29. Rowshanfarzad, P., McCurdy B.M., Sabet, M., Lee C., O`Connor, D.J., and Greer, P.B., *Measurement and modeling of the effect of support arm backscatter on dosimetry with a varian EPID*, Med Phys, 2010, **37**(5), p. 2269-78.
30. Chytyk-Praznik, K., VanUytven, E., vanBeek, T.A, Greer, P.B., and McCurdy, B.M., *Model-based prediction of portal dose images during patient treatment*, Med Phys, 2013, **40**(3), p. 031713.
31. VanUytven, E., vanBeek, T.A., McCowan, P.M., Chytyk-Praznik, K., Greer, P.B., and McCurdy B.M., *Validation of a method for in vivo 3D dose reconstruction for IMRT and VMAT treatments using on-treatment EPID images and a model-based forward-calculation algorithm*, Med Phys 2015, **42**(12), p.6945-54..
32. Philips Medical Systems, *Pinnacle^3 Physics Reference Guide, Release 7.6*, 2005.
33. Ahnesjo, A., *Collapsed cone convolution of radiant energy for photon dose calculation in heterogeneous media*, Med Phys, 1989, **16**, p. 577-592.
34. Krieger, T., and Sauer, O.A, *Monte-Carlo versus pencil-beam/collapsed-cone dose calculation in heterogeneous multi-layer phantom*, Phys Med Biol, 2005, **50**(5), p. 859-68.
35. Hasenbalg, F., Neuenschwander, H., Mini, R., and Born, E.J., *Collapsed cone and analytical anisotropic algorithm dose calculations compared to VMC++ Monte carlo simulations in clinical cases*, Journal of Physics: Conference Series **74**, (2007), 012007.
36. Fotina,I., Winkler, P., Kunzler T., Reiterer, J., and Georg, D., *Advanced kernel methods vs. Monte Carlo-based dose calculation for high energy photon beams*, Radiother Oncol, 2009, **93**(3), p. 645-53.
37. Chow, J.C.L., Jiang, R., and Leung, M., *Dosimetry of oblique tangential photon beams calculated by superposition/convolution algorithms: a Monte Carlo evaluation*, J Appl Clin Med Phys, 2010, **12**(1), p. 108-21.

38. Siddon, R.L., *Fast calculation of the exact radiological path for a three dimensional CT array*, Med Phys, 1985, **12**(2), p. 252–255.
39. Kirky, C., and Sloboda, R., *Comprehensive Monte Carlo calculation of the point spread function for a commercial a-Si EPID*, Med Phys, 2005, **32**, p. 1115-27.
40. McNutt, T.R., Mackie, T.R., and Paliwal, B.R., *Analysis and convergence of the iterative convolution/superposition dose reconstruction technique for multiple treatment beams and tomotherapy*, Med Phys, 1997, **24**, p. 1465-1476.
41. McNutt, T.R., Mackie, T.R., Reckwerdt, P., and Paliwal, B.R., *Modeling dose distributions from portal dose images using the convolution/superposition method*, Med Phys, 1996, **23**(8), p. 1381-92.
42. Laub, W.U., and Wong, T., *The volume effect of detectors in the dosimetry of small fields used in IMRT*, Med Phys, 2003, **30**(3), p. 341-47.
43. Wuerfel, J.U., *Dose measurements in small fields*, Med Phys It'l. J., 2013, **1**(1), p.81-90.
44. Low, D.A., Harms, W.B., Mutic, S., and Purdy, J.A., *A technique for the quantitative evaluation of dose distributions*, Med Phys, 1998, **25**, p.656-61.
45. McDermott, L., Wendling, M., Sonke, J., Vanherk, M., and Mijnheer, B., *Replacing Pretreatment Verification With In Vivo EPID Dosimetry for Prostate IMRT*, Int J Radiat Oncol Biol Phys, 2007, **67**(5), p. 1568-77.
46. Mans, A., Wendling, M., McDermott, L. N., Sonke, J. J., Tielenburg, R., Vijlbrief, R., Mijnheer, B., van Herk, M., and Stroom, J. C., *Catching errors with in vivo EPID dosimetry*, Med Phys, 2010, **37**(6), p. 2638-44.
47. McDermott, L., Wendling, M., Nijkamp, J., Mans, A., Sonke, J., Mijnheer, B., and Vanherk, M., *3D in vivo dose verification of entire hypo-fractionated IMRT treatments using an EPID and cone-beam CT*, Radiother Oncol, 2008, **86**(1), p. 35-42.
48. van Zijtveld, M., Dirkx, M., Breuers, M., de Boer, H., and Heijmen, B., *Portal dose image prediction for in vivo treatment verification completely based on EPID measurements*, Med Phys, 2009, **36**, p. 946-952.
49. Liu, B., Adamson, J., Rodriguez, A., Zhou, F., Yin F.F., Wu, Q., *A novel technique for VMAT QA with EPID in cine mode on a Varian TrueBeam linac*, Phys Med Biol, 2013, **58**(19), p.6683-700.
50. Bakhtiari, M., Kumaraswamy, L., Bailey D.W., de Boer, S, Malhotra, H.K., Podgorsak, M.B., *Using an EPID for patient-specific VMAT quality assurance*, Med Phys, 2011, **38**(3), p.1366-73.
51. Bailey, D.W., Kumaraswamy, L., Bakhtiari, M., Molhotra, H.K., and Podgorsak, M.B., *EPID dosimetry for pretreatment quality assurance with two commercial systems*, J Appl Clin Med Phys, 2012, **13**(4), p.82-99.
52. Greer, P.B., *3D EPID based dosimetry for pre-treatment verification of VMAT – methods and challenges*, Journal of Physics: Conference Series 444 (2013), 012010.
53. Fricke, H. and Hart, E. L., *The chemical action of roentgen rays on dilute ferrosulphate solutions as a measure of dose*, Am J Roentgenol Radium Ther Nucl Med, 1927, **18**, p.430-432.
54. Low, D.A., Moran, J.M., Dempsey, J.F., Dong, L., and Oldham, M., *Dosimetry tools and techniques for IMRT*, Med Phys, 2011, **38**(3), p.1313-38.
55. Dieterich, S., and Sherouse, G.W., *Comparison of seven commercial dosimetry diodes for SRS*, Med Phys, 2011, **38**(7), p.4166-4173.

56. Chuang, C.F., Verhey, L.J., and Xia, P., *Investigation of the used of MOSFET for clinical IMRT dosimetric verification*, Med Phys, 2002, **29**, p.1109-1115.
57. Rustgi, S.N., *Evaluation of the dosimetric characteristics of a diamond detector for photon beam measurements.* Med Phys., 1995, **22**, p.567-570.
58. Warkentin, B., Steciw, S., Rathee, S., and Fallone, B.G., *Dosimetric IMRT verification with a flat-panel EPID*, Med Phys, 2003, **30**(12), p. 3143-55.
59. Van Esch, A., Depuydt, T., and Huyskens, D. P., *The use of an aSi-based EPID for routine absolute dosimetric pre-treatment verification of dynamic IMRT fields*, Radiother Oncol, 2004, **71**(2), p.223-34.
60. Bedford, J.L., Lee, Y.K., Wai, P., South, C.P., and Warrington, A.P., *Evaluation of the Delta4 phantom for IMRT and VMAT verification*, Phys Med Biol, 2009, **54**, p.N167-176.
61. Van Esch, A., Basta, K., Evrard, M., Ghislain, M., Sergent, F., Huyskens, D.P., *The Octavius1500 2D ion chamber array and its associated phantoms: Dosimetric characterization of a new prototype*, Med Phys, 2014, **41**(9): p. 091708.
62. Boggula, R. *et al.*, *Experimental validation of a commercial 3D dose verification system for intensity-modulated arc therapies*, Phys Med Biol, 2010, **55**(19), p. 5619-33.
63. Chaswal, V., Weldon, M., Gupta, N., Chakravarti, A., and Ronga, Y., *Commissioning and comprehensive evaluation of the ArcCHECK cylindrical diode array for VMAT pretreatment delivery QA*, J App Clin Med Phys, 2014, **15**(4), p. 212-225.
64. Li G, *et al. Evaluation of the ArcCHECK QA system for IMRT and VMAT verification*. Phys Med, 2013, **29**(3), p.295–303.
65. Nicolini, G., *et al*., The *GLAaS – an absolute dose calibration algorithm for an amorphous silicon portal imager. Aplications to IMRT verification*, Med Phys, 2006, **33**, p.2839-51.
66. Nicolini, G., *et al*., The *GLAaS algorithm for portal dosimetry and quality assurance of RapidArc, an intensity modulated rotational therapy*, Radiother Oncol, 2008, **3**(24), doi: 10.1186/1748-717X-3-24.
67. Fredh, A., Scherman, J.B., Fog, L.S., and af Rosenschöld, P.M., *Patient QA systems for rotational radiation therapy: A comparative experimental study with intentional errors*, Med Phys, 2013, **40**(3), p.031716.
68. Baldock, C., De Deene, Y., Doran, S., Ibbott, G., Jirasek, A., Lepage, M., McAuley, K. B., Oldham, M., and Schreiner, L.J., *Polymer gel dosimetry*, Phys Med Biol, 2010, **55**(5), p. R1-R63.
69. Ceberg, S., Gagne, I., Gustafsson, H., Scherman, J.B., and Korreman, S.S., *RapidArc treatment verification in 3D using polymer gel dosimetry and Monte Carlo simulation*, Phys Med Biol, 2010, **55**(17), p. 4885-98.
70. Sakhalkar, H.S., Adamovics, J., Ibbott, G., and Oldham, M., *A comprehensive evaluation of the PRESAGE/optical-CT 3D dosimetry system*, Med Phys, 2009, **36**(1), p. 71-82.
71. Adamson, J. *et al.*, *On the feasibility of polyurethane based 3D dosimeters with optical CT for dosimetric verification of low energy photon brachytherapy seeds*, Med Phys, 2014, **41**(7), p.071705.
72. Goulet, M., Rilling, M., Gingras, L., Beddar, S., Beaulieu, L., and Archambault, L., *Novel, full 3D scintillation dosimetry using a static plenoptic camera*, Med Phys, 2014, **41**(8), p.082101.

73. Langmack, K.A., *Portal imaging*, Br J Radiol, 2001, **74**(885), p.789-804.
74. Antonuk, L.E., *Electronic portal imaging devices: a review and historical perspective of contemporary technologies and research*, Phys Med Biol, 2002, **47**(6), p.R31-65.
75. Kirby, M.C., and Glendinning, A.G., *Developments in electronic portal imaging systems*, Br J Radiol, 2006, **79**(1), p.S50-65.
76. Heijmen, B.J., Pasma, K L., Kroonwijk, M., Althof, V.G., de Boer, J.C., Visser, A.G., and Huizenga, H., *Portal dose measurement in radiotherapy using an electronic portal imaging device (EPID)*, Phys Med Biol, 1995, **40**(11), p.1943-55.
77. Meertens, H., van Herk, M., and Weeda, J., *A liquid ionisation detector for digital radiography of therapeutic megavoltage photon beams*, Phys Med Biol, 1985, **30**(4), p. 313-21.
78. Meertens, H., van Herk, M., Bijhold, J., and Bartelink, H., *First clinical experience with a newly developed electronic portal imaging device*, Int J Radiat Oncol Biol Phys, 1990, **18**(5), p. 1173-81.
79. van Herk, M. and Meertens, H., *A matrix ionisation chamber imaging device for on-line patient setup verification during radiotherapy*, Radiother Oncol, 1988, **11**(4), p. 369-78.
80. van Herk, M., *Physical aspects of a liquid-filled ionization chamber with pulsed polarizing voltage*, Med Phys, 1991, **18**(4), p. 692-702.
81. van Herk, M., Bijhold, J., Hoogervorst, B., and Meertens, H., *Sampling methods for a matrix ionization chamber system*, Med Phys, 1992, **19**(2), p. 409-18.
82. Greer, P.B. and Popescu, C.C., *Dosimetric properties of an amorphous silicon electronic portal imaging device for verification of dynamic intensity modulated radiation therapy*, Med Phys, 2003, **30**(7), p.1618-27.
83. Herman, M.G., Balter, J.M., Jaffray, D.A., McGee, K.P., Munro, P., Shalev, S., Van Herk, M., and Wong, J.W., *Clinical use of electronic portal imaging: Report of AAPM Radiation Therapy Committee Task Group 58*, Med Phys, 2001, **28**(5), p.712.
84. Munro, P. and Bouius, D.C., *X-ray quantum limited portal imaging using amorphous silicon flat-panel arrays*, Med Phys, 1998, **25**(5), p.689-702.
85. Winkler, P., Hefner, A., and Georg, D., *Dose-response characteristics of an amorphous silicon EPID*, Med Phys, 2005, **32**(10), p.3095-105.
86. McDermott, L.N., Louwe, R.J.W., Sonke, J J., van Herk, M.B., and Mijnheer, B.J., *Dose–response and ghosting effects of an amorphous silicon electronic portal imaging device*, Med Phys, 2004, **31**(2), p.285-95.
87. Sabet, M., Menk, F.W., and Greer, P.B., *Evaluation of an a-Si EPID in direct detection configuration as a water-equivalent dosimeter for transit dosimetry*, Med Phys, 2010, **37**(4), p.1459-67.
88. Podesta, M., Nijsten, S.M., Snaith, J., Orlandini, M., Emans, D., Aland T., and Verhaegen, F., *Measured vs simulated portal images for low MU fields on three accelerator types: possible consequences for 2D portal dosimetry*, Med Phys, 2012, **39**(12), p. 7470-9.
89. Jaffray, D.A., Battista, J.J., Fenster, A., and Munro, P., *X-ray scatter in megavoltage transmission radiography: physical characteristics and influence on image quality*, Med Phys, 1994, **21**(1), p.45-60.
90. Greer, P.B., Vial, P., Oliver, L., and Baldock C., *Experimental investigation of the response of an amorphous silicon EPID to intensity modulated radiotherapy beams*, Med Phys, 2007, **34**(11), p.4389-98.

91. Zwan, B.J., King B.W., O'Connor, D.J., and Greer, P.B., *Dose-to-water conversions for the backscatter-shielded EPID: a frame-based method to correct for EPID energy response to MLC transmitted radiation*, Med Phys, 2014, **41**(8), p.081716.
92. Greer, P.B., *Correction of pixel sensitivity variation and off-axis response for amorphous silicon EPID dosimetry*, Med Phys, 2005, **32**(12), p.3558-68.
93. Woodruff, H.C., Fuangrod, T., Rowshanfarzad, P., McCurdy, B.M.C., and Greer, P.B., *Gantry-angle resolved VMAT pretreatment verification using EPID image prediction*, Med Phys, 2013, **40**, p.081715.
94. Ansbacher, W., Gagne, I.M., and Swift, C-L., *A comprehensive EPID-based 3D validation technique for TrueBeam VMAT plans*, Journal of Physics: Conference Series, 2014, 489, p.012067.
95. Podesta, M., Nijsten, S.M., Persoon, L.C., Scheib, S.G., Baltes, C., and Verhaegen, F., *Time dependent pre-treatment EPID dosimetry for standard and FFF VMAT*, Phys Med Biol, 2014, **59**(14), p.4749-68.
96. Gimeno, J. *et al*., *Commissioning and initial experience with a commercial software for in vivo volumetric dosimetry*, Phys Med, 2014, pii: S1120-1797(14)00108-2.
97. van Elmpt, W.J.C., Nijsten, S.M.J.J.G., Mijnheer, B.J., and Minken, A.W.H., *Experimental verification of a portal dose prediction model*, Med Phys, 2005, **32**(9), p.2805-18.
98. Bedford, J.L., Hanson, I.M., and Hansen, V.N., *Portal dosimetry for VMAT using integrated images obtained during treatment*, Med Phys, 2014, **41**(2), p.021725.
99. Fuangrod, T., Woodruff, H.C., Rowshanfarzad, P., O'Connor, D.J., Middleton, R.H., and Greer, P.B., *An independent system for rael-time dynamic multileaf collimation trajectory verification using EPID*, Phys Med Biol, 2014, **59**(1), p.61-81.
100. Piermattei, A., Fidanzio, A., Stimato, G., Azario, L., Grimaldi, L., D'Onofrio, G., Cilla, S., Balducci M., Gambacorta, M.A., Di Napoli, N., Cellini, N., *In vivo dosimetry by an aSi-based EPID*, Med Phys, 2006, **33**(11), p.4414-22.
101. Piermattei, A., *et al.*, *In patient dose reconstruction using cine acquisition for dynamic arc radiation therapy*, Med Biol Eng Comput, 2009, **47**, p.425–433.
102. Fidanzio, A., Porcelli, A., Azario, L., Greco, F., Cilla, S., Grusio, M., Balducci, M., Valentini, V., Piermattei, A., *Quasi real time in vivo dosimetry for VMAT*, Med Phys, 2014, **41**(6), p.062103.
103. Peca, S., and Brown, D.W., *Two-dimensional in vivo dose verification using portal imaging and correlation ratios*, J Appl Clin Med Phys, 2014, 489 (4), p.4752.
104. Boellaard, R., Essers, M., van Herk, M., and Mijnheer, B.J., *New method to obtain the midplane dose using portal in vivo dosimetr*, Int J Radiat Oncol Biol Phys, 1998, **41**(2), p.465-74.
105. Wendling, M., Louwe, R.J.W., McDermott, L.N., Sonke J-J., van Herk M., Mijnheer B.J., *Accurate two-dimensional IMRT verification using a back-projection EPID dosimetry method*, Med Phys, 2006, **33**, p.259–73.
106. Wendling, M., McDermott, L.N., Mans, A., Sonke, J-J., van Herk, M., Mijnheer, B., *A simple back-projection algorithm for 3D EPID dosimetry of IMRT treatments*, Med Phys, 2009, **36**, p.3310–21.
107. Mans, A., Remeijer, P., Olacirequi-Ruiz, I., Wendling, M., Sonke, J.J., Mijnheer B., van Herk, M., and Stroom, J.C., *3D Dosimetric verification of volumetric-modulated arc therapy by portal dosimetry*, Radiother Oncol, 2010, **94**(2), p.181-7.

108. Wendling, M., McDermott, L.N., Mans, A., Olacirequi-Ruiz, I., Pecharroman-Gallego, R., Sonke, J.J., van Herk, M., and Mijnheer B., *In aqua vivo EPID dosimetry*, Med Phys, 2012, **39**(1), p.367-77.
109. Olacirequi-Ruiz, I., Rozendall, R., Mijnheer B., van Herk, M., and Mans, A., *Automatic in vivo portal dosimetry of all treatments*, Phys Med Biol, 2013, **58**(22), p. 8253-64.
110. Rozendall, R., Mijnheer B., van Herk, M., and Mans, A., *In vivo portal dosimetry for head-and-neck VMAT and lung IMRT: Linking γ-analysis with differences in dose-volume histograms of the PTV*, Radiother Oncol, 2014, pii: S0167-8140(14)00164-9.
111. Hanson, I.M., Hansen, V.N., Olacirequi-Ruiz, I., and van Herk, M., *Clinical implementation and rapid commissioning of an EPID based in-vivo dosimetry system*, Phys Med Biol, 2014, **59**(19), p. N171-9.

CHAPTER THREE: THE CHARACTERIZATION OF GRAVITATIONAL SAG ON AN EPID DURING VMAT DELIVERY

This chapter discusses the characterization of EPID support arm sag, due to gravity, during treatment delivery. It will focus primarily on the work performed at CancerCare Manitoba (CCMB) as well as briefly discuss a combined investigation with our collaborators at the Calvary Mater Newcastle Hospital (CMNH) in Newcastle, Australia. Overall, this effect was investigated on three linacs at CCMB and four linacs at CMNH. A different measurement and analysis approach was carried out for the joint investigation but yielded the same results as this CCMB investigation. The joint investigation was published in the peer-reviewed journal *Medical Physics*. My contributions to the publication included experimental measurements and some analysis.

3.1 INTRODUCTION

Modern radiation treatment units consist of a linear accelerator (linac) with an electronic portal imaging device (EPID). The EPID was originally developed to verify the patient position via anatomical imaging with the treatment x-ray beam. However, the EPID has been shown to have properties attractive for use as a dosimetric verification tool[1,2]. Furthermore, its integration with the radiation treatment unit, sufficient spatial resolution, and digital output have made it the subject of several studies on dosimetry applications as discussed by van Elmpt *et al.* and references within[3]. The work presented here will build on our group's existing expertise in using EPIDs for dosimetry[2,4-9] (as discussed in Chapter 2) in order to

establish an accurate method for *in vivo* patient dose verification for volumetric modulated arc therapy (VMAT).

While the EPID has been shown to behave as a good dosimeter, it has only been studied in a single acquisition mode known as 'integration mode'. This acquisition mode results in the capture of a single image during an irradiation, and therefore would collapse all the time-dependent information delivered during a VMAT treatment into a single image. This is undesirable since one can therefore not reconstruct the delivered patient dose due to lack of information. McCurdy and Greer investigated the dosimetric properties of the EPID when operated in 'continuous mode' (also known as cine-mode), whereby a continuous acquisition of EPID frames or frame-averaged images are saved by the clinical computer during delivery. They demonstrated that, with some modification of the acquisition parameters and ensuring delivered doses were higher than about 70 MU (monitor units), typical of VMAT deliveries, the EPID would still exhibit good dosimetric properties[2].

Previous work by our group, involving three-dimensional patient dose reconstruction for IMRT delivery, is being extended to VMAT. The aim was to investigate the gravitational "sag" of the EPID support arm during VMAT delivery. This effect introduces positional error in EPID images which must be corrected for in order to achieve accurate patient dosimetry. The EPID sag will be characterized as a function of the linac's gantry angle.

3.2 MATERIALS AND METHODS

3.2.1 Data acquisition

The EPID sag was experimentally determined in two ways: firstly, an independent test carried out at our centre (CCMB) and secondly, a joint effort with our collaborating research facility Calvary Mater Newcastle Hospital (CMNH) in Newcastle, Australia (see discussion). For this chapter, the focus will be on the work carried out at CCMB which will then be compared to the CMNH results.

At CCMB a cubical phantom (4 cm^3) containing a tungsten ball-bearing (4.0 mm diameter) was set up at linac isocentre using the alignment lasers in the room (see Fig. 3.1). EPID images were acquired in continuous mode for 360 degree rotations. A VMAT plan was created in the Eclipse treatment planning system (Varian medical Systems, Palo Alto, CA) which delivered a 20x20 cm^2 field with no MLC modulation using a 6 MV beam, 700 MU, and a dose rate of 600 MU/min for a clockwise (CW) and counter-clockwise (CCW) arc. This measurement was performed on three different Varian 2100ix linacs. Furthermore, the same measurement was repeated six months later on one of the linacs in order to investigate reproducibility over time. All EPIDS were Varian model aS1000 EPIDs mounted on E-arm support arms. The EPID was centrally positioned at 150 cm source-to-detector distance (SDD) and 5 frames were averaged per image using Varian's integrated acquisition software (IAS3).

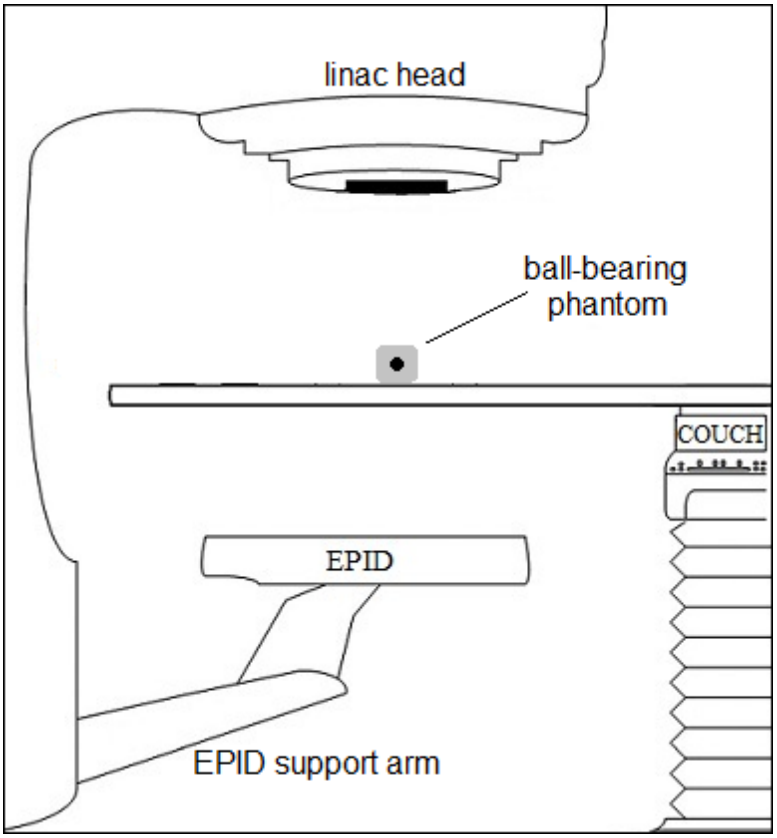

Fig.3.1 [Linac Experimental Setup]: Experimental setup for CCMB measurements of EPID sag.

3.2.2 Ball-bearing location detection

Each EPID image was cropped to a 40x40 pixel region centered on the central axis (CAX) of the EPID. The EPID's *x*-axis and *y*-axis ball-bearing coordinates of each image were determined via a 2D centroid (centre-of-intensity) calculation. The positions were calculated as a function of the linac's *average* gantry angle which was determined by dividing the total arc length by the number of images acquired per arc. This was an acceptable approximation due to the constant speed of the gantry for the created VMAT plan.

The centroid determined ball-bearing positions were sensitive to misalignments with the linac's true mechanical isocentre, either by human error and/or misaligned room lasers. This

will introduce geometric offsets as well as gravitational sag offsets in the determined ball-bearing positions. This effect is illustrated for clarity in Fig. 3.2 where linac coordinates are defined as *x*, *y*, and *z* and EPID coordinates are defined as *x* (cross-plane) and *y* (in-plane).

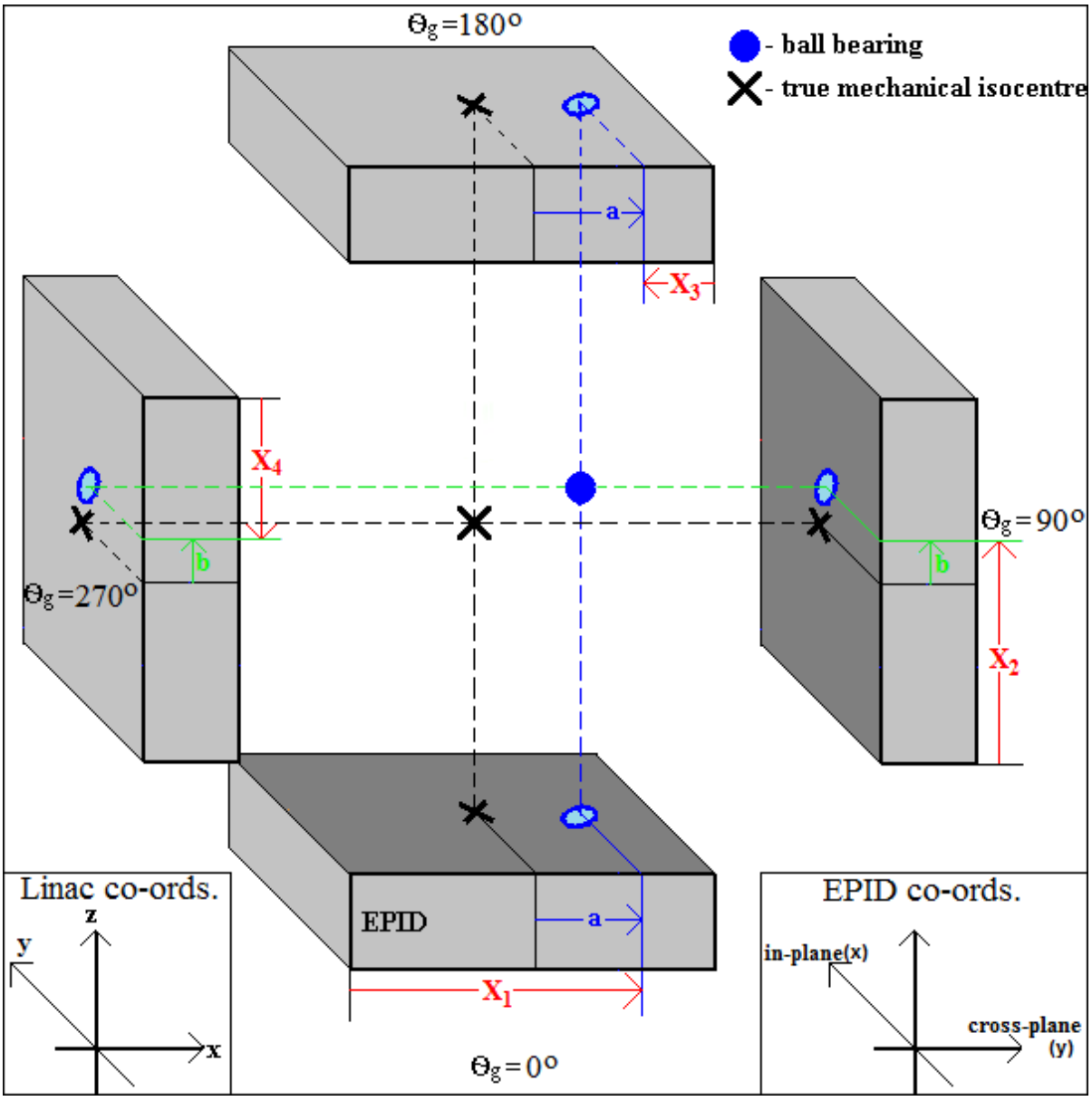

Fig. 3.2 [EPID Sag Geometry]: An illustration of the isocentre misalignments 'a' and 'b', for a linac's *x* and *z* axes respectively, at cardinal gantry angles, θ_g. X_1, X_2, X_3, and X_4 define the EPID's *x*-axis measurements determined by a centroid calculation.

It is observed that the EPID's *x*-axis measurement is sensitive to *x* and *z* axis misalignments with linac isocentre. Misalignments with the linac's *y*-axis do not affect the EPID's *x*-axis measurement because it is parallel to the linac's rotational axis. It is obvious from Fig. 3.2 that the EPID's *y*-axis measurement is invariant to any linac isocentre misalignments.

It is apparent from the geometry in Fig. 3.2 that the EPID's isocentre-corrected *x*-axis ball-bearing position, $X_{corr}(\theta_g)$, due only to gravitational sag is:

$$X_{corr}(\theta_g) = X_{meas}(\theta_g) - a \cdot cos\theta_g - b \cdot sin\theta_g \qquad [3.1]$$

where $X_{meas}(\theta_g)$ is the position determined from the centroid calculation of the EPID image as a function of the is the linac's gantry angle, θ_g. The constants 'a' and 'b' are the misalignments of the ball-bearing with isocentre in the linac's *x* and *z* axes respectively.

The linac's *x*-axis isocentre misalignment, 'a', was determined by taking integrated images of the ball-bearing at the static linac gantry angles 0° (X_1) and 180° (X_3) and performing a centroid calculation of each image's ball-bearing position. These were acquired prior to delivering the VMAT arc. From Fig. 3.2 it is clear then that 'a' is:

$$a = (X_1 - X_3)/2 \qquad [3.2]$$

The linac's *z*-axis isocentre misalignment 'b' cannot be determined like 'a' was because static gantry angle measurements at angles 90° and 270° would also include a gravitational

term, which needs to be isolated. The following process was used to characterize '*b*': the ball-bearing phantom was purposely misaligned from the linac's *z*-axis isocentre (defined by the room lasers) by a substantial amount (~5 mm), the centroid determined positions were then corrected for any *x*-axis linac isocentre misalignment, using Eq. 3.1 and 3.2, and then a Fourier analysis was performed in order to remove the *z*-axis linac isocentre misalignment. The Fourier analysis removed the first sinusoidal harmonic (fundamental) of the resulting ball-bearing position data (i.e., the lowest frequency component of the position data over the full range of gantry angles: -180° to 180°). The Fourier analysis was performed using MATLAB's (MathWorks Inc., Natick, MA) 'fft' (discrete fast Fourier transform) and 'ifft' (discrete inverse fast Fourier transform) functions. It subtracts the first harmonic from the discrete fast Fourier transform of the ball-bearing position data. The real part of the discrete inverse fast Fourier transform of the discrete fast Fourier transform, with the first harmonic removed, produces the ball-bearing positions corrected for *z*-axis linac isocentre misalignment. Unfortunately, this, or any other process (or any other experiment for that matter) cannot de-couple first order components due to the gravitational effect (if they exist) and the linac's *z*-axis isocentre alignment effect. Therefore, first order gravitational effects in the linac's *x*-axis and second order gravitational effects in the linac's *z*-axis and were determined for the EPID's cross-plane. This process, which was also performed and by the CCMB and CMNH study[10], and is illustrated in Fig. 3.3 for clarity.

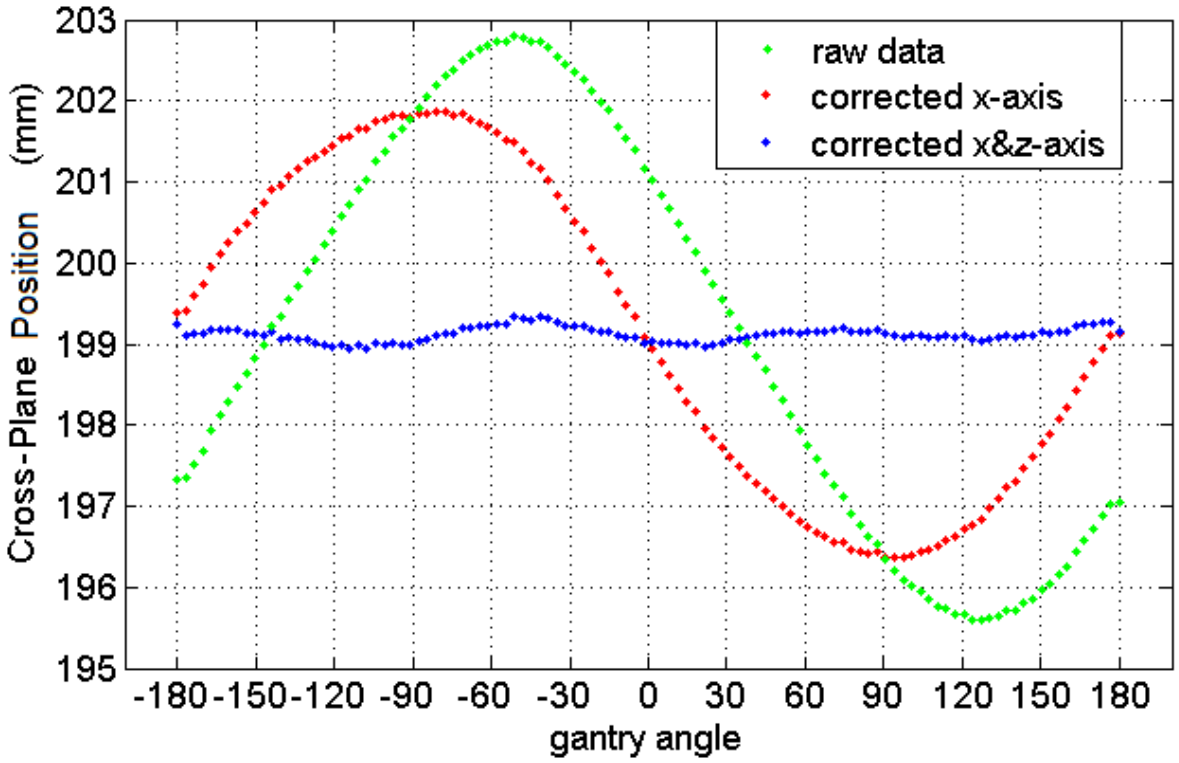

Fig. 3.3 [Isocentre Misalignment Corrections]: The centroid determined *x*-axis ball-bearing positions for a CCW arc are shown as the green curve. The linac's *x*-axis isocentre misalignment was corrected for using measured data and Eq. 3.1 (with b = 0) and 3.2 to produce the red curve. The linac's *z*-axis isocentre misalignment was corrected for by performing a Fourier analysis of the red data to remove the lowest frequency sinusoidal component (over the full range of gantry angles) to produce the EPID's *x*-axis ball-bearing position data due primarily to gravitational sag (blue data).

3.3 RESULTS AND DISCUSSION

The EPIDs *y*-axis and isocentre corrected *x*-axis ball-bearing positions, due to EPID sag are plotted as a function of the linac's gantry angle (-180° to 0° to 180° is the CCW direction and vice versa for CW) in Fig. 3.4 and 3.5 respectively. The average *maximum* displacement from isocentre of the ball bearing in the *y*-axis for all four measurements was 0.83 ± 0.04 mm, roughly two EPID pixels (each pixel is 400 mm/1024 pixels = 0.39 mm). The *y*-axis

ball-bearing positions were consistent and reproducible for all three linacs. The data followed a sinusoidal shape with gantry angle so a cosine function was fitted to all the data (black line in Fig. 3.4) and had the form:

$$-0.38 \cdot cos(0.98 \cdot \theta_g - 12°) \quad [3.3]$$

There was a slight angular asymmetry of the *y*-axis displacements and thus 12 degrees was included in the cosine argument for a better fit.

The average maximum displacement of the ball bearing position from isocentre for the EPIDs *x*-axis for all four measurements was 0.33 ± 0.08 mm, roughly less than one EPID pixel. The *x*-axis offsets were also generally consistent and reproducible for all three linacs. The data generally followed a sinusoidal shape with gantry angle and was fitted with a sine function (black line in Fig. 3.5) for simplicity which had the form:

$$-0.15 \cdot sin(3 \cdot \theta_g + 50°) \quad [3.4]$$

Both the *y* and *x*-axis EPID sag were reproducible over a six month period for linac 3. There was some negligible deviation in the EPIDs *x*-axis sag of roughly 0.1 mm after 6 months.

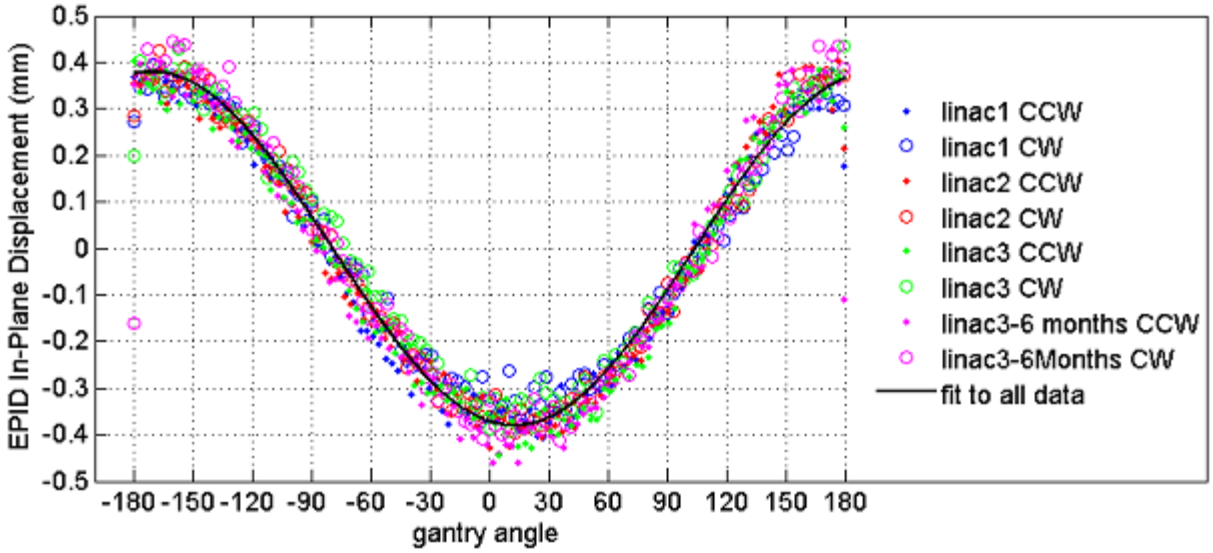

Fig.3.4 [EPID *y*-axis Sag]: The EPID's *y*-axis ball-bearing positions from isocentre as a function of linac gantry angle for CW and CCW arcs delivered to three linacs at CCMB: linac 1 (blue), linac 2 (red), linac 3 (green) and linac 3 measured 6 months later (magenta). The maximum offset due to EPID sag is roughly 0.8 mm for all linacs and is independent of rotation direction. A cosine function fit to all the data is shown as a black solid line.

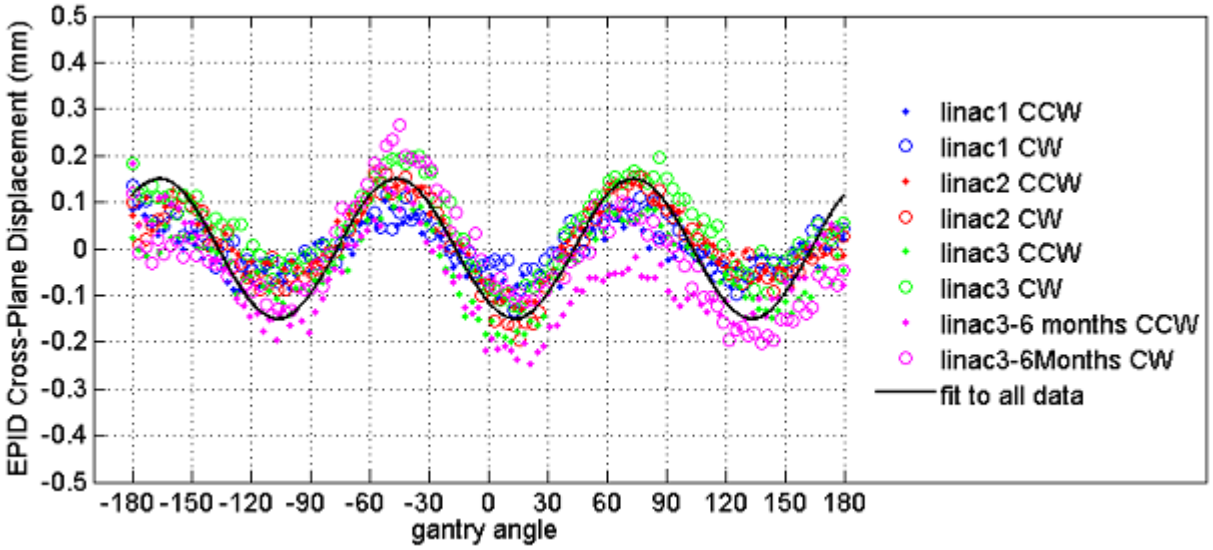

Fig.3.5 [EPID *x*-axis Sag]: The EPID's *x*-axis ball-bearing positions from isocentre as a function of linac gantry angle for CW and CCW arcs delivered to three linacs at CCMB: linac 1 (blue), linac 2 (red), linac 3 (green), and linac 3 measured 6 months later (magenta). The maximum offset due to EPID sag is roughly 0.3 mm for all linacs and is independent of rotation direction. A sine function fit to all the data is shown as a black solid line.

Both Eq. 3.3 and 3.4 provide EPID sag corrections for every EPID pixel. However, because the resolution of the EPID is only 0.39 mm per pixel (400 mm/1024 pixels) the *x*-axis correction was considered negligible. Therefore, a *y*-axis correction, Y_{corr}, to the measured EPID position, Y_{meas}, was incorporated using Eq. 3.3:

$$Y_{corr} = Y_{meas} - 0.38 \cdot cos(0.98 \cdot \theta_g - 12°) \quad [3.5]$$

This equation was applied to every measured EPID image used in our reconstruction algorithm.

The results determined here were also found in a collaborative study between CCMB and CMNH[10]. In this study, four additional Varian Trilogy linacs, located at CMNH, were included along with the three described here. A different measurement and analysis approach was performed in order to determine EPID sag and yielded identical results to the ones described here. This was a good validation of the analysis performed here and also verified the reproducibility of the results for a larger sample of linacs. Measurements on one of the CMNH linacs, taken over roughly a one year period, also demonstrated there were no differences in *x* or *y*-axis sag.

The study also showed that a reconstructed 3D dose of a simplistic circular collimator field using sag corrected EPID images gave an improvement in γ-pass rates up to 9% when compared to using the uncorrected images. Both image reconstructions were compared to a reference dose image taken at gantry = 0°.

The sinusoidal functions fit to the *y*-axis and *x*-axis sag data were optimized by minimizing the difference between data points for each arc and the fitted curve. A simple sine function was used to model the *x*-axis sag but the data shows that this effect may be more complex. However, due to the negligible displacement observed in the EPIDs *x*-axis direction, further curve fitting was not performed. Furthermore, there was no accurate way to quantify, if any, first order gravitational effects in the linac's *z*-axis direction. Alternatively, in an attempt to precisely align the ball-bearing to linac isocentre, days after a linac vault laser calibration, and without correcting for any *z*-axis isocentre offset (i.e., no first harmonic removal by Fourier analysis) the maximum ball-bearing displacement in the EPID's *x*-axis was determined to be roughly 0.8 mm. Therefore, it can be inferred that by including first order terms in the Fourier analysis, the EPIDs *x*-axis sag should be < 1 mm.

3.4 CONCLUSION

A characterization of the linac`s EPID sag due to gravity for three linacs at CCMB and four at CMNH was performed. The sag was reproducible and is thus a correctable effect. *Y*-axis and *x*-axis isocentre positions were consistent for all 7 linacs as well. The total *x*-axis sag effect, although hard to accurately quantify, was very small and therefore was neglected. The *y*-axis correction has been incorporated into our dose reconstruction algorithm in order to reduce the positional error per EPID image. This will allow for a more accurate patient dose reconstruction.

REFERENCES

1. Greer, P.B., and Popescu, C.C., *Dosimetric properties of an amorphous silicon electronic portal imaging device for verification of dynamic intensity modulated radiation therapy*, Med Phys, 2003, **30**, p.1618-27.
2. McCurdy B.M., and Greer, P.B., *Dosimetric properties of an amorphous-silicon EPID used in continuous acquisition mode for application to dynamic and arc IMRT*, Med Phys, 2009, **36**(7), p.3028-39.
3. van Elmpt, W.J.C., McDermott, L.N., Nijsten, S., Wendling, P., Lambin, B., and Mijnheer, B.J., *A literature review of electronic portal imaging for radiotherapy dosimetry*, Radiother Oncol, 2008, **88**, p.289-309.
4. McCurdy, B.M., and Pistorius, S., *Photon scatter in portal images: accuracy of a fluence based pencil beam superposition algorithm*, Med Phys, 2000, **27**(5), p.913-22.
5. McCurdy, B.M., and Pistorius, S., *A two-step algorithm for predicting portal dose images in arbitrary detectors*, Med Phys, 2000, **27**(9). p. 2109-16.
6. McCurdy, B.M., Luchka, K., and Pistorius, S., *Dosimetric investigation and portal dose image prediction using an amorphous silicon electronic portal imaging device*, Med Phys, 2001, **28**(6), p. 911-24.
7. Chytyk, K., and McCurdy B.M., *Investigation of tilted dose kernels for portal dose prediction in a-Si electronic portal imagers*, Med Phys, 2006, **33**(9), p. 3333-9.
8. Chytyk, K., and McCurdy, B.M., *Comprehensive fluence model for absolute portal dose image prediction*, Med Phys, 2009, **36**(4), p.1389-98.
9. Chytyk-Praznik, K., VanUytven, E., vanBeek, T.A, Greer, P.B., and McCurdy, B.M., *Model-based prediction of portal dose images during patient treatment*, Med Phys, 2013, **40**(3), p.031713.
10. Rowshanfarzad, P., Sabet, M., O'Connor, D.J., McCowan, P.M., McCurdy, B.M., and Greer, P.B., *Detection and correction for EPID and gantry sag during arc delivery using cine EPID imaging*, Med Phys, 2012, **39**(2), p.623-35.

CHAPTER FOUR: AN INVESTIGATION OF GANTRY ANGLE DATA ACCURACY FOR CINE-MODE EPID IMAGES ACQUIRED DURING VMAT

This chapter is an in-depth investigation of the gantry angle accuracy of cine-mode EPID images acquired during VMAT delivery. A verification of the linac's angle potentiometer accuracy was performed using an encoder and an in-house made radiographic gantry-angle phantom. Optional adjustments one can make in order to adjust the EPID image angle to within ±1° of the true mechanical gantry angle are also presented. Overall, the simplest method of angle adjustment for ±1° accuracy was utilizing a smoothing function of the EPID image header angle data. This chapter was previously published in the peer-reviewed Journal of Applied Clinical Medical Physics[†].

4.1 INTRODUCTION

Radiation treatment is commonly performed with a linear accelerator (linac) equipped with an electronic portal imaging device (EPID). Although the EPID was originally developed to verify patient position via anatomical imaging using the treatment x-ray beam, it also has properties attractive for use as a dosimetric verification tool[1,2]. Its integration with the radiation treatment unit, high spatial resolution, and digital output have made it the

†-P.M. McCowan, D. Rickey, P. Rowshanfarzad, P.B. Greer, W. Ansbacher, and B.M.C. McCurdy, *Investigation of gantry angle data accuracy for cine-mode EPID images acquired during arc-IMRT*, J. App. Clin. Med. Phys., 2014, **15**(1), p.187-201.

subject of many dosimetric studies[3]. These dosimetric properties along with its acquisition speed have also made the EPID a promising tool for 2D and 3D dose verifications of intensity modulated radiation therapy (IMRT) treatments[1,4]. This would be particularly useful during RapidArc™ (Varian Medical Systems, Palo Alto, CA, USA) or VMAT (Elekta AB, Stockholm, Sweden) treatments, a type of arc IMRT that involves the simultaneous control of dose rate, gantry speed, and aperture shaping while the treatment gantry rotates about the patient (VMAT also includes collimator control). For clarity, we will use the term VMAT to also define RapidArc. While the EPID has been shown to function as a good dosimeter, it has primarily been studied for dosimetric applications when acquiring images in integration mode, which produces a single image consisting of a summation of all frames captured during an irradiation. This is appropriate for static-beam IMRT delivery. However, in order to utilize the EPID as a dosimetric tool that captures the time-dependent nature of VMAT treatments, it must acquire images in cine mode (also known as continuous mode), where sequential images are produced from averaged frames acquired at a user-defined frequency.

Analysis of EPID images as a function of gantry angle (or time) is necessary in order to reconstruct the three-dimensional *in vivo* dose delivered to the patient. However, the actual gantry angle of the linac as a function of time (or EPID image) is not readily available during a VMAT treatment. In some cases the linac gantry angle indicators can also be incorrect due to inadequate QA[5] or inherent design limitations. Uncertainty in the projection angles limits the achievable accuracy of the patient dose reconstruction.

Varian's Trilogy and Clinac 2100ix linac models use an analogue potentiometer to measure the linac's physical gantry angle, while the newer TrueBeam linacs use a digital encoder. The EPID image header angles of a Clinac 2100ix/Trilogy linac are updated approximately every 1 to 3 seconds, in random time increments, due to an analogue-to-digital conversion and non-real-time communication software. TrueBeam systems update the image header information (including gantry angle) every 10 ms (although the accuracy of this needs to be tested). In principle, the linac potentiometer (or encoder for TrueBeam) is the most accurate reference to the true mechanical gantry angle, but this signal is not easily accessible during treatment.

For Varian Clinac 2300ix/Trilogy linacs, the gantry angle recorded in the DICOM[6] image header of each EPID image were found to differ by as much as three degrees from the linac's gantry potentiometer[7] while other studies have found similar results[4]. This problem was also observed by Mans et al.[8] for Elekta linacs, where a ball-bearing phantom was used to determine a 0.4 second systematic time lag in gantry angle information supplied by the software (corresponding to a nearly three degree lag at maximum gantry velocity), although it is not clear in that work if there was any additional random component, nor how reproducible the observation was. In general, the large uncertainty in EPID image header gantry data is unfortunate since it is the source most readily accessible by clinical users. There is a need for an accurate real-time estimate of gantry angle for dosimetric applications such as three dimensional dose reconstruction[8,9] and also for EPID-based, pre-treatment QA applications. This is illustrated by the recent presentation of a technique which used an experimental approach to directly measure the gantry angle with a customized radiographic

phantom during pre-treatment delivery[10]. This required modification of the treatment plan to enable imaging of the phantom during the delivery.

The purpose of this investigation is to measure the true gantry angle as a function of treatment time for Clinac 2100ix/Trilogy linacs (note that access to TrueBeam linacs is currently unavailable at our centre). In addition, methods were developed that one could apply to the gantry angles recorded in the header of EPID images, acquired in clinical mode, in order to correct them to within the clinically accepted tolerance criteria of ± 1°[11,12]. While applied to Varian linacs here, the methods described in this study can be applied to any linac equipped with an EPID.

4.2 MATERIALS AND METHODS

4.2.1. Experimental setup

To fully characterize each linac, gantry angle data was measured simultaneously with three independent methods that were synchronized with each other. For this work, three different Varian Clinac 2100ix linacs (Varian Medical Systems, Palo Alto, CA; these systems form the basis of Trilogy linacs, so the results are valid for the newer Clinac and Trilogy models) all equipped with EPID's (model aS1000) attached via a mechanical support arm (Exact E-arm) were used. An overview of the acquisition is shown schematically in Fig. 4.1 and 4.2.

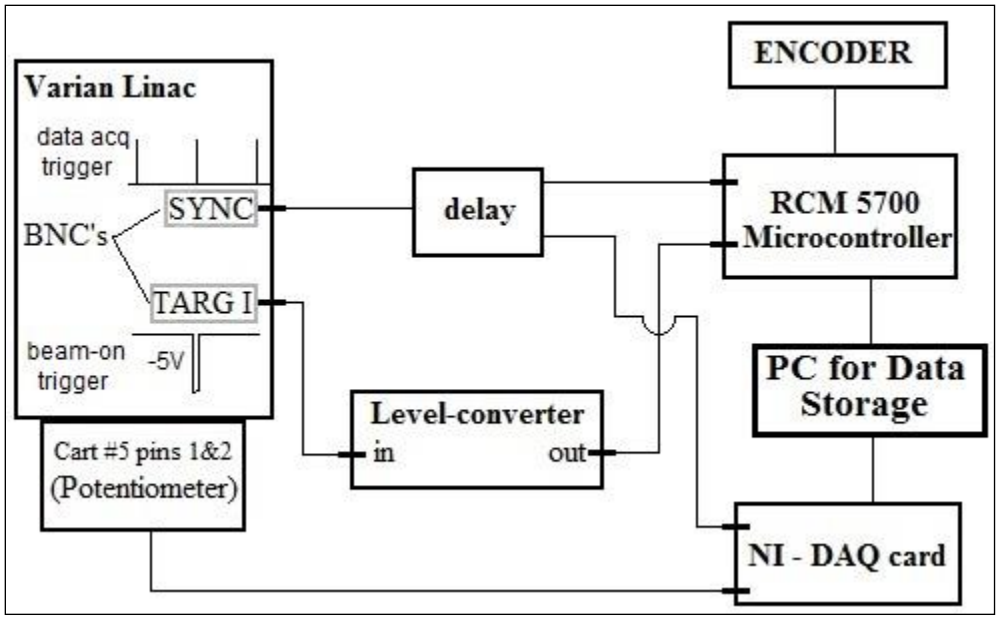

Fig. 4.1 [Signal Acquisition]: Schematic illustrating how the encoder and potentiometer data were acquired with respect to the clock signal, "SYNC" and the target current signal, "TARG I". To convert the target current signal to logic levels and stretch it to a useful length, a level converter was used. This signal allowed us to know when the beam was on or off.

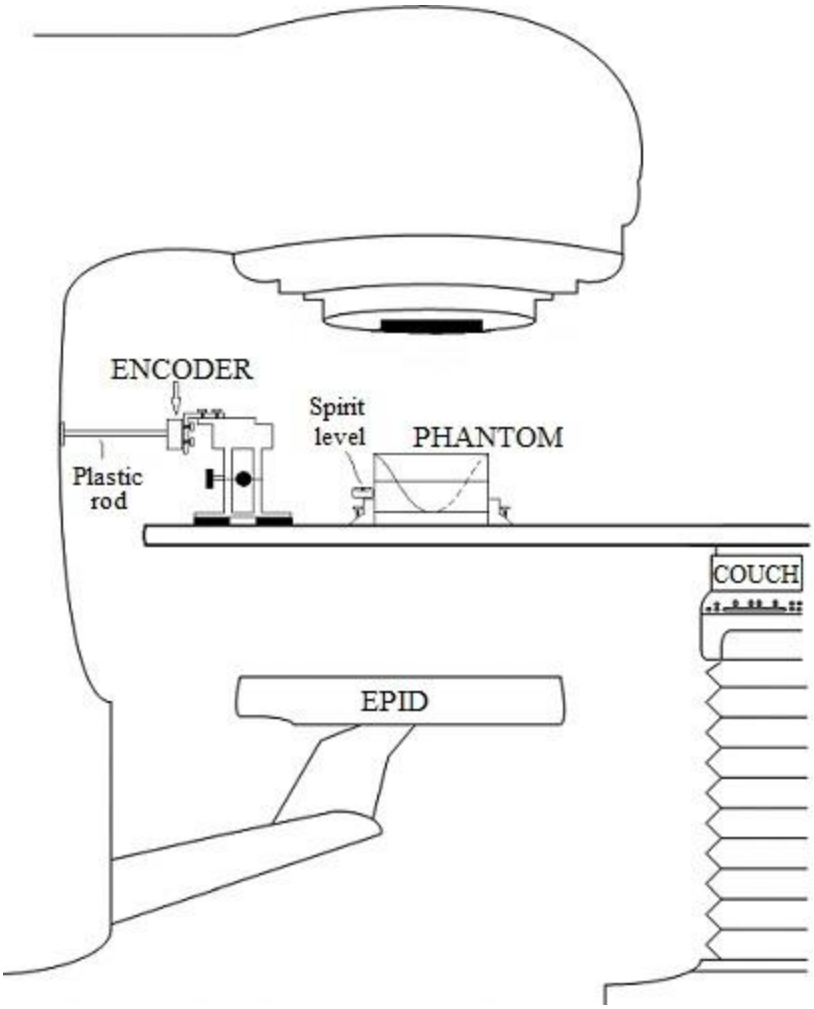

Fig. 4.2 [Experimental Setup at the Linac]: The experimental setup at the linac. An encoder was connected to the centre-of-rotation of the gantry with a plastic rod. The encoder mount allowed for precise lateral and longitudinal adjustments. Target crosshairs machined into the sides and top of our radiographic gantry-angle phantom allowed positioning at isocentre via room lasers. A spirit-level attached to the phantom base along with adjustable screws located on each of the four support legs enabled levelling.

Each linac provided a convenient clock signal, "SYNC", which was used to synchronize the rate at which measurements were acquired. Because this signal ran continuously with a frequency determined by the selected dose rate, the target current, "TARG I", signal was also acquired. The TARG I signal represents the beam pulses produced by the linac. This allowed

us to synchronize all acquired data to the same initial point ('beam-on'). Gantry angle information was then obtained by the following three methods:

i) The gantry angle was determined from EPID images of an in-house constructed gantry-angle phantom (Fig. 4.3). It consisted of a 0.80 mm diameter tungsten wire wrapped helically around a hollow acrylic cylinder with an additional straight tungsten wire traversing the central axis of the cylinder. The cylinder had a 16.0 cm outer diameter, an inner diameter of 12.8 cm, and a length of 20.0 cm. The phantom was positioned at isocentre by aligning cross-hairs etched in the top and sides of its cylindrical frame with the room lasers. A spirit level attached to the base allowed for levelling via adjustable screws in each leg. EPID images of the phantom yielded unique intersection points of the two wires as a function of gantry angle as illustrated in Fig. 4.4. The wire intersection points were determined offline using an algorithm programmed in MATLAB (MathWorks Inc., Natick, MA).

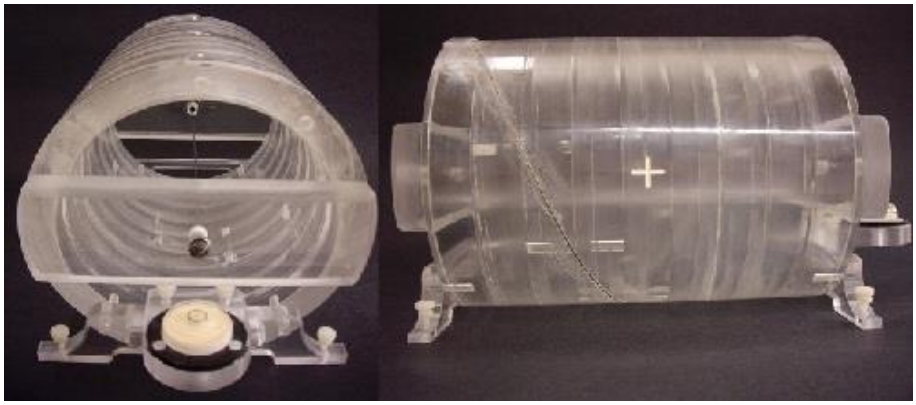

Fig. 4.3 [Gantry-Angle Phantom]: An axial (left) and lateral (right) view of our in-house constructed radiographic gantry- phantom. The axial and helical wires are visible, the latter of which was set into grooves precisely machined into the outer frame of the phantom. White levelling screws, a spirit level, and isocentre laser alignment crosshairs are also visible. The hollow cylinder and base were made of acrylic.

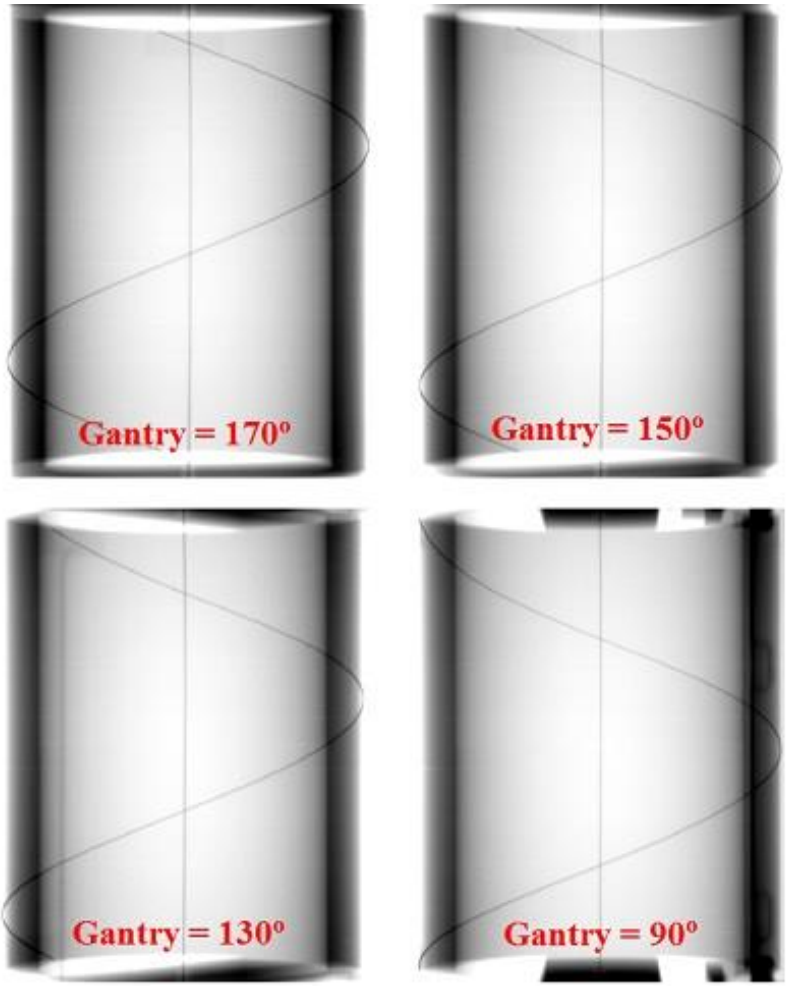

Fig. 4.4 [Gantry-Angle Phantom Transmission Images]: Four inverted grayscale EPID images of the gantry-angle phantom acquired at gantry angles 170°, 150°, 130°, and 90° (in the International Electrotechnical Commission or IEC standard). These images illustrate how the intersection points uniquely depend on the gantry angle. The axial (vertical line) and helical (casting a sinusoidal shadow when imaged) tungsten wires are observed.

ii) The potentiometer voltage that provided the gantry angle signal to the treatment unit was measured. This was performed by measuring the corresponding analogue signal, directly from the appropriate circuit board at the console area. The target current signal ("TARG I") was also simultaneously recorded. These data were acquired to a precision of 16 bits at a rate of SYNC/2 using an analogue-to-digital converter board (PCI-MIO-

16XE-50 and LabView, National Instruments, Austin, TX). Acquisition commenced before beam-on and ended after beam-off. A gantry angle-to-voltage conversion factor was calculated by averaging the first 20 data points and last 20 data points, which resulted in a range of 17.795 ± 0.007 V for a 359.8° rotation.

iii) The mechanical gantry angle was also physically measured using an optical incremental rotary encoder (SM23-2500-50/5, DATA TECH, Billerica, MA) adhered to the centre-of-rotation of the linac gantry as illustrated in Fig. 4.2. The encoder had a resolution of 10,000 ± 1 counts per revolution and data were acquired at a rate of SYNC/6 using a microcontroller (MiniCore RCM5700, Digi International, Minnetonka, MN) outfitted with an additional 2 MB of storage. The microcontroller also acquired the target current signal ("TARG I"), thus enabling encoder measurements to be synchronised to the measurements of potentiometer voltage.

The above three measurement-based methods were then compared to the angles recorded in the treatment console multi-leaf collimator (MLC) DynaLog file and the angles in the EPID image headers, both of which were created during treatment delivery. The MLC DynaLog file from a Clinac 2100ix/Trilogy linac records the gantry angle and MLC positions every 50 ms[13], while the EPID image acquisition details are discussed in Section *4.2.4*. The goal was to determine any errors these data exhibited with respect to the true gantry angle.

4.2.2. Gantry-Angle Phantom

4.2.2.i Intersection detection algorithm

Fig. 4.4 illustrates the movement of the wire intersection points for several projection images of the gantry-angle phantom. Only the wire intersection at the top of the Fig. 4.4 image was evaluated since for a full arc these points remained in the image field of view the whole time, unlike the other intersection point, which exited the bottom or top of the image halfway through an arc. A stepwise procedure of the algorithm used to locate the intersection points is explained below with the aid of Fig. 4.5. In most cases these intersections were also confirmed manually.

(a) The intersection point was found by creating a 25x25 pixel region-of-interest (ROI) around its expected location (user input was required for the first point only). The algorithm also required the number of frames averaged and the direction of rotation. From these, boundary conditions for the approximate location of subsequent intersection points were calculated and used for more accurate analysis as described below.

(b) The ROI was centred on the estimated coordinates of the new intersection point determined from the previous step. Unfortunately acquisition of EPID images in cine-mode produces banding artefacts, resulting from a lack of synchronization between the irradiation pulses and detector readout[14,15,16]. These are observed in Fig. 4.5 and were present, with differing severity, in our images. The ROI was processed to remove any banding artefacts. These were identified in the algorithm by averaging each row's first five pixel values (green box on image I in Fig. 4.5) and looking for differences between

adjacent row averages that were larger than ± 15 greyscales, a threshold manually determined by trial and error. When average row differences were larger than the threshold, the average row value was added to the remaining rows of pixels above or below that row. Values for background noise were determined by identifying the maximum pixel value from four rows of five pixel values, located at each corner of the ROI, and subtracted from image II (blue boxes in Fig. 4.5).

(c) A two dimensional convolution was performed between the ROI image and a reference image representing a perfect projection of the wire intersection at the expected gantry angle. The convolution produced an image where the greatest pixel intensity was at located at the wire intersection point.

(d) A 5x5 pixel ROI was then centered on the maximum intensity pixel of the convolution result. A centre-of-mass calculation for pixel intensity of the 5x5 ROI was performed to give sub-pixel accuracy in the X and Y directions.

(e) Due to the constant image acquisition frequency, rotation direction constraints were added in order to reduce incorrect detections of the intersection-points. It was observed that consecutive EPID images (with 3-frame averaging) resulted in Y-axis intersection points that differed from their previous location by no more than 5 pixels. Consecutive intersection points along the Y-axis should increase for counter-clockwise rotations and decrease for clockwise rotations. Consequently, any point outside these limits was

deemed invalid, rejected, and the algorithm cycled using the next maximum intensity pixel of the convolution result until a point within the limits was found.

(f) Each intersection coordinate was converted to a gantry angle using a scale factor determined from the initial and final coordinates of the gantry-angle phantom's intersections at the start and end angles of the arc.

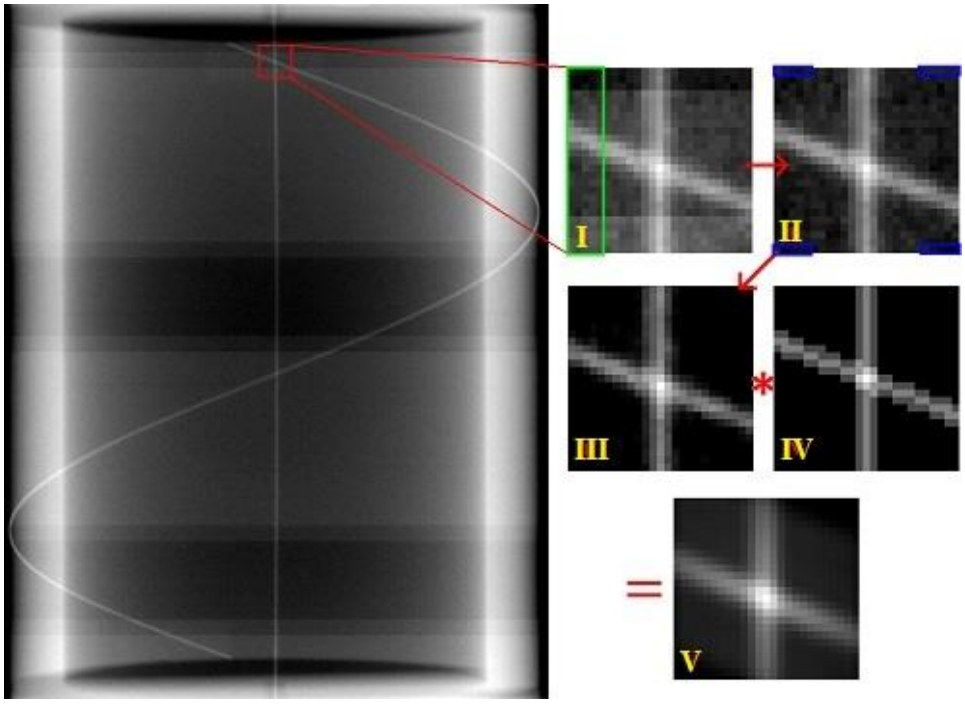

Fig. 4.5 [<u>Intersection Detection Algorithm Steps</u>]: An illustration of the wire intersection detection algorithm. The original image, which may contain banding artefacts, was cropped to a 25x25 pixel region of interest (I). Banding artefacts were removed by looking for adjacent row average differences, located within the green rectangle of image I, larger than a given threshold value. A background noise reduction was applied to the ROI by subtracting the maximum pixel value of the blue boxes from image II. A 2D convolution of image III with a reference image (IV) was calculated to produce a final image (V). A centroid calculation was performed on a 5x5 pixel square centered on the maximum intensity pixel in image V to determine the intersection coordinate.

As discussed in Chapter 3 there is a measureable sag of the EPID imager and support arm due to the effects of gravity, which is reproducible and can be quantified as a function of gantry angle[7,17]. The intersection points of the gantry-angle phantom depend only on the in-plane axis of the EPID (the axis parallel to the gantry's axis of rotation), therefore there was no need to perform an cross-plane correction. As discussed in Chapter 3, the amplitude of the resulting in-plane shift of the EPID was roughly one pixel (~0.39 mm), and has the form:

$$Y_{corr} = Y_{meas} + 0.38 \cdot cos(0.98 \cdot \theta_g - 12°) \qquad [4.1]$$

where θ_g is the linac's gantry angle (equal to the EPID angle minus 180°), Y_{meas} is the Y-axis intersection point determined from the algorithm, and Y_{corr} is the EPID sag corrected intersection point. This correction was incorporated into the analysis.

4.2.2.ii Algorithm accuracy

The intersection point detection algorithm was independently verified by acquiring EPID images of the phantom at fixed (i.e., static) gantry angles. The resulting gantry angles calculated by the algorithm were compared to the gantry angles displayed on the treatment console computer and to the gantry angles calculated from manually determined intersection points. The images were acquired at 10 degree intervals over a 360 degree arc. In addition, the accuracy of the cardinal angles (0°, 90°, 180°, and 270°) were independently validated with a high precision, four-sided gantry level (F#352-200, Radiation Products Design, Albertville, MN) accurate to 1/40 of a degree.

4.2.2.iii Phantom irradiation

For data acquisition, 6 MV beams delivering 700 MU at 600 MU/min were used to capture continuous (cine) EPID images. To determine the initial and final intersection points for the gantry-angle phantom, two additional images were acquired with 100MU at 600 MU/min for fixed gantry angles (179.9° and 180.1°) before and after delivering the treatment arc. The EPID was positioned at 140 cm source-to-detector distance (SDD). Frames were acquired at high resolution (1024x768 pixels or 0.39 mm/pixel), which was necessary to accurately determine the gantry-angle phantom's intersection points. The 'BeamOnDelay' parameter of Varian's Image Acquisition System v.3 software was set to zero.

A RapidArc^{TM} plan was constructed specifically for this study using the Eclipse software package. It consisted of a 359.8° arc with fixed jaws and MLC's producing a 21.5 cm (Y-axis) by 26.0 cm (X-axis) field at isocentre (100 cm SAD) in order to image the entire gantry-angle phantom. Using three linacs there were a total of 16 trials (arcs) delivered in treatment mode, consisting of 7 counter-clockwise and 9 clockwise rotations.

4.2.3 Time Synchronization

To allow comparison of data collected with the different methods, each set of data needed to be referenced to 'beam-on'. The target current signal, TARG I, is synchronized directly to the SYNC signal. The SYNC signal is the master timing signal for the linac's electronic control system. For a dose rate of 600 MU/min the SYNC signal frequency will be 360 Hz (it decreases by 60 Hz for every decrease of 100 MU/min). Thus, the acquisition rates for the potentiometer and encoder data were 180 Hz and 60 Hz respectively. DynaLog files update

linac angle data at 20 Hz (for all dose rates), which was assumed to be derived from the SYNC signal. The linacs create separate DynaLog files for each arc and the file only records angle data during beam-on. The EPID frame acquisition rate was set to 7.5 Hz, which is also derived from the SYNC signal[16]. EPID images saved by the clinical computer system were three-frame averaged, i.e., acquired at 2.5 Hz. This was chosen due to a memory limitation of the On-Board Imager (OBI) computer[18], which limits the total number of high resolution images in a single treatment delivery that can be acquired, to roughly 200. This limitation of cine-mode imaging with a Varian Clinac 2100ix/Trilogy was also observed in another study[10]. Consequently, approximately 185 EPID images were produced for each 359.8° arc.

4.2.4 EPID image time uncertainty

Since data were acquired at submultiples of the SYNC signal, there were uncertainties with respect to the first TARG I pulse. The maximum uncertainty associated with each method could be as large as the acquisition period minus one SYNC period. The maximum time uncertainties for the potentiometer, encoder, and DynaLog file were neglected due to their fast acquisition rates. The slower acquisition rate of the EPID images (2.5 Hz) produced the largest time uncertainties. In order to characterize these, a separate computer with frame grabbing hardware and associated software package (iTools Capture, Varian Medical Systems) was connected directly to the frame processing board of the treatment console computer. This allowed us to capture EPID frames continuously before and during beam-on. Using the same RapidArc™ plan described in Section 4.2.2.iii, a total of 10 arcs on the same three linacs (5 counter-clockwise and 5 clockwise trials) were delivered. The EPID images saved by the clinical software were compared to the frames captured by the frame-grabber.

The goal was to determine an estimated time delay correction, t_d, to be applied to the clinically saved EPID images.

4.2.5 Correspondence of the encoder, gantry potentiometer, and gantry-angle phantom readings

In order to characterize the potentiometer, a comparison of every third angle measurement made with the potentiometer to angle measurements made with the rotary encoder was performed. The gantry-angle phantom data was also compared to a two-point interpolated potentiometer angle data set.

4.2.6 EPID header and DynaLog file angles

The EPID image header angles were compared to a two-point interpolation of the potentiometer angle data set with respect to the EPID image time. Header angles were compared to potentiometer angles three different ways: using the unmodified EPID image time, applying the determined EPID image time delay correction, t_d, and by applying a boxcar smoothing function to the time delay corrected EPID image headers. The boxcar function was utilized to smooth noise in the angle data, present due to the random 1 to 3 second update lag for the EPID headers. It convolves the header angle data with a box-shaped pulse of width (2m+1) values, where m is the number of nearest neighbours. The function had the form:

$$\theta_s = \frac{1}{2\mathrm{m}+1}\sum_{\mathrm{j}=(\mathrm{i}-\mathrm{m})}^{(\mathrm{i}+\mathrm{m})}[\theta_e(i) - \theta_e(j)] \qquad [4.2]$$

where θ_s is the smoothed result, θ_e is the EPID angle, and 'm' was chosen to be 2 (for three frame averaging this corresponds to a 1.6 second box-shaped pulse) in order to minimize errors due to the update lag.

The angle data in the DynaLog file (20 Hz) were compared to every ninth potentiometer angle (180 Hz). Mean angle differences and standard deviations were calculated.

4.2.7 Independent inclinometer measurement

A completely independent gantry angle measurement technique was performed on a Clinac 2100ix/Trilogy linac located at a different treatment facility. An inclinometer (NG360, Nordic Transducer, Handsund, Denmark) was bolted to a steel frame, which was attached to the linac head's accessory tray slot such that it could not move during gantry rotation. Potentiometer data were acquired using OMB-DaqView-XL software (Omega Engineering Inc., Stamford, CT) with a Personal Daq/56 USB analogue-to-digital data acquisition module (IOtech, Norton, MA) attached to the linac's gantry potentiometer. Six rotations were completed (without an encoder or gantry-angle phantom present) while the inclinometer acquired data at 1.0 second intervals, and the inclinometer data were compared to the interpolated potentiometer data. The manufacturer has stated that there is a 0.56 second systematic lag for this inclinometer model[19]. For each trial 360 MU at 600 MU/min were delivered over 359.8° arcs. Since inclinometers are popular choices for gantry angle QA a comparison of the inclinometer accuracy to that of our encoder and gantry-angle phantom methods was carried out.

4.2.8 Effect of angle adjustment on 3D dose reconstructions

In order to determine the overall effect of a gantry angle adjustment eight different VMAT plans were delivered to an anthropomorphic phantom and EPID images were acquired using a six frame average. Using our EPID-based *in vivo* patient dose reconstruction model[20] results using header angles and box-smoothed header angles were individually compared to the Eclipse (Varian Medical Systems, Palo Alto, CA) treatment planning result. χ-compariaon tests of the high dose volume (HDV) regions, defined as the voxels containing 80% or more of the prescribed dose (generally considered to encompass the planning target volume) were performed.

4.3 RESULTS AND DISCUSSION

4.3.1 Phantom intersection detection algorithm accuracy

Verification of the gantry-angle phantom and analysis algorithm was carried out by comparing the angles calculated from the gantry-angle phantom image analysis to angles displayed on the treatment console, in 10° intervals using static gantry angles. Using the high precision gantry level it was confirmed that the console displayed the cardinal angles to within ± 0.08°. A linear regression performed on the algorithm-determined gantry angles from the EPID images as a function of the angles displayed on the treatment console resulted in a slope of 1.000 ± 0.143. This indicated that the error in the linac's gantry angle display was random and likely larger than ± 0.08° at angles other than the cardinal angles. As well, a

linear regression of manually-determined gantry angles (i.e., intersection points) to those determined automatically by the algorithm resulted in a slope of 1.000 ± 0.016. The strong agreement in the regression analyses confirms that the algorithm was accurately determining intersection points.

The gantry-angle phantom analysis was susceptible to mechanical effects inherent to the linac's gantry and EPID support arm. These effects, which differ for each linac, may arise from wear and tear of linac components. These effects do not include gravitational effects on the EPID and EPID arm as those were corrected for in our analysis.

4.3.2 EPID image time delay correction

Comparison of the EPID images saved by the clinical systems with the frame-averaged images acquired with the frame grabber revealed that up to two frames after beam-on were tagged 'invalid' by the clinical software and thus not saved. Furthermore, the average frame acquisition time of the last invalid beam-on frame was 0.203 ± 0.004 s instead of the expected 0.133 s. This is illustrated for one trial in Fig. 4.6. There was only one case where just a single frame after beam-on was not saved. This frame had a frame acquisition time of 0.203 s and all the rows had some acquired signal. This was likely due to the beam-on trigger happening to be in sync with the EPID frame acquisition.

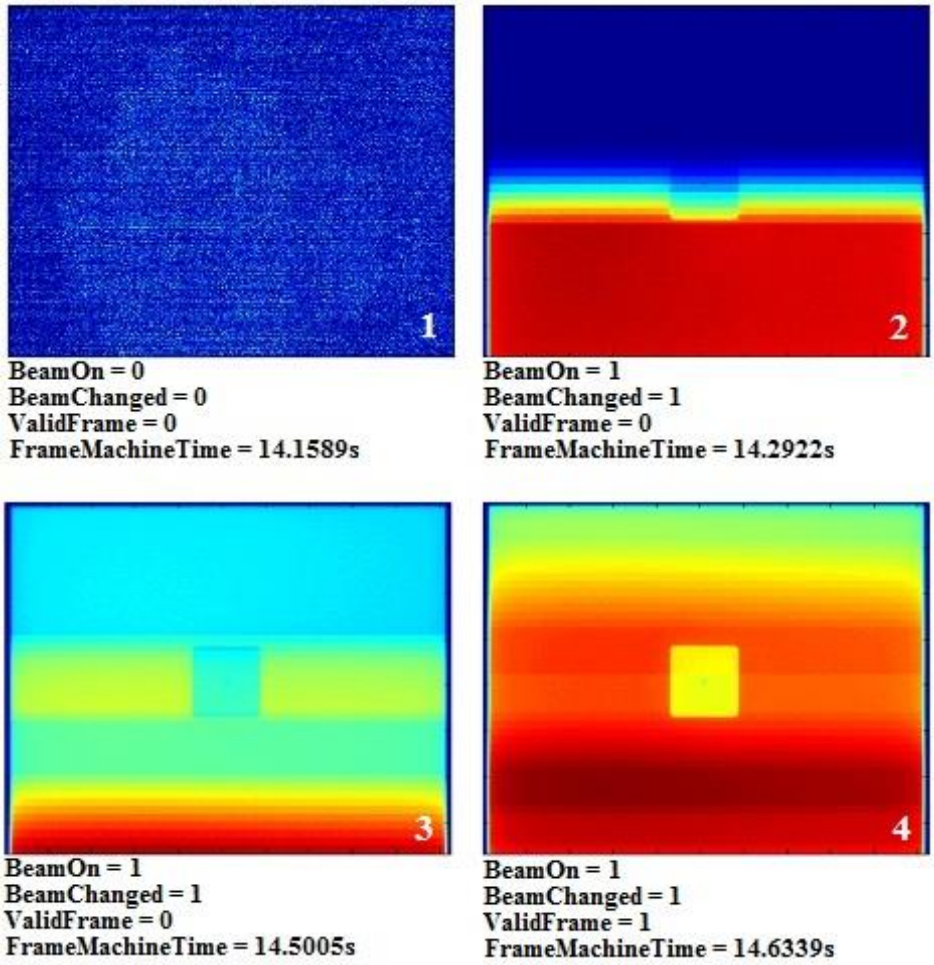

Fig. 4.6 [Lost EPID Frames After Beam-On]: EPID frames and header information of a simple cube phantom acquired at 7.5 Hz using a frame-grabber. The jaws and MLC's were positioned to allow full EPID panel irradiation. Frames 1 and 2 were acquired with beam-on (BeamOn = 1) but were not saved to the clinical system (ValidFrame = 0). A time delay, t_d, before the first clinically saved frame (ValidFrame = 1) can be calculated from the first two non-valid beam-on frames. It is also observed that frame 3 has an acquisition time of 0.2083 s, rather than 0.1333 s.

The time when beam-on occurs for the first unsaved EPID frame is random but can be calculated simply by determining the number of rows of acquired dose and knowing the frame's acquisition time. This is possible because the Varian aS1000 EPID reads pixel data in a row-by-row fashion (both Varian and Elekta EPID acquisition details can be found in the

work of Podesta et al.[21]). It was determined that the average time delay before the first clinically saved frame for all ten trials was 0.262 ± 0.042 s.

Since a frame-grabber is not available with clinical computer systems, an estimation of this time delay was required in order to apply it to every day clinical use. Due to the aforementioned frame-grabber analysis an estimated t_d of 0.267 s (half of a frame period plus 0.200 s) was chosen for two reasons: to minimize the synchronization error between data sets due to random beam-on times, and because the probability of only a single frame loss after beam-on was extremely rare. Furthermore, since each clinically acquired EPID image was an average of three frames, the time-stamp given to each was the mid-point of the image acquisition period. Thus, the first image was given a time stamp of $T_1 = t_d + 0.200$ s = 0.467 s, and the next image was given a time stamp of $T_2 = T_1 + 0.400$ s = 0.867 s. An initial frame delay time of 0.400 s was reported in a study using an Elekta SL20i linac with three frame-averaged EPID images, but the source of the delay was not determined[8].

4.3.3 Correspondence of the encoder, gantry-angle phantom, and gantry potentiometer readings

Encoder measurements for one gantry rotation are plotted in Fig. 4.7 as a function of the corresponding potentiometer measurements. A simple point-by-point comparison showed that the encoder measurements agreed with 99.9% of the potentiometer measurements to within ± 0.40°. A linear fit resulted in a slope of 0.999 ± 0.018. Also shown are the resulting residuals found by subtracting the potentiometer measurements from the encoder measurements. The blue lines indicate the region in which 99.9% of the measurements lie

(i.e. within ± 0.40°). Similar results were found for all trials. The low frequency variations in residuals are most likely due to mechanical deformation of the gantry cover creating small offsets between the encoder rod and the gantry's central axis-of-rotation. The high frequency variation in residuals is due to the electronic noise associated with the analogue potentiometer.

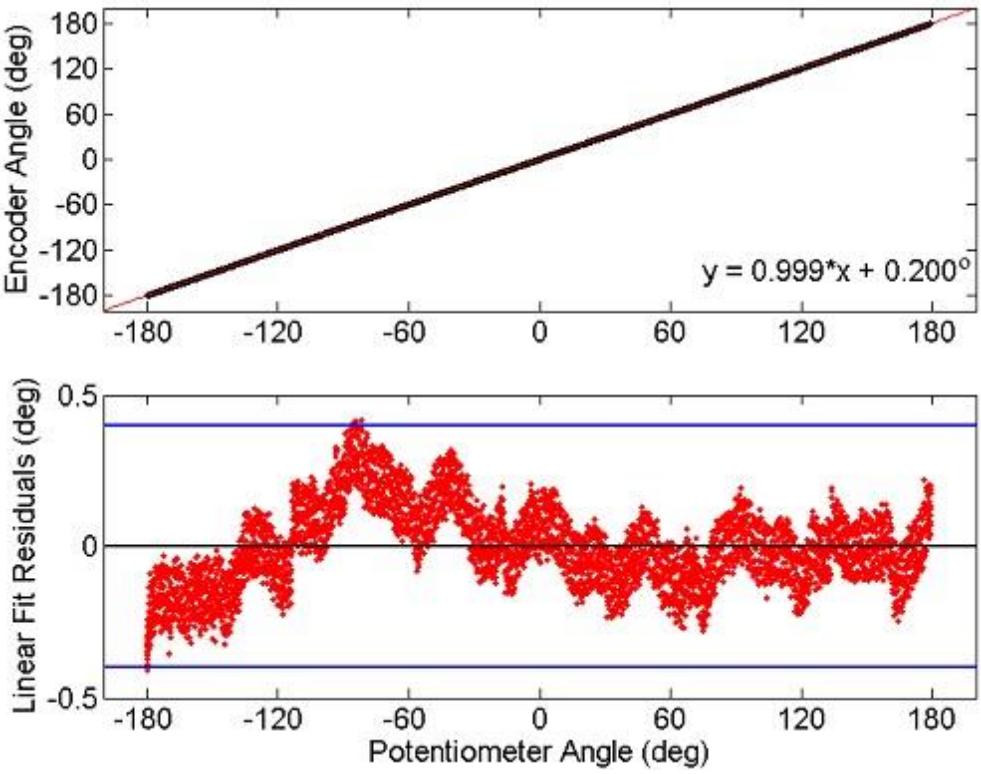

Fig. 4.7 [Potentiometer vs. Encoder]: Gantry angles measured with an optical encoder plotted as a function of the gantry angles measured by the linac's potentiometer for one trial. Both acquisition modes agreed on the gantry angle to within ± 0.4°, 99.9% of the time (between blue lines). Similar observations were found for all trials. The low frequency variation in residuals is due to slight movements of the gantry covers that could create misalignments between the encoder and the gantry's central axis of rotation. The high frequency residuals are due to electrical noise associated with the potentiometer.

The absolute mean difference and standard deviation in the gantry angle determined by the encoder and the potentiometer for each trial are given in Table 4.1. One trial for linac #2 had no encoder data acquired. The absolute mean difference in angle and standard deviation between the encoder and potentiometer data for linac #1, #2, and #3 were 0.15 ± 0.12°, 0.07 ± 0.17°, and 0.17 ± 0.12° respectively.

The absolute mean difference in angle and standard deviation between the gantry-angle phantom and potentiometer for linac #1, #2, and #3 were 0.10 ± 0.28°, 0.10 ± 0.29°, and 0.09 ± 0.31° respectively. Results of all trials for all linacs are also given in Table 4.1. Without incorporating the EPID image time delay correction, t_d, the absolute mean difference in gantry angle with the potentiometer for linac #1, #2, and #3 were 1.18° ± 0.28°, 1.20° ± 0.29°, and 1.26° ± 0.31° respectively (not given in Table 4.1). The significant improvement in angle accuracy validates the determined time delay correction value.

The high levels of agreement between these two independent measurements with the potentiometer indicate that, as expected, the linac potentiometer is accurately recording the gantry angle and that the chosen potentiometer acquisition method was reliable. For subsequent analyses the potentiometer was used as the reference for comparison.

Table 4.1. Encoder and Gantry-Angle Phantom Absolute Mean Differences in angle with the linac potentiometer.

		Encoder	Gantry-Angle Phantom
Linac	**Rotation Direction**	**Absolute Mean Angle Difference (± SD)**	**Absolute Mean Angle Difference (± SD)**
#1	CW1	0.15 ± 0.12	0.01 ± 0.30
	CW2	0.16 ± 0.13	0.12 ± 0.29
	CW3	0.30 ± 0.12	0.10 ± 0.28
	CCW1	0.13 ± 0.12	0.17 ± 0.29
	CCW2	0.01 ± 0.12	0.10 ± 0.26
#2	CW1	0.00 ± 0.17	0.04 ± 0.31
	CW2	n/a	0.07 ± 0.29
	CW3	0.05 ± 0.17	0.07 ± 0.29
	CCW1	0.14 ± 0.17	0.04 ± 0.30
	CCW2	0.04 ± 0.16	0.21 ± 0.28
	CCW3	0.11 ± 0.17	0.17 ± 0.28
#3	CW0	0.24 ± 0.11	0.10 ± 0.30
	CW1	0.15 ± 0.13	0.11 ± 0.31
	CW2	0.30 ± 0.12	0.08 ± 0.30
	CCW1	0.13 ± 0.12	0.05 ± 0.33
	CCW2	0.01 ± 0.12	0.09 ± 0.33

4.3.4 EPID image header angle corrections

The absolute mean difference and standard deviation between the uncorrected (t_d = 0) EPID header angles and potentiometer angles for all trials are given in Table 4.2. Both the mean and standard deviation were given to illustrate the statistical variation of the angle differences. It can be seen that the gantry angles recorded in the EPID image headers have large standard deviations and typically disagree with the potentiometer by more than one degree. For some trials, individual EPID header gantry angles disagreed by as much as ± 3° with the potentiometer, much larger than the tolerance criteria of ±1°.

The percentage of the EPID header gantry angle differences within ±1° of the potentiometer are also given in Table 4.2. For linacs #1, #2, and #3 the average per cent of uncorrected ($t_d = 0$) EPID header angles within ±1° of the potentiometer were 38.7%, 36.8%, and 29.3% respectively, and was as low as 21.6% for one trial. This highlights the need for a method that adjusts the gantry angles recorded in the EPID header to within an acceptable tolerance. Incorporating the suggested time delay correction, the average angle agreement within ±1° improved to 74.6%, 75.7%, and 75.3% for linacs #1, #2, and #3 respectively. For all linacs, an average of 99.4% of the boxcar smoothed, time delay corrected EPID header gantry angles agreed within ±1° of the potentiometer; the lowest agreement was 97.8% for one trial. In all trials it was either the first and/or last few images which had differences in angle larger than ±1° but they never exceeded ±1.23°. This was likely due to the convolution of the boxcar smoothing function not including enough neighbouring data points in those regions of the data.

An example of these analyses is illustrated in Fig. 4.8 for trial "CW1" of linac #3. The EPID image header gantry angle datasets shown include the uncorrected (purple diamonds), the time corrected (green circles), and the time corrected and boxcar smoothed analysis. The blue lines illustrate the defined tolerance of ± 1° agreement with the potentiometer (black line at zero). There is an observed improvement in the header gantry angle accuracy due to the incorporation of the EPID image time delay correction.

Table 4.2. Differences Between the Potentiometer and EPID Header Angles, Including Time Delays and Linear Fits.

		EPID image headers				
		Uncorrected (t_d = 0)			Time delay corrected (t_d=0.267s)	Boxcar time delay corrected
Linac	Trial	Absolute Mean Diff	St. Dev.	% within ±1°	% within ±1°	% within ±1°
#1	CW1	0.95	0.78	49.7	76.1	99.5
	CW2	1.32	0.82	40.2	76.6	99.5
	CW3	1.36	0.81	23.3	75.0	100
	CCW1	1.06	0.89	41.2	73.8	98.9
	CCW2	1.12	0.89	39.0	71.6	97.8
#2	CW1	1.10	0.74	35.6	80.6	100
	CW2	1.01	0.75	46.4	81.8	98.9
	CW3	1.18	0.73	37.0	79.2	100
	CCW1	1.35	0.84	27.9	74.9	98.9
	CCW2	1.06	0.87	43.4	73.6	99.4
	CCW3	1.46	0.90	30.2	64.3	99.4
#3	CW1	1.65	0.78	21.6	75.8	98.9
	CW2	1.18	0.79	40.3	74.3	99.5
	CW3	1.51	0.78	25.8	77.4	100
	CCW1	1.55	0.76	24.6	69.1	98.9
	CCW2	1.24	0.73	34.0	80.1	100

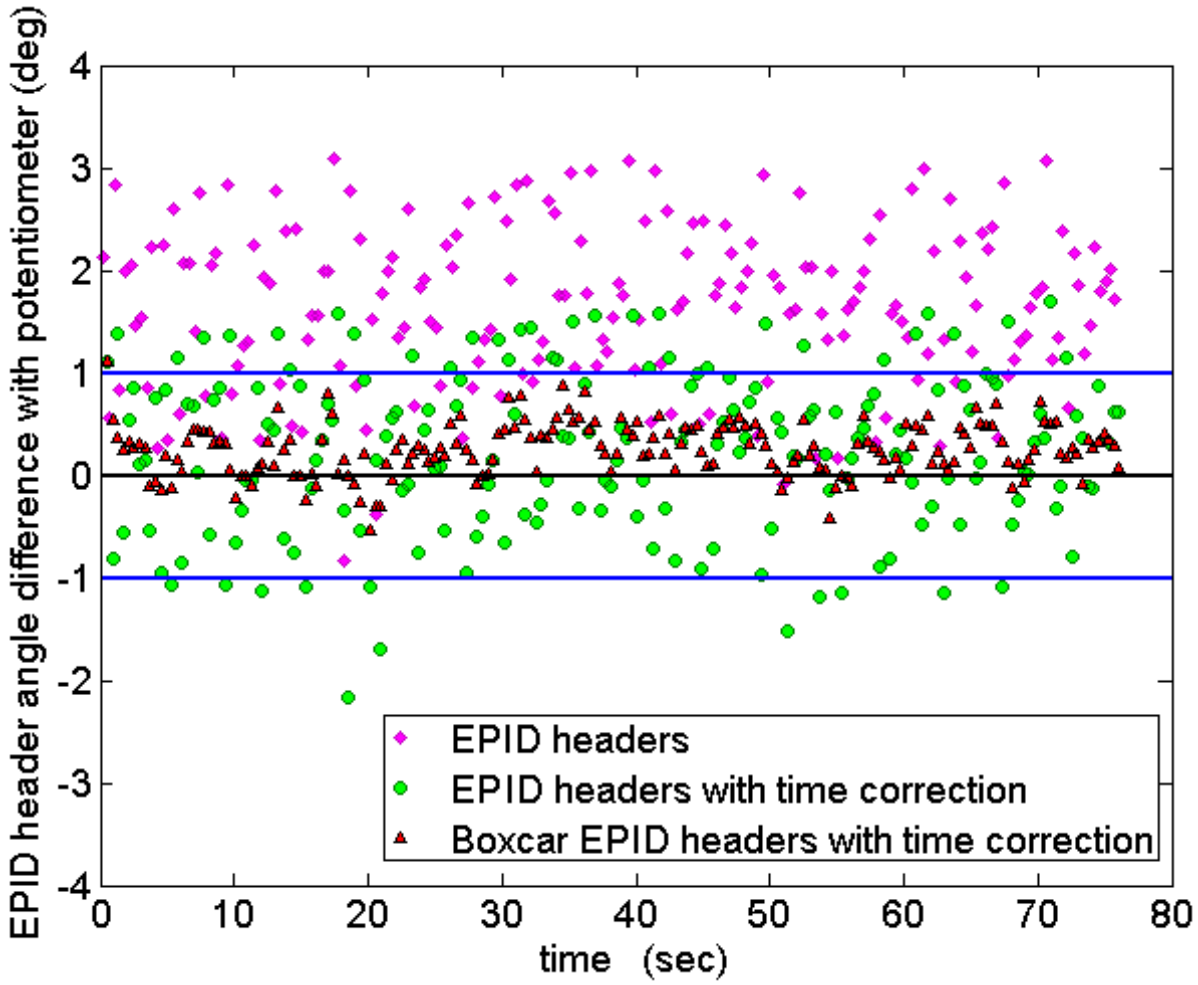

Fig. 4.8 [<u>EPID Image Header Adjustments</u>]: Graph showing differences in angle between the EPID image header data and the linac potentiometer data (black line at zero) as a function of the EPID image time for trial "CW1" from linac #3. Only 21.6% of the unmodified header angles (purple diamonds) were within ±1° (blue lines) of the potentiometer and had a maximum angle difference of 3.1°. Applying the time correction to the EPID image times (green circles), improved the ±1° angle agreement to 75.8%, while 98.9% of the boxcar smoothed, time-corrected header angles (red triangles) agreed within ±1°.

4.3.5 DynaLog file's gantry angle accuracy

The absolute mean difference between the DynaLog file gantry angle and the potentiometer gantry angle for linacs #1, #2, and #3 was 0.11° ± 0.04°, 0.12° ± 0.04°, and 0.11° ± 0.04° respectively. Importantly, 100% of the gantry angle differences were within

±1.0° of the potentiometer and the largest angle difference was 0.46° for one data set. Therefore the gantry angle data stored within the MLC DynaLog file was an accurate reference to the true gantry angle. Unfortunately accessing the DynaLog file is far less convenient than accessing the EPID image header information.

4.3.6 Inclinometer results

The angles measured with the inclinometer and the potentiometer had a mean difference of 0.33° ± 0.22° for all trials. The relatively large standard deviation was due to the measurement method of the inclinometer system, which is based on a liquid capacitive sensor that produces significant electronic noise during movement.

4.3.7 Reconstruction Results

For the eight different types of VMAT plans reconstructions were performed using the header angles as well as the box-smoothed header angles. Both results were compared to the Eclipse treatment planning result. For all plans, there were improvements in the HDV χ-pass rates ranging between up to 5.0% using a 2%/2mm criterion up to 2.0% using a 3%/3mm criterion. This noticeable improvement encourages a header gantry angle adjustment.

4.3.8 Discussion

To perform *in vivo* patient dose reconstruction for VMAT, one needs to accurately know the gantry angle associated with each EPID image. At present, the exact accuracy in EPID image gantry angle required to accurately reconstruct patient dose is unknown. However, the AAPM Task Group 142[10] and Task Group 40[9] recommended gantry angle accuracy of ± 1°

was considered to be a logical goal. During irradiation of a patient it is impractical to have an encoder or gantry-angle phantom present on the linac couch. This study presents several alternative means of reducing the EPID image gantry angle error. While the 2100ix series of linacs were characterized in this work, the methods can be applied easily to EPID images acquired with any commercial linac.

The time delay associated with clinically acquired cine-mode EPID images using Trilogy/Clinac2100ix linacs was quantitatively measured using a frame-grabber. Similar results were found for EPIDs on Elekta linacs[8]. Using the results from the frame grabber analysis an estimated time delay correction was used on the EPID images of each trial. This approach, rather than measuring a time delay correction for each trial, was used in order to make the methods proposed here clinically applicable. The suggested estimate of the time delay correction, to be applied to the time stamp of the EPID image header, noticeably increased the percentage of header gantry angle values within ± 1° of the true gantry angle.

Verification of the accuracy of the linac's potentiometer gantry angle during VMAT using an optical encoder and with an in-house constructed gantry-angle phantom was performed. The difference in angle between the potentiometer and encoder for all linacs was 0.13 ± 0.14°. A difference of 0.10 ± 0.30° was found between the potentiometer and gantry-angle phantom for all linacs. The potentiometer accuracy was also verified to within roughly a third of a degree by an inclinometer. Although the encoder and gantry-angle phantom cannot be used for gantry angle correction during regular treatment, they can alternatively be used for precise linac gantry angle QA.

It has been shown that the gantry angles recorded in the EPID image headers can differ from the potentiometer measurements by as much as ± 3°. For the trials presented here, an average of 35% of header angles agreed within ±1° of the potentiometer. However, by applying the suggested time delay correction to the EPID image time, an average of 75% of the header angles agreed within ±1° of the potentiometer for all trials. By also applying a simple boxcar smoothing to the time corrected images, an average of 99.4% of the header angles were corrected to within ± 1° of the potentiometer. Alternatively, the gantry angles recorded in the DynaLog file were shown to lie within ± 0.5° of the potentiometer data. Although the DynaLog angle data meets the desired accuracy, it is inconvenient and time consuming to retrieve the file for each treatment arc as compared to using the EPID headers.

The inclinometer model used in this study adequately characterized the linac's gantry angle during VMAT although it was less accurate than the encoder or gantry-angle phantom methods. This was mainly due to its slower acquisition rate and high level of noise.

There was an improvement in the 3D reconstructed dose when using the box-smoothed adjusted header angles as opposed to just using the unmodified header angles.

4.4 CONCLUSION

An investigation of three independent methods for accurately measuring the linac gantry angle and the development of three approaches to obtain an accurate, on-treatment EPID

image gantry angle were performed. It was shown that the gantry angle data contained in both the DynaLog files and in the EPID image headers can be analysed to ensure almost all of the EPID image gantry angles are within ± 1° of the true gantry angle. This accuracy coincides with the AAPM-recommended tolerance for gantry angle precision. Without the analyses proposed here, the EPID image header angles demonstrate an uncertainty as large as ± 3°. The methods discussed in this study are applicable to any EPID-equipped linac. This study provides a critical step towards *in vivo* patient dose reconstruction during VMAT, by ensuring the gantry angles associated with the EPID images are accurate and precise. It was also shown that the *in vivo* patient dose reconstruction accuracy will improve with better EPID angle accuracy.

REFERENCES

1. McCurdy, B.M., and Greer, P.B., *Dosimetric properties of an amorphous-silicon EPID used in continuous acquisition mode for application to dynamic and arc IMRT*, Med Phys, 2009, **36**, p.3028-3039.
2. Greer P.B., and Popescu, C.C., *Dosimetric properties of an amorphous silicon electronic portal imaging device for verification of dynamic intensity modulated radiation therapy*, Med Phys, 2003, **30**, p.1618-1627.
3. van Elmpt W., McDermott, L.N., Nijsten, S., Wendling, M., Lambin, P., and Mijnheer, B., *A literature review of electronic portal imaging for radiotherapy dosimetry*, Radiother Oncol, 2008, **88**, p.289-309.
4. Ansbacher, W., Swift, C-L., and Greer, P.B., *An evaluation of cine-mode 3D portal image dosimetry for Volumetric Modulated Arc Therapy*, J Phys: Conf Ser, 2010, 250-012022.
5. Chang, L., Ho, S., Du, Y., Lin, C., and Chen, T., *An improved method to accurately calibrate the gantry angle indicators of the radiotherapy linear accelerators*, Nuc Inst Meth Phys Res, 2007, **576**, p.441-445.
6. http://dicom.nema.org/
7. McCowan, P.M., McCurdy, B.M., Greer, P.B., Rickey, D.W., and Rowshanfarzad, P., *An Investigation of Geometry Issues for EPID Dosimetry during Rotational IMRT*, Med Phys, 2010, **37**, p. 3896.
8. Mans, A., Remeijer, P., Olaciregui-Ruiz, I., Wendling, M., Sonke, J.J., Mijnheer, B., van Herk, M., and Stroom, J.C., *3D Dosimetric verification of volumetric-modulated arc therapy by portal dosimetry*, Radiother Oncol, 2010, **94**, p.181-187.

9. VanUytven, E., McCurdy, B.M., van Beek, T., Chytyk, K., and Greer, P.B., *Accurate patient dose reconstruction from on-treatment EPID images*: Electronic Portal Imaging 2012 International Conference, Abstract.
10. Adamson, J., and Wu, Q., *Independent verification of gantry angle for pre-treatment VMAT QA using EPID*, Phys Med Biol, 2012, **57**, p.6587-6600.
11. Kutcher, G.J., Coia, L., Gillin, M., Hanson, W.F., Leibel, S., Morton, R.J., Palta, J.R., Purdy, J.A., Reinstein, L.E., Svensson, G.K., and Wingfield, L., *Comprehensive QA for radiation oncology: Report of AAPM Radiation Therapy Committee Task Group 40*, Med Phys, 1994, **21**, p.581-618.
12. Klein, E.E., Hanley, J., Bayouth, J., Yin, F., Simon, W., Dresser, S., Serago, C., Aguirre, F., Ma, L., Arjomandy, B., and Liu, C., *Quality Assurance of medical accelerators": Report of AAPM Radiation Therapy Committee Task Group 142*, Med Phys, 2009, **36**, p.4197-4212.
13. Varian Medical Systems: DynaLog File Viewer Reference Guide, P/N 100013698-05, (2011).
14. Blessing, D., Stsepankou, D., Wertz, H., Arns, A., Lohr, F., Hesser, J., and Wenz, F., *Breath-Hold Target Localization With Simultaneous Kilovoltage/Megavoltage Cone-Beam Computed Tomography and Fast Reconstruction*, Int J Rad Oncol, 2010, **78**, p.1219-1226.
15. Wertz, H., Stsepankou, D., Blessing, D., Rossi, M., Knox, C., Brown, K., Gros, U., Boda-Heggemann, J., Walter, C., Hesser, J., Lohr, F., and Wenz, F., *Fast Kilovoltage/Megavoltage Breathhold Cone-Beam CT for Image-Guided Radiotherapy of Lung Cancer*, Phys Med Biol, 2010, **55**, p.4203.
16. Varian Medical Systems: Image Acquisition System 3, Reference Guide, P/N B401994R01H, (2011).
17. Rowshanfarzad, P., Sabet, M., O'Connor, D.J., McCowan, P.M., McCurdy, B.M., and Greer, P.B., *Detection and Correction for EPID and Gantry Sag During Arc Delivery Using Cine EPID Imaging*, Med Phys, 2012, **39**, p.623-635.
18. Varian Medical Systems: On-Board imager® Advanced Imaging, Customer Release Note ver.1.5.18, (2011).
19. Rowshanfarzad, P., Sabet, M., O'Connor, D.J., McCowan, P.M., McCurdy, B.M., and Greer, P.B., *Gantry angle determination during arc-IMRT: Evaluation of a simple EPID-based technique and two commercial inclinometers*, J Appl Clin Med Phys, 2012, **13**(6), p.3981.
20. VanUytven, E., McCowan, P.M., vanBeek, T.A., Chytyk-Praznik, K., Greer, P.B., and McCurdy B.M., *Validation of a method for in vivo 3D dose reconstruction for IMRT and VMAT treatments using on-treatment EPID images and a model-based forward-calculation algorithm*, Med Phys, 2015, accepted.
21. Podesta, M., *et al.*, *Measured vs simulated portal images for low MU fields on three accelerator types: Possible consequences for 2D portal dosimetry*, Med Phys, 2012, **39**(12), p.7470-79.

CHAPTER FIVE: AN *IN VIVO* DOSE VERIFICATION METHOD FOR SBRT-VMAT DELIVERY USING THE EPID

In this chapter, the processes involved in modeling a therapeutic SBRT linac beam for the EPID-based CCMB dose reconstruction algorithm will be discussed. This was performed through Monte Carlo modeling of a Varian Trilogy linac, optimization of the fluence functions, and then a validation using six different types of SBRT-VMAT patient plans delivered to an anthropomorphic phantom. Overall, the model was determined to be clinically acceptable at predicting the in vivo dose to the patient using a 3%/3mm χ-comparison. This chapter was published in the peer-reviewed journal Medical Physics[†].

5.1 INTRODUCTION

Recently there has been increased clinical use of stereotactic body radiation therapy (SBRT) and stereotactic radiosurgery (SRS), where extremely large doses of radiation are delivered in 1-8 fractions to one or more small targets of diseased tissue. SRS traditionally was limited to the skull, due to its' rigid anatomy facilitating reproducible and accurate patient positioning, but recently with improved image guidance tools, it has[1] been applied throughout the body (named SBRT)[1]. In this work we will term all stereotactic treatments as SBRT.

[†] P.M. McCowan, E. Van Uytven, T. Van Beek and B.M.C. McCurdy, *An in vivo dose verification method for SBRT VMAT delivery using the EPID*, Med. Phys. **42**(12): 6955-6963, (2015).

Modern radiation treatment units consist of a linear accelerator (linac) and an electronic portal imaging device (EPID) that can capture images of the treatment x-ray beam exiting the patient. The EPID was originally developed to verify the patient position via anatomical imaging. However, the EPID has been shown to have properties that make it attractive to use as a dosimetric verification tool[2,3]. In this investigation, we build on our existing expertise in using EPIDs for dosimetry[3-11] to establish a system for accurate in vivo patient dose verification for volumetric modulated arc therapy (VMAT), specifically customizing our previous methods for SBRT beams. VMAT delivery involves simultaneous control and modification of dose rate, gantry speed, collimator angle, and aperture shaping, all while the treatment gantry rotates about the patient[12].

SBRT may be delivered using either VMAT or static-gantry IMRT methods, but differs from 'conventional' radiation therapy in terms of the amount of dose and number of fractions used to deliver the dose. Per fraction doses for SBRT are typically much higher (8-24 Gy/fraction vs 1.5-2.2 Gy/fraction conventionally), and delivered over fewer fractions (1-8 vs 16-40 conventionally). To reduce the time required to deliver these large doses of radiation, linear accelerators often have a customized SBRT beam mode available to deliver a higher dose rate. This option can utilize a different flattening filter (which can limit the field size) or no flattening filter, to achieve higher dose rates than standard beams (e.g. 1000-2000 cGy/minute vs 300-600 cGy/minute). The SBRT approach of delivering a few, large doses guarantees that any error made in treatment delivery has a greater radiological impact on the patient compared to the same error made during a conventional treatment regimen.

While the EPID has been shown to behave as a good dosimeter while operated in 'integration mode' it has only recently been studied using the 'continuous mode' (or 'movie mode') of acquisition. Continuous mode captures all time-dependent information delivered during VMAT treatments, needed for reconstruction of the delivered 3D patient dose. Our group was the first in the world to investigate the dosimetric properties of the EPID when operated in continuous mode. We demonstrated that, with some modification of the acquisition parameters and ensuring irradiation times were high enough, typical of VMAT treatments, the EPID still behaves as a good dosimeter in continuous mode[3]. Recent studies investigating the use of continuous mode EPID images for in vivo dosimetry by our group[11] and others[13,14] have shown that this approach is feasible.

The goal of this investigation was to build on our existing EPID dose reconstruction algorithm for conventional VMAT and IMRT[11] to develop and validate an accurate in vivo patient dose verification system for SBRT-VMAT delivery.

5.2 MATERIALS AND METHODS

5.2.1 Linac modelling

5.2.1.i linac beam dosimetry

Ionization chambers are typically used for dose distribution measurements during linac commissioning and some routine QA. However, the physical size of most ionization chambers makes them unsuitable for small field dosimetry, because of a loss of lateral

charged particle equilibrium and partial volume effect. Therefore, a stereotactic diode field detector, SFD Hi-pSi (IBA Dosimetry, Schwarzenbruck, Germany), and photon diode field detector, PFD 3G-pSi (IBA Dosimetry, Schwarzenbruck, Germany) were used for our dose profile measurements in water. The ionization volume of the SFD is 0.017 mm^3, providing better spatial resolution than standard ionization chambers. The SFD was used for profile dosimetry when field sizes were equal to or less than 8 x $8cm^2$. The PFD, which has a sensitive volume of 0.094 mm^3, was used for profile dosimetry for field sizes greater than 8 x 8 cm^2. Both detectors were unshielded for these measurements. A recent study by Dieterich and Sherouse[15] determined that the SFD diode signal over-responds for larger field sizes. Measurements provided by the manufacturer verified this effect while also showing an over-response at greater depths. These effects create slightly broader shoulders in the profile's penumbra region and slightly larger dose readings in the out-of-field profile.

Ionization chambers were used for measuring the central axis percentage depth doses (PDD) for all field sizes. Data were acquired using a Markus ionization chamber in solid water for the surface dose (single point), and a Markus chamber in liquid water for just below surface to d_{max}. The water tank was set up at 100 cm source-to-surface distance (SSD). A PTW 31016 PinPoint 3D chamber (PTW, Freiburg, Germany) was used beyond d_{max}. The Mellenberg correction[16] was applied to all Markus chamber measurements. The nominal d_{max} used in this study was 1.4cm. The accuracy of the PTW 3D chamber was verified in a study by Scott *et al*. and references within[17].

Data were acquired using a Varian Clinac 2300ix linac (Varian Medical Systems, Palo Alto, CA) delivering 1000MU/min in SBRT mode using a 6MV photon beam. Cross-plane (perpendicular to the gantry's axis of rotation) and in-plane (parallel) central axis profiles were acquired using jaw-defined square fields with side dimensions of 1, 2, 3, 5, 8, 10, 12, and 15cm at depths of 1.4, 5, 10, and 20 cm.

5.2.1.ii linac beam Monte Carlo simulation

The EGS/BEAMnrc software package[18], extensively validated for radiotherapy applications, was used to model the linac's SBRT beam. Vendor schematics for Varian's Clinac 2300ix linac beam production and modulation components, including the SBRT flattening filter, were obtained under a nondisclosure agreement. These were required in order to perform detailed Monte Carlo simulations of the radiation beam formation, collimation, and modulation. Directional bremsstrahlung splitting (DBS) was incorporated using a splitting number of 750 and splitting radii of 20 cm for all field sizes. Global photon cutoff energy and electron cutoff energy, PCUT and ECUT, were 0.01 and 0.521 MeV respectively. The number of histories was set to 5×10^8 and phase-space files were produced at 100 cm source-to-surface distance (SSD). A mono-energetic, pre-target electron beam energy of 6.13 MeV was employed, as the resulting output agreed best with the experimentally acquired PDD data. The source was a circular beam with a Gaussian distribution having FWHM values of 0.12 cm.

The phase-space files produced with BEAMnrc were then used as input for DOSXYZnrc, a Monte Carlo software package which estimates radiation dose in user-defined voxel

geometries. Dose was scored in voxels having dimensions of 0.6 mm × 0.5 mm × *z* for the out-of field region, 0.1 mm × 0.5 mm × *z* in the penumbral region, and 0.3-0.5 mm × 0.5 mm × *z* in the central region (depending on field size). The *z* dimension of the voxels was chosen to be 2 mm and was increased to 1 cm at depths below 20cm. These choices were based on the small field modeling work of Scott *et al*.[17] except for our choice of a smaller *x* dimension voxel in the penumbral region. Central axis profiles and PDD's were created for the field sizes and depths listed in section 5.2.1.i.

5.2.2 EPID-based dose reconstruction

Our in-house developed, EPID-based dose reconstruction model consists of two elements: a 'forward' prediction and an 'inverse' EPID measured component. The forward model can predict fluence and/or dose at any plane between the linac head and the EPID. The inverse model uses both on-treatment measured as well as forward model predicted EPID images in order to reflect delivery information. Both models will be summarized briefly below for clarity in the following sections. In this work, a forward model was needed to be commissioned specifically for a clinical SBRT beam.

5.2.2.i 'Forward' prediction: predicting fluence entering the EPID and converting to dose

The forward model consists of a focal fluence source (i.e., fluence originating in the target) and extra-focal fluence source (i.e., fluence generated in any non-target component). A comparison of measured and predicted EPID images was used to optimize each fluence which is described in detail by Chytyk-Praznik *et al*.[9,10]. This was required in order to optimize our Monte Carlo derived SBRT linac beam data.

For VMAT (and SBRT-VMAT) delivery, the model must take into account varying modulation of the MLCs. To calculate incident fluence maps for a VMAT arc, the forward model requires the MLC leaf positions and monitor unit (MU) weightings for each control point. Our group uses additional in-house software to provide utilities to import treatment planning system (TPS) files to determine the machine parameters required for a desired fluence (this also includes CT datasets, contoured structures, and dose distributions). For this study the TPS used was Eclipse v.10 (Varian Medical Systems, Palo Alto, CA).

Primary fluence on the EPID, due to focal and extra-focal photons, is calculated by attenuating the incident predicted linac head energy fluence, calculated at a plane above the patient/phantom, and then along the appropriate radiological path-lengths through the phantom (or patient). The phantom/patient scatter fluence entering the EPID is calculated by convolving the incident fluence (entering the patient) with Monte Carlo generated scatter energy fluence kernels. This is described in detail by McCurdy and Pistorius[4,5].

The total predicted fluence incident on the EPID is a sum of the primary fluence from the linac and scattered fluence from the patient. For each *x* and *y* position on the EPID, a convolution of the total fluence with a pre-calculated library of EPID dose deposition kernels is performed for 15 defined energy bins and summed over all the contributing energies at that position. EPID dose kernels were generated using DOSXYZnrc and is described by Chytyk-Praznik[9]. An EPID support arm backscatter dose correction[19] and optical glare signal correction[20] are also performed.

5.2.2.ii EPID image dose reconstruction: 'inverse' model

This EPID-based dose reconstruction model is described in detail by VanUytven *et al*[11] and will be discussed only briefly here. In general, the model isolates the measured focal fluence at the plane of the EPID by removing the scatter and extra-focal components derived from the forward model described previously. An adjusted focal fluence is determined by multiplying the predicted focal fluence at the EPID by the ratio of the EPID measured focal dose image and the predicted EPID focal dose image. This adjusted focal fluence, which now incorporates delivery information, is back-projected to a plane above the patient and combined with the predicted extra-focal fluence component. The resulting *new* forward fluence plane is then used to calculate TERMA in the patient density data set via standard ray-tracing techniques. The dose is calculated using an in-house developed collapsed cone convolution (CCC) algorithm[11] based on the work of Ahnesjö[21] involving a 3D superposition of TERMA with point-based Monte Carlo determined dose kernels. The process is illustrated in Figure 5.1 for clarity where 'F' is fluence, 'D' is dose, 'm' is measured, 'p' is predicted, '*f*' is focal and '*ef*' is extra-focal.

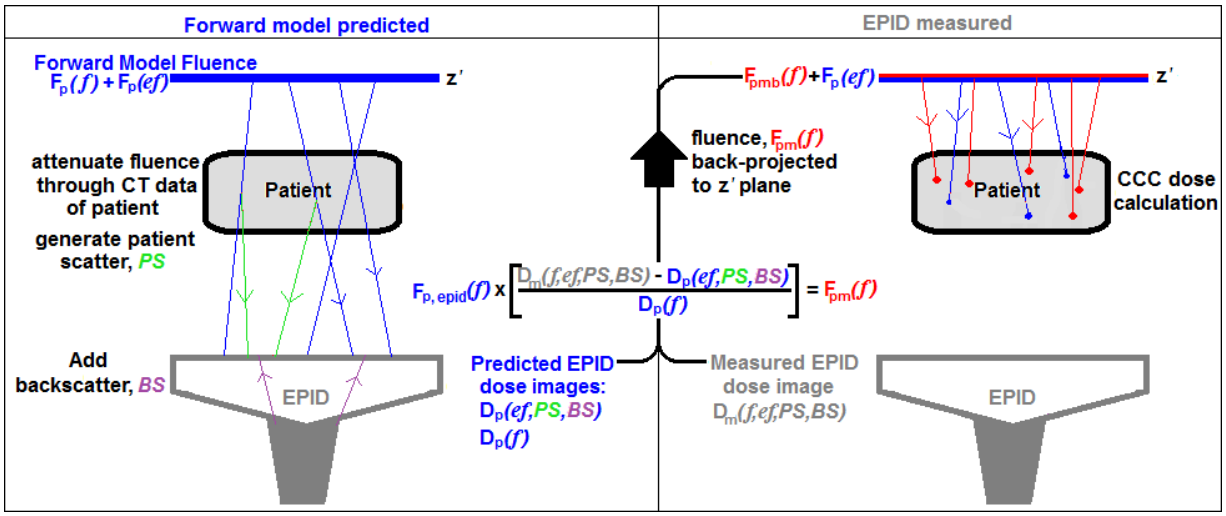

Fig. 5.1 [Inverse Model Theory]: The steps involved in our 'inverse' EPID dose reconstruction model: The forward model predicted EPID fluence, $F_{p,epid}(f)$, and dose image, D_p are compared to the measured EPID dose image, D_m (*f*-focal fluence, *ef*-extra-focal fluence). An adjusted focal fluence $F_{pm}(f)$ is back-projected to the z' plane and added to the forward model's predicted extra-focal fluence. This total fluence is projected onto the patient, used to calculate TERMA, and the delivered dose to the patient is calculated using a collapsed cone convolution calculation, i.e., a 3D superposition of TERMA with point-based dose kernels.

5.2.3 Model validation and 3D dose reconstruction

In order to validate our customized EPID dose prediction model, two prostate, three lung, and two spine SBRT-VMAT treatment plans were delivered to anthropomorphic phantoms using an energy of 6MV. The EPID was positioned at 150cm SDD for the treatments. EPID frames were acquired at 7.5 Hz using the continuous acquisition mode. Due to a virtual memory limitation of the On-Board Imager[22] computer, nine or more frames were averaged per image in order to keep the total number of images under 200; otherwise the imaging system would crash during treatment. Therefore, nine frames were averaged per EPID image for the prostate plans, the spine plans, and one lung plan while twelve frame-averaging was used for the other two lung plans and the two patient plans. Table I summarizes the treatment parameters for this study. Average gantry speed can be calculated from the imager frequency,

frame average, and number of acquired frames per arc. The model was also tested on actual patient data for one spine and lung SBRT-VMAT plan with similar acquisition details.

We compared our 3D dose reconstruction to the Eclipse AAA calculated dose using a percentage difference and χ-comparison[23] calculation. The χ-comparison is a computationally efficient version of the γ-comparison. The χ-comparison pass criteria used was a stringent 2% global dose difference (with respect to the maximum predicted dose), and a 2 mm distance-to-agreement (DTA). The percentages of pixels passing this criterion were calculated and used to quantify the comparison. The chosen criteria allowed for an in-depth analysis on the accuracy of our algorithm in comparison to Eclipse's AAA. We used it to highlight any systematic errors our algorithm may have. A more conventional 3%/3mm test was also included.

In order to maintain the time dependant information of each EPID image we need a precise gantry angle for each image. Since the gantry angles found in the image headers of the measured EPID images have been shown to be incorrect by up to ±3 degrees[24,25], they were adjusted using a method devised by our group[25]. This method uses a two-nearest neighbours sliding average function to smooth out each image header angle to improve accuracy to within ±1° of the actual gantry angle (as measured by the linac's gantry potentiometer), 99% of the time.

Table 5.1. SBRT Treatment Delivery Summary

Plan Type	Dose per fraction (Gy)	Total arc length per field	Avg. Gantry Speed (°/s)	EPID frames averaged
Prostate1	8.0	358°	3.69	9
Prostate2	8.0	358°	3.10	9
Lung1 (anterior, upper-lobe)	12.0	199°	1.48	12
Lung2 (posterior, mid-lobe)	12.0	204°	1.45	12
Lung3 (anterior, mid-lobe)	7.5	240°	3.15	9
T-spine (mid-thoracic)	6.0	358°	3.94	9
C-spine (cervical)	6.0	358°	4.26	9
Lung-posterior (patient data)	12.0	194°	1.37	12
Spine low-thoracic (patient data)	12.0	358°	2.51	12

5.3 RESULTS AND DISCUSSIONS

5.3.1 Validation of Monte Carlo modeling

The Monte Carlo simulation of the linac's SBRT beam was validated with dose measured in a water tank. Figure 5.2 shows the normalized central axis cross-plane (x-axis) profiles in water of Monte Carlo generated data (blue) and the measured data (red) at depths of 1.4, 5, 10, and 20 cm for field sizes of 2 x 2, 5 x 5, and 10 x 10 cm^2. All data were normalized to the

central axis EPID dose at a depth of 1.4 cm. Absolute percentage differences are also given in sub plots above the profile data.

For all the field sizes (1, 2, 3, 5, 8, 10, 12, and 15 cm^2) the Monte Carlo profiles agreed within 1% of the measured profiles for all the in-field data (in-plane not shown). There was a noticeable increase in the out-of-field percentage differences, ranging from 0.45% to 1.41%, as field size increased for the SFD measured data (2 x 2 to 5 x 5 cm^2 fields in figure 2). The 10 x 10 cm^2 field, measured with the PFD detector, had reduced out-of-field differences because the PFD is less sensitive to low energy photons than the SFD. For a few data points, differences in the profile's shoulder regions (i.e. steep dose gradients) were as large as 16%, because the measured fields were shaped only using the jaws, which have a larger positional error than the MLCs[26,27]. The histogram data indicates that this was a small number of points per profile. The shallow depth (d=1.4 cm and 5 cm), in-field profiles of the 10 x 10 and 15 x 15 cm^2 fields, both measured and Monte Carlo simulated, demonstrated some subtle structure. This was also reported by Scott *et al*.[17] and is likely due to the physical shape of the flattening filter. The Monte Carlo predicted and measured PDD data (not shown) agreed within 1% of each other for all field sizes. The agreement observed between measured and Monte Carlo profiles validated our SBRT linac head model.

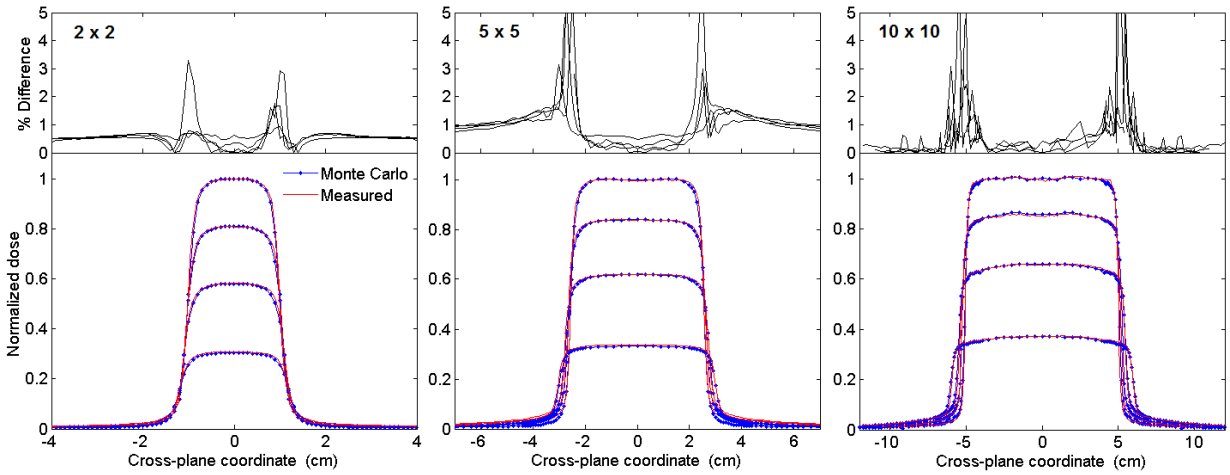

Fig. 5.2 [Monte Carlo vs Experimental Data]: The normalized central axis cross-plane dose in water profiles for 2x2, 5x5, and 10x10 cm^2 square fields at depths of 1.4, 5, 10, and 20 cm for a 6MV SBRT beam. The Monte Carlo generated data (blue dots), water tank measured data (red), and absolute percentage differences between the two (above subplot) are given. The measured and Monte Carlo profiles agreed within 1% for all in-field data and within 1.4% for the out-of-field data.

5.3.2 Linac beam model optimization output for EPID dose image prediction

Figure 5.3 shows central axis profile results of our optimization results for our predicted SBRT linac fluence as described in Section 5.2.2.i. Figure 5.3(a) shows EPID cross-plane profiles of our prediction model (blue) and the measured (red) fluence through varying water phantom thicknesses for 2 x 2 cm^2 fields. These were used to optimize the focal fluence source parameters. Figure 5.3(b) shows open field cross-plane profile comparisons. These fields, varying between 1 x 1 to 15 x 15 cm^2, were used to optimize the extra-focal source parameters. The CAX normalization values for both figures agreed within 1% for all fields. The good agreement demonstrates the robustness of our SBRT linac beam model in handling a variety of field sizes and material thicknesses. In-plane (EPID y-axis) results were similar (not shown).

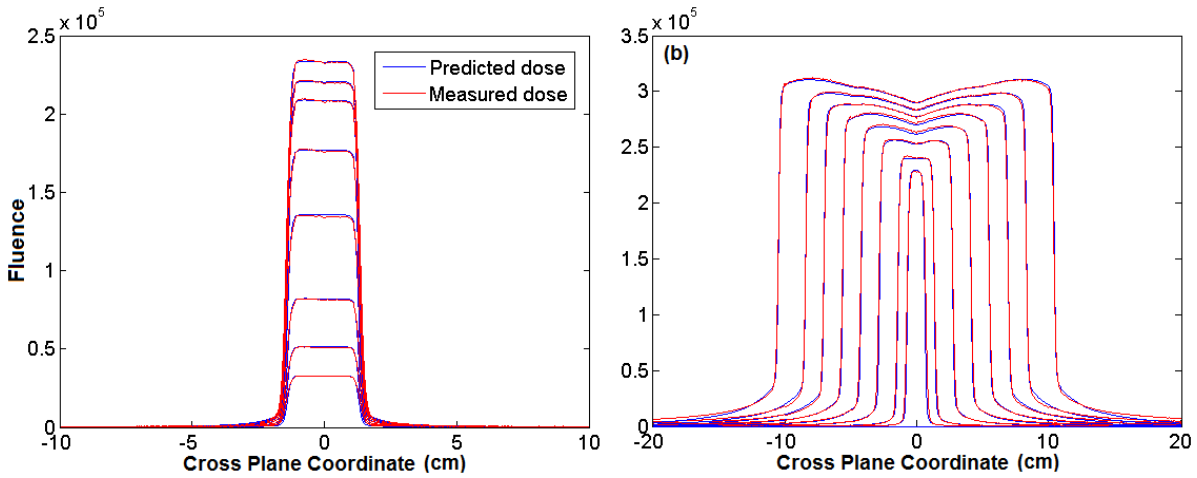

Fig. 5.3 [Model vs EPID Data]: A comparison of cross-plane profiles between EPID measured data (red) and the model predicted data (blue). Figure (a) shows the 2 x 2 cm^2 profiles through varying thicknesses of water ranging from 0 to 40 cm. Figure (b) are the 'open' square field profiles (i.e. no patient/phantom between linac and imager) used to optimize and validate the extra-focal parameters of the Pearson VII function. The range in field size was 1, 2, 3, 5, 8, 10, 12, and 15 cm per side.

5.3.3 VMAT EPID dose reconstruction

Figure 5.4 shows transverse slices of the EPID reconstructed doses overlaid on the CT data, the dose percentage difference images, and the 2%/2mm χ-comparison images between our EPID reconstruction model and the TPS calculation for the prostate2, lung3, and T-spine plans. A ±5% color bar and 0 to 1 index are given for the percentage differences and the χ-comparisons respectively. Red on the χ-comparison images indicates a failed voxel (i.e. index >1). Dose comparison data for three different volumes are given in Table II for each plan. The 'body region' defines any calculated dose in the phantom volume, 'low dose volume' (LDV) defines doses that are greater than 20% of the prescribed dose, and the 'high dose volume' (HDV) defines doses greater than 80% of the prescribed dose.

The mean percentage dose differences for the total volume of all plans were less than 3%. The 2%/2mm χ-comparison calculation gave HDV pass rates of better than 85.5% for all plans. The more commonly used 3%/3mm calculation gave better than 93.4% pass rates. For the high dose volume regions: the prostate plans had pass rates better than 91% at 2%/2mm and 98% at 3%/3mm, the lung plans had pass rates better than 88% at 2%/2mm and 95% at 3%/3mm, and the spine plans, which were the most complex, had pass rates better than 85% at 2%/2mm and 93% at 3%/3mm.

Our two patient data examples were comparable to our phantom results. The lung plan had the lowest 2%/2mm HDV pass rate of 86% while the thoracic spine plan had an HDV pass rate of 95%. At 3%/3mm all regions were better than 95%. Both phantom and patient results thus far have validated the accuracy of our EPID dose reconstruction model and we have demonstrated that using a conventional 3%/3mm criterion that this method provides clinically acceptable accuracy. Considering the AAPM TG-119 action level pass rate for IMRT of 88%[28], which can be applied to VMAT as well[29], our model performs well at 2%/2mm (lowest was 85.5%). However, the stringent criterion is more sensitive to the algorithmic differences between our model's CCC and Eclipse's AAA.

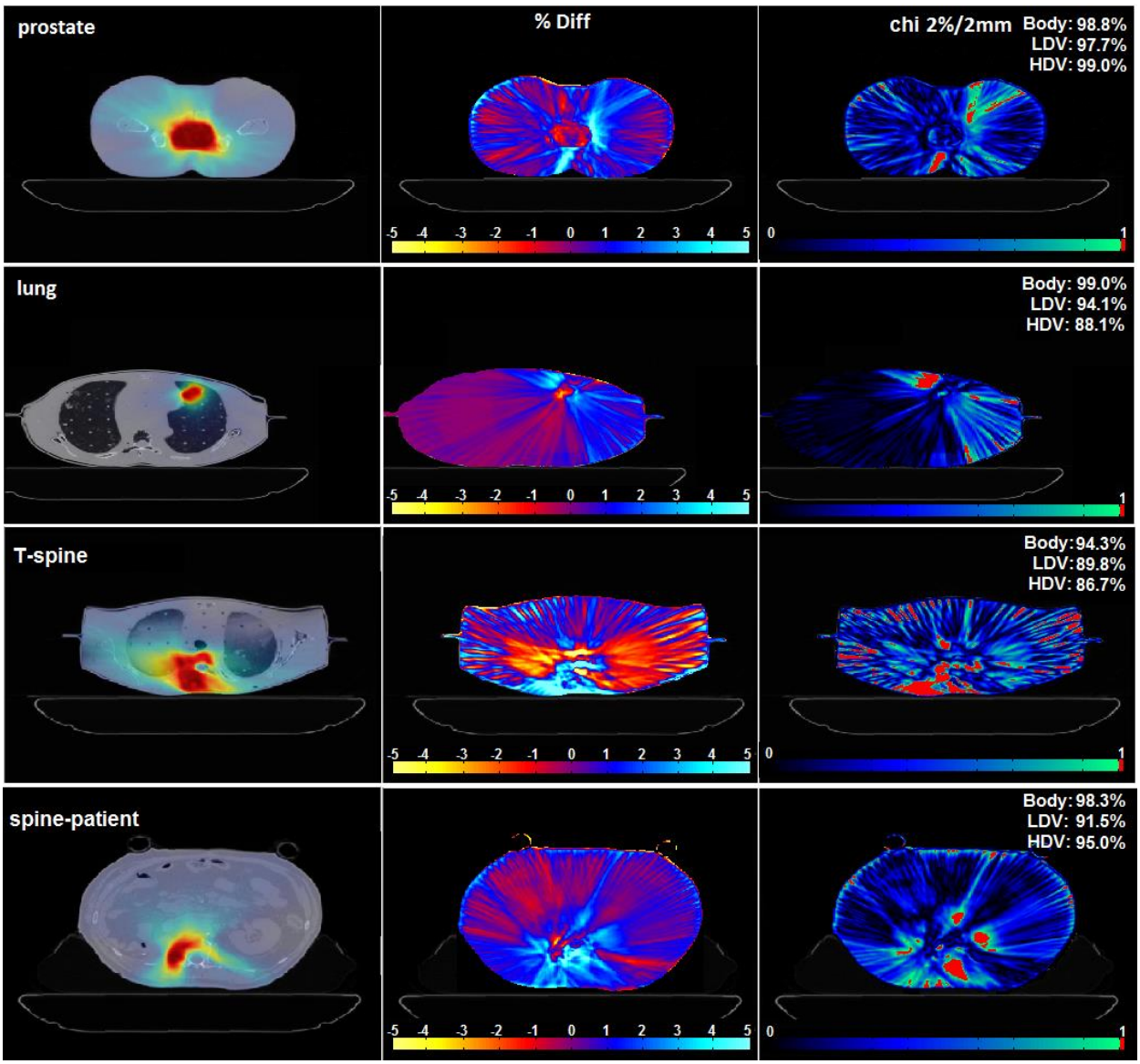

Fig. 5.4 [Phantom Reconstruction Results] The reconstructed dose overlaid on the planning CT (column 1), the ±5% percentage dose differences (column 2), and the 2%2mm χ comparison results between the TPS and our EPID model (column 3) for central transverse slices of a prostate, lung, spine, and patient data spine plan (rows 1 to 4 respectively). Red on the χ image denotes a failed voxel (χ >1).

Table 5.2. Summary of Dose Calculation Comparisons

Treatment	Region	TPS mean Dose /Model Mean Dose (Gy)	Volume Mean % Diff	χ Pass Rate (2%/2mm)	Mean χ Value	χ Pass Rate (3%/3mm)
Prostate1	Body	1.51/1.42	1.20	96.6%	0.38	99.8%
	LDV	3.46/3.31	2.03	91.1%	0.54	99.1%
	HDV	8.58/8.41	2.14	91.4%	0.53	98.5%
Prostate2	Body	1.79/1.71	1.03	98.8%	0.01	100%
	LDV	3.65/3.53	1.43	97.7%	0.23	99.9%
	HDV	8.83/8.74	1.36	99.0%	0.46	99.9%
Lung1	Body	1.05/1.00	0.63	98.9%	0.22	99.9%
	LDV	8.66/8.47	2.73	97.8%	0.34	99.7%
	HDV	18.36/18.58	2.81	89.5%	0.46	94.8%
Lung2	Body	1.05/1.00	0.57	99.1%	0.20	99.9%
	LDV	6.94/6.80	2.54	94.1%	0.42	99.1%
	HDV	15.16/15.32	2.86	88.8%	0.52	94.8%
Lung3	Body	0.67/0.63	0.47	99.0%	0.16	99.9%
	LDV	4.06/3.94	1.55	94.1%	0.40	98.0%
	HDV	8.85/8.97	2.10	88.1%	0.52	95.0%
T-spine	Body	1.10/1.07	1.02	94.3%	0.34	98.8%
	LDV	2.78/2.78	1.82	89.8%	0.49	97.9%
	HDV	6.27/6.27	2.01	86.7%	0.54	95.6%
C-spine	Body	1.52/1.43	1.94	90.0%	0.48	97.6%
	LDV	3.45/3.33	2.90	86.5%	0.55	97.7%
	HDV	7.26/7.29	2.55	85.5%	0.55	93.4%
Lung (patient data)	Body	0.52/0.51	0.25	99.3%	0.10	99.9%
	LDV	4.90/4.95	1.70	95.5%	0.41	99.7%
	HDV	12.51/12.60	2.55	86.3%	0.51	94.6%
Spine (patient data)	Body	0.61/0.59	0.29	98.3%	0.10	99.7%
	LDV	4.77/4.62	1.64	91.5%	0.43	98.8%
	HDV	11.79/11.58	2.34	95.0%	0.42	99.5%

5.3.4 Discussions

An SBRT linac head model was successfully simulated using Monte Carlo methods and verified with measured water tank data to within 1.4% of maximum dose. A 'forward' prediction algorithm was customized in order to perform EPID-based patient dose

reconstructions for SBRT beams. These algorithms were optimized and verified using open and water-attenuated static fields. Testing was extended to SBRT-VMAT delivery where the dose delivered to a phantom and actual patient data were reconstructed from EPID images. Using a stringent 2%/2mm χ-comparison, the TPS and EPID reconstructed dose for the phantom data demonstrated a minimum 91% pass rate for the prostate plans, a minimum 88% pass rate for the lung plans, and a minimum 86% pass rate for the spine plans in all defined dose regions. A lung SBRT patient study by van Elmpt *et al.*[30], which also uses a Monte Carlo based EPID image reconstruction algorithm, gave 3%/3mm isocentre slice pass rates comparable to our total volume 3%/3mm results. Another group, which also uses transmission EPID images in order to calculate patient dose, documented an average 3D gamma pass rate of 99% for nine hypo-fractioned IMRT rectum plans in the LDV region[31]. This was comparable to our hypo-fractionated prostate LDV region pass rates which, on average, were 99.5%. Both the prostate and C-spine SBRT-VMAT χ-pass rates were comparable to our non SBRT-VMAT χ-pass rates for prostate (92.7-98.2%) and head-and-neck respectively (79.9-88.6%)[11]. The patient data results were comparable to what was found for the phantom results and were clinically acceptable using a 3%/3mm test (>98%). We are presently applying this method to clinical SBRT-VMAT patient data.

It is important to note that the TPS calculates dose from a number of discrete control points with static MLC positions. The EPID reconstructed dose, which contains the effects of MLC motion and any dose delivery errors during treatment, will not be exactly the same as the TPS calculated dose, even in phantom delivery situations. The MLC leaf motion becomes increasingly blurred in the EPID images with increased frame-averaging. Optimization of the

number of frames averaged per EPID image would also be useful to minimize this effect and we are presently investigating this.

The lung and spine plans showed larger dose volume differences than the prostate plans. These are partially due to differences between the analytical anisotropic algorithm (AAA) dose calculation used by the TPS and our model's collapsed cone convolution (CCC) calculation. These dose calculation differences have been well documented[11,32-35] and are known to be similar in homogeneous cases, but noticeably different for heterogeneous situations. In order to quantify the differences between algorithms a comparison between our forward model CCC dose calculation, the Eclipse AAA calculation, and a Monte Carlo (MC) calculated dose were performed (this also validated our model's implementation of the CCC calculation)[11]. We determined that the AAA dose calculation in the lung can be between 2-5% less than the CCC result. More importantly, the AAA dose in tissue exiting the lung can over predict the dose up to 5% while bone had over predictions as large as 8% with respect to the CCC result. This was comparable to the errors seen in our lung and spine reconstructions where the largest voxel failing regions were posterior of the lung. This is clearly seen in the percentage difference image of the 'T-spine' plan given in Figure 5.4; an under prediction within the lung (red-to-yellow) and an over prediction posterior of the lung (cyan). In general the largest disagreement in dose algorithms occurs in the bone and this why the C-spine reconstruction had the lowest pass rates due to the head-and-neck bones. From this analysis, as well as the work of Han *et al.*[32,33], there is motivation to implement the Acuros XB (Varian Medical Systems, Palo Alto, CA) dose algorithm for Eclipse which will give better dose comparison results.

Finally, our group has investigated various methods to accurately define the gantry angle per EPID image[25,36]. This is essential in order to accurately determine time dependent dose information during VMAT. Furthermore, it will be more important when dealing with complex anatomical disease sites such as head and neck, spine, or lung because each EPID image will be affected by slight changes in transit dosimetry due to differing densities (i.e., bone, lung/air, etc.). Dose reconstructions using the actual EPID image header angle always gave noticeably lower χ-pass rates and higher average percentage differences than the reconstructions using the adjusted header angle as described in Section 5.2.3. For example, a reconstruction of the T-spine plan using the angles in the EPID image header gave an HDV pass rate of 80%, which was 6.7% lower than the adjusted header angle reconstruction.

5.4 CONCLUSIONS

We have customized an accurate, physics-based patient-dose reconstruction model for SBRT-VMAT delivery using on treatment, continuous mode EPID images. The model was validated using prostate, lung, and spine SBRT-VMAT treatment plans, demonstrating accurate dose reconstruction in an anthropomorphic phantom as well as some patient data. We have also demonstrated clinically acceptable accuracy using the conventional 3%/3mm tolerance. The methods discussed in this study can be applied to any EPID-equipped linac. We are currently implementing this model (and our other linac models) clinically as both an offline verification tool[37] and as a real-time error analysis tool[38].

REFERENCES

1. Kollar, L. & Rengen, R., *Stereotactic body radiotherapy*, Semin. Oncol., 2014, **41**(6), p. 776-89.
2. Greer, P.B. and Popescu, C.C., *Dosimetric properties of an amorphous silicon electronic portal imaging device for verification of dynamic intensity modulated radiation therapy*, Med Phys, 2003, **30**, p. 1618-1627.
3. McCurdy, B.M., and Greer, P.B., *Dosimetric properties of an amorphous-silicon EPID used in continuous acquisition mode for application to dynamic and arc IMRT*, Med Phys, 2009, **36**(7), p. 3028-39.
4. McCurdy, B.M. and Pistorius, S., *Photon scatter in portal images: physical characteristics of pencil beam kernels generated using the EGS Monte Carlo code*, Med Phys, 2000, **27**(2), p. 312-20.
5. McCurdy, B.M. and Pistorius, S., *Photon scatter in portal images: accuracy of a fluence based pencil beam superposition algorithm*, Med Phys, 2000, **27**(5), p. 913-22.
6. McCurdy, B.M. and Pistorius, S., *A two-step algorithm for predicting portal dose images in arbitrary detectors*, Med Phys, 2000, **27**(9), p. 2109-16.
7. McCurdy, B.M., Luchka, K., and Pistorius, S., *Dosimetric investigation and portal dose image prediction using an amorphous silicon electronic portal imaging device*, Med Phys, 2001, **28**(6), p. 911-24.
8. Chytyk, K. and McCurdy, B.M., *Investigation of tilted dose kernels for portal dose prediction in a-Si electronic portal imagers*, Med Phys, 2006, **33**(9), p.3333-9.
9. Chytyk, K. and McCurdy, B.M., *Comprehensive fluence model for absolute portal dose image prediction*, Med Phys, 2009, **36**(4), p. 1389-98.
10. Chytyk-Praznik, K., van Uytven, E., van Beek, T., McCurdy, B.M. and Greer, P.B., *Model-based prediction of portal dose images during patient treatment*, Med Phys, 2013, **40**(3), p. 031713.
11. Van Uytven, E., Van Beek, T., McCowan, P.M., Chytyk-Praznik, K., Greer, P.B. and McCurdy, B.M., *Validation of a method for in vivo 3D dose reconstruction for IMRT and VMAT treatments using on-treatment EPID images and a model-based forward-calculation algorithm*, Med Phys 2015, **42**(12), p.6945-54.
12. Otto K., *Volumetric modulated arc therapy: IMRT in a single gantry arc*, Med Phys, 2008, **35**(1), p. 310-318.
13. Olaciregui-Ruiz, I., Rozendaal, R., Mijnheer, B., van Herk, M., and Mans, A., *Automatic in vivo portal dosimetry of all treatments*, Phys Med Biol, 2013, **58**(22), p. 8253-8264.
14. Liu, B., Adamson, J., Rodriguez, A., Zhou, F., Yin, F.F., and Wu, Q., *A novel technique for VMAT QA with EPID in cine mode on a Varian TrueBeam linac*, Phys Med Biol, 2013, **58**(19), p. 6683-6700.
15. Dieterich, S., and Sherouse, G.W., *Comparison of seven commercial dosimetry diodes for SRS*, Med Phys, 2011, **38**(7), p.4166-4173.
16. Mellenberg, D.E., *Determination of build-up region over-response corrections for a Markus-type chamber*, Med Phys, 1990, **17**(6), p. 1041-1044.
17. Scott, A.J.D., Nahum, A.E. and Fenwick, J.D., *Using Monte Carlo model to predict dosimetric properties of small radiotherapy photon fields*, Med Phys, 2008, **35**(10), p. 4671-4684.

18. Rogers, D.W., Faddegon, B.A., Ding, G.X., Ma, C.M., We, J. and Mackie, T.R., *BEAM: a Monte Carlo code to simulate radiotherapy treatment units*, Med Phys, 1995, **22**(5), p. 503-24.
19. Rowshanfarzad, P., McCurdy, B.M., Sabet, M., Lee, C., O'Connor, D.J. and Greer, P.B., *Measurement and modelling of the effect of support arm backscatter on dosimetry with a Varian EPID*, Med Phys, 2010, **37**, p.2269-2278.
20. Kirkby C. and Sloboda, R., *Comprehensive Monte Carlo calculation of the point spread function for a commercial a-Si EPID*, Med Phys, 2005, **32**, p.1115-1127.
21. Ahnesjo, A., *Collapsed cone convolution of radiant energy for photon dose calculation in heterogeneous media*, Med Phys, 1989, **16**, p.577-592.
22. Varian Medical Systems: On-Board imager® Advanced Imaging, Customer Release Note ver.1.5.18, (2011).
23. Bakai, A., Alber, M., and Nusslin, F., *A revision of the gamma-evaluation concept for the comparison of dose distrbutions*, Phys Med Biol, 2003, **48**, p. 3543-3553.
24. Ansbacher, W., Swift C.L., and Greer, P.B., *An evaluation of cine-mode 3D portal image dosimetry for Volumetric Modulated Arc Therapy*, J Phys: Conf Ser., 2010, **250**(1) p. 012022.
25. McCowan, P.M., Rickey, D., Rowshanfarzad, P., Greer, P.B., Ansbacher, W., and McCurdy, B.M., *Investigation of gantry angle data accuracy for cine-mode EPID images acquired during arc-IMRT*, J App Clin Med Phys, 2014, **15**(1), p. 1-15.
26. Varian Medical Systems: CAP-IX-G.doc, Customer Acceptance Procedure, revision G, (2009).
27. Varian Medical Systems: CAP-ML-P.doc, Customer Acceptance Procedure, revision P, (2008).
28. Ezzell, G.A., *et al*., *IMRT commissioning: multiple institution planning and dosimetry comparisons, a report from AAPM Task Group 119* Med. Phys., 2009, **36**(11), p. 5359-73.
29. Mancuso, G. M., Fontenot, J. D., Gibbons, J. P., and Parker, B. C., *Comparison of action levels for patient-specific quality assurance of intensity modulated radiation therapy and volumetric modulated arc therapy treatments*, Med Phys, 2012, **39**(7), p. 4378–4385.
30. van Elmpt, W., Petit, S., Ruysscher, D.D., Lambin, P. and Dekker, A., *3D dose delivery verification using repeated cone-beam imaging and EPID dosimetry for stereotactic body radiotherapy of non-small cell lung cancer*, Radiother Oncol, 2010, **94**, p.188-194.
31. McDermott, L.N, Wendling, M., Nijkamp, J., Mans, A., Sonke, J.J., Mijnheer, B.J. and van Herk, M., *3D in vivo dose verification of entire hypo-fractionated IMRT treatments using an EPID and cone-beam CT*, Radiother. Oncol., 2008, **86**(1), p. 35-42.
32. Han, T., Mikell, J.K., Salehpour, M., and Mourtada, F., *Dosimetric comparison of Acuros XB deterministic radiation transport method with Monte Carlo and model-based convolution methods in heterogeneous media*, Med Phys, 2011, **38**, p. 2651-2664.
33. Han, T. *et al*., *Dosimetric impact of Acuros XB deterministic radiation transport algorithm for heterogeneous dose calculation in lung cancer*, Med Phys, 2013, **40**(5), p. 051710.
34. Hasenbalg, F., Neuenschwander, H., Mini, R., and Born, E.J., *Collapsed cone convolution and analytical anisotropic algorithm dose calculations compared to*

VMC++ Monte Carlo simulations in clinical cases, Phys Med Biol, 2007, **52**, p. 3679-3691.
35. Aarup L.R. *et al*., *The effect of different lung densities on the accuracy of various radiotherapy dose calculation methods: implications for tumour coverage*, Radiother Oncol, 2009, **91**, p.405-414.
36. Woodruff, H.C., Fuangrod, T., Rowshanfarzad, P., McCurdy, B.M, and Greer, P.B., *Gantry-angle resolved VMAT pretreatment verification using EPID image prediction*, Med Phys, 2013, **40**(8), p. 081715.
37. Asuni, G., vanBeek, T., McCowan, P.M., VanUytven, E., and McCurdy, B.M., *Clinical Implementation of EPID-based daily in vivo dose verification system for SBRT patients*, ASTRO 56th annual conference, 2014.
38. Woodruff, H.C. *et al*., *Initial experience with an EPID-based, real-time error monitoring system for radiation therapy*, 13th International Conference on Electronic Patient Imaging, 2014.

CHAPTER SIX: FRAME AVERAGE OPTIMIZATION OF CINE-MODE EPID IMAGES USED FOR *IN VIVO* PATIENT DOSE VERIFICATION OF VMAT DELIVERIES

In this chapter, the analyses involved in optimizing the frame averaging number per EPID image for VMAT deliveries are discussed. This was performed in order to reduce the reconstruction calculation time while still maintaining a certain level of accuracy. The optimization was determined using data from 12 different types of VMAT patient plans. Overall, frame average numbers of 9 and 11 were determined to provide acceptable dose reconstruction accuracy for VMAT and SBRT-VMAT respectively. This chapter was published in the peer-reviewed journal Medical Physics[†]

6.1 INTRODUCTION

Volumetric modulated arc therapy (VMAT) is now a common form of radiation treatment. VMAT delivers conformal beams of radiation while rotating in an arc around the patient. Karl Otto developed a method for optimizing the dose delivery, gantry speed, and multi-leaf collimator (MLC) positions for VMAT into discrete control points (CPs), which are functions of the linac's gantry angle[1]. The linear accelerator (linac) can dynamically change the MLCs, gantry speed, dose rate, and even the collimator angle during VMAT delivery. VMAT has been shown to have comparable or better tumor coverage and healthy tissue sparing than IMRT while requiring roughly half the delivery time[2-5]. Both Elekta's

†-P McCowan and B.M.C. McCurdy, *Frame average optimization of cine-mode EPID images used for in vivo patient dose verification of VMAT deliveries*, Med. Phys., 43(1), p.254-61 (2016).

VMAT (Elekta AB, Stockholm, Sweden) and Varian's RapidArcTM (Varian Medical Systems, Palo Alto, CA) are capable of delivering this complex therapy.

Most commercial linacs come equipped with an electronic portal imaging device (EPID) capable of measuring exit fluence (as dose) downstream from the patient. The EPID acquires image data in either an 'integrated' or a 'cine' (continuous) mode. Cine-mode acquires frames at a specific frequency while also allowing for integral averaging of these frames into 'frame-averaged' EPID images. The EPID has been shown to be an accurate dosimeter and dose verification tool while operated in either the integrated or cine acquisition modes[6-9]. However, cine-mode is required in order to obtain the time dependant dose information of VMAT delivery.

Frame averaging reduces the overall number of images acquired per arc but also introduces artefacts leading to degradation or 'blurring' of dosimetric data. This is because the linac's dynamic delivery information is being mapped onto static sets of images, essentially integrating images over many small sub-arcs of the gantry rotation. The magnitude of the blurring is a function of the gantry angle change per image acquired, which in turn depends on frame acquisition rate, frame average number, and the linac's gantry speed. Generally, with a faster gantry speed, a lower frame averaging number should be chosen.

Our group has successfully developed a robust, physics-based *in vivo* dose verification model for both VMAT and IMRT treatments using on-treatment EPID images[10]. Other

groups have also used the EPID for *in vivo* and/or pre-treatment dose verification[11-16]. The main benefit of optimizing the frame averaging for any EPID image based dose reconstruction model is the reduction in 3D patient dose calculation time. However, the reduced number of images must be weighed against the loss of dosimetric accuracy.

The goal of this investigation was to determine an optimal frame average number for cine-mode EPID images acquired during VMAT as a function of the linac's average gantry speed (i.e., determined by the dose delivered per fraction). The methods described here can be applied to any linac equipped with a cine-capable EPID.

6.2 MATERIALS AND METHODS

6.2.1 A Linac setup and frame acquisition

All data were acquired using a model 2300ix Varian linac equipped with an aS1000 EPID. The EPID was operated in full resolution mode (employing a 40x30 cm^2 panel of 1024x768 pixels) with a frame acquisition rate, *f*, of 7.5 Hz. It has been determined that there is an upper limit (~200) on the number of EPID images one can save to the clinical computer during treatment[17,18]. This virtual memory limitation of the On-Board Imager[19] needed to be circumvented in order to capture the single-frame cine EPID images which represent the highest angular resolution. This was achieved through a frame-grabber card (Matrox Solios SOL 2M EV CLB) with associated software (iTools Capture, Varian Medical Systems) which was installed on a designated PC that connects in parallel to the frame processing

board of the 4DTC treatment computer. This allowed for continuous capturing of single EPID frames during beam-on. The single frames were 'frame-averaged' to desired values using MATLAB (MathWorks Inc., Natick, MA) code developed in-house. The frame-grabber system did not disrupt normal operation of the linac.

Twelve different 6MV VMAT patient plans to an anthropomorphic phantom (RANDO® The Phantom Laboratory, Salem NY, USA) were delivered. Each patient plan, created in the Eclipse (Varian Medical Systems, Palo Alto, CA) treatment planning system (TPS), delivered a counter-clockwise (ccw) and clockwise (cw) arc. Dose rates of 600 MU/min for regular VMAT and 1000 MU/min for SBRT-VMAT were employed. The patient plans were chosen to represent a spectrum of VMAT-type treatments currently commissioned at our clinic. The plans delivered were: 4 prostate plans including 1 high-risk plan (CTV includes at-risk lymph node and seminal vesicle regions), 2 head-and-neck (H&N), 2 SBRT prostate, 2 SBRT lung, and 2 SBRT spine. Specific plan details are given in Table 6.1. The average gantry speed, $\bar{v}_g$, was calculated as:

$$\bar{v}_g = \frac{L \cdot f}{N_f} \qquad [6.1]$$

where L is the arc length, f is the EPID frame acquisition rate, and N_f is the number of EPID frames acquired. In Table 6.1, the average gantry speed column is the mean of the average gantry speeds calculated for each arc. The average gantry speed can also be estimated from the plan's CP data defined in the TPS.

Table 6.1 VMAT Treatment Delivery Details

Plan Type	Fraction Dose (Gy)	Arc length L	Number of EPID frames N_f (ccw/cw)	Average gantry speed $\overline{v}_g$ (°/s)
prostate1	2.0	358°	557/566	4.78
prostate2	2.0	358°	562/569	4.75
prostate3	2.0	358°	562/568	4.75
prostate-hi	2.0	358°	560/573	4.74
H&N1 (hypopharynx)	2.0	358°	556/568	4.78
H&N2 (nasopharynx)	2.1	358°	555/567	4.78
SBRT-prostate1	8.0	358°	728/725	3.69
SBRT-prostate2	8.0	358°	870/862	3.10
SBRT-lung1(upper-anterior)	12.0	199°	1007/1008	1.48
SBRT-lung2(lower-posterior)	12.0	204°	1057/1048	1.45
SBRT-spine1 (mid-thoracic)	6.0	358°	681/679	3.94
SBRT-spine2 (mid-cervical)	6.0	358°	596/619	4.26

6.2.2 Frame averaging error

For each plan delivered, the frames acquired by the frame-grabber were averaged into select sets of frame-averaged EPID images using MATLAB code. We arbitrarily chose ten degrees to be the maximum allowable angle subtended per frame-averaged EPID image. Therefore, frame averaging was performed in factors of 3 up to a maximum of 15 for the non-SBRT VMAT plans and up to 51 for the lung SBRT-VMAT plans due to their slower gantry speeds. An EPID data set consisting of the non-averaged frame-grabber frames was constructed for each plan, and was considered the most accurate data due to its minimum subtended arc per frame. The dose reconstruction from the non-averaged frame-grabber frames was compared to all the frame-averaged patient dose reconstructions. The average

angle subtended per EPID image was calculated by dividing the arc length, *L*, by the total number of frame-averaged EPID images.

For every frame-averaged EPID data set the dose delivered to the phantom was calculated using the methods described previously by our group[8,9,10]. In general, this method combines Monte Carlo modelled parameters with physical models to predict EPID images. The predicted image is compared to a corresponding measured image whereby the measured primary fluence is isolated by removing the predicted scattered components. This primary fluence is then back projected to a plane above the patient, converted to TERMA in the patient, which is then used in a 3D superposition calculation with point-dose kernels. The 'superposition calculation' of patient dose is based on Ahnesjö's collapsed cone convolution (CCC)[20] method using a resolution of 160 cones. The accuracy of our CCC implementation has been validated against Monte Carlo data[10].

To characterize the error introduced by increased frame averaging a comparison between the dose calculated from each frame-averaged data set and the single frame data set using our reconstruction model was performed. Mean percentage dose differences were calculated for two defined dose volume regions: a lower dose volume (LDV) region for voxels receiving between 20% and 80% of the prescribed dose, and a high dose volume (HDV) region for voxels receiving >80% of the prescribed dose.

For this work an unacceptable loss of accuracy as a greater than 1% mean dose difference in the HDV (or LDV) due to the frame-averaging error was defined. Therefore, any frame-

averaged mean dose value that differed by more than 1% from the single frame reconstruction mean dose value was considered to be unacceptable. The data is presented in order to select any arbitrary level of accuracy.

The mean dose difference results were plotted as functions of the average angle subtended by the frame-averaged EPID images, $\bar{\theta}_e$. After determining an optimized subtended angle per EPID image, $\langle\bar{\theta}_e\rangle$, using the 1% dose difference tolerance, the following equation was used to convert this to an optimized frame averaging number, $\langle n_{avg}\rangle$:

$$\langle n_{avg}\rangle = \frac{N_f}{N_I} = \left(\frac{L \cdot f}{\bar{v}_g}\right) \cdot \left(\frac{L}{\langle\bar{\theta}_e\rangle}\right)^{-1} = \left\lfloor \frac{\langle\bar{\theta}_e\rangle}{\bar{v}_g} \cdot f \right\rfloor \qquad [6.2]$$

where N_I is the number of frame-averaged EPID images acquired per arc length L and the other parameters are defined in Section 6.2.1. Floor brackets are used in Eq. 6.2 to calculate a rounded-down integer for n_{avg} which is required by the software.

6.2.3 Frame averaging effects

Theoretically, there will be two dose reconstruction errors produced when using higher frame-averaged EPID images. Firstly, there will be an error due to the averaging of the EPID-measured delivery information over a sub-arc angle, which the gantry rotated through, during the EPID image acquisition. The effect, illustrated in Fig. 6.1, will be more prominent further away from beam isocentre and smallest at beam isocentre. All the information within the yellow triangle is collapsed (averaged) into one image angle projected through the patient. We describe this as a geometric frame averaging error.

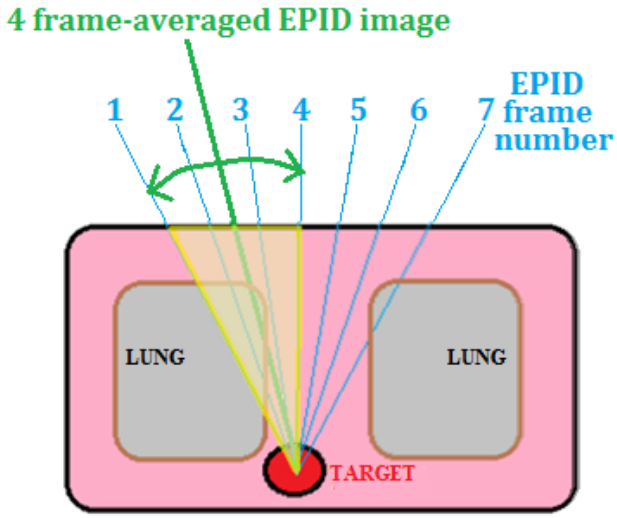

Fig. 6.1 [Geometric Frame Averaging Error]: An illustration (not to scale) of the geometric frame averaging error. All dose delivery information within the yellow triangle is 'integrated' and represented by a single gantry angle EPID image. The dosimetric error will be more pronounced in regions further away from beam isocentre (target).

The second artefact will occur due to the averaging of MLC positions captured in a frame-averaged EPID image. Our EPID image prediction model performs an interpolation of the planned MLC positions as a function of the EPID image's gantry angle. This prediction produces a static MLC-defined dose image which is then compared to a measured frame-averaged EPID dose image in order to isolate the measured primary dose. However, the measured frame-averaged EPID dose is defined by a moving MLC aperture, so the MLC aperture imaged on the EPID is blurred. The amount of blurring depends on the chosen frame averaging and the magnitude of MLC modulation (i.e., MLC leaf speed). This effect is illustrated in Fig. 6.2 for a measured EPID image using a frame averaging value of 12 (left)

and its corresponding predicted EPID image (right) produced by our model. Each measured EPID image will have some amount of MLC blurring due to averaging of the MLC positions over the image acquisition time. This will produce differences between the reconstructed doses calculated from the frame-averaged EPID images to that from the single-frame EPID images. These differences will be additive in the volume of overlap (i.e. the target region), resulting in a dosimetric error in that volume.

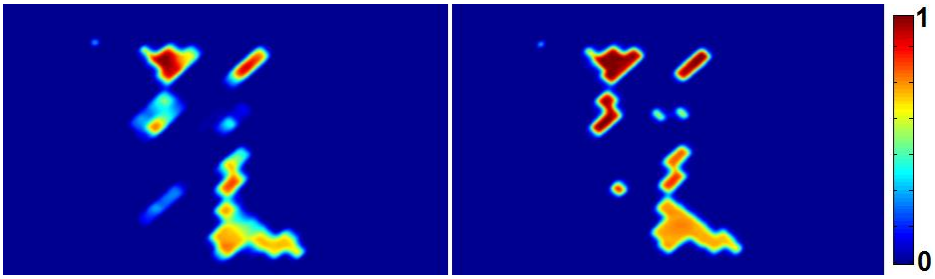

Fig. 6.2 [Predicted vs Measured MLC Images]: EPID measured MLC field (left – 12 frames averaged) and our predicted EPID MLC field (right) for a specific gantry angle from a VMAT arc. The different MLC fields will introduce errors when our dose reconstruction model isolates the measured primary dose.

To investigate the magnitude of this effect, a VMAT plan was created to deliver a static 5x5 cm^2 field at every control point, thus eliminating the MLC modulation. This effect was further characterized by modifying this same plan to deliver an opening and closing 5x5 cm^2 MLC square field with varying slow and fast leaf speeds. For both approaches dose reconstructions for variable frame averaging were performed and then analysed as outlined in Section 6.2.2. The modifications to the treatment plan file were performed using software written in MATLAB.

We calculated the average MLC leaf speed of each plan. This was determined by multiplying the MLC displacements between control points, by the average gantry speed, from Eq. 6.1, and dividing by the angle per control point. Only moving leaves were used for the calculation.

6.2.4 EPID image gantry angle

It has been previously determined that the gantry angle defined in the header of the clinical EPID images can be incorrect by as much as ±3 degrees[17,21]. The EPID frames acquired with the frame-grabber do not have gantry angle information in their headers so we employed the angle acquisition method used by Woodruff *et al*.[22]. This method utilizes the angles recorded in the kV frame headers, which can be acquired simultaneously with the MV frames. The accuracy of the kV angle data was verified to be within ± 0.6° of the actual gantry angle by Woodruff *et al*.[22.] The kV frame data were acquired at 15 Hz.

While operating the EPID in cine-mode the first 1 or 2 frames of acquisition are not saved by the clinical system (non-valid). Furthermore, the last 1 or 2 frames are also not saved (also non-valid). This lost-frame effect was observed by our group[17] and the reason why these images are not saved is due to the acquisition software which was not designed with dosimetric applications in mind. During treatment only valid EPID frames are saved by the clinical treatment computer. In order to keep our results clinically relevant only the valid frame-grabber frames were averaged (valid and non-valid frames are flagged in the headers of the frame-grabber MV frames). For a typical VMAT delivery (> 100 MU/min) the additional dose data acquired by non-valid beam-on frames are insignificant (<1%) when

compared to the total dose acquired by the valid frames (between 2 and 4 out of 500 to 1000 total frames)[17,22,23].

6.3 RESULTS AND DISCUSSION

6.3.1 Frame averaging effect

The artefacts introduced into the dose reconstruction due to increased frame averaging are illustrated in Fig. 6.3 for the SBRT-spine1 plan. Transverse, central axis (CAX) dose difference images between the various frame-averaged patient dose reconstructions and the single frame EPID reconstructions are shown. The $\bar{\theta}_e$'s are given in the bottom left corner of each image and the EPID reconstructed dose overlayed on the CT CAX slice is given in the upper left as a target dose reference. Two artefacts related to increased frame-averaging dominate the reconstruction results: 1) a geometric out-of-target error appearing as 'streaks' or 'spokes' and 2) a target-specific error.

The geometric error occurs because of the averaging of the EPID-measured delivery information over the sub-arc angle that the gantry rotated through during the EPID image acquisition as described in Section 6.2.3. The magnitude of the geometric error increases as frame averaging increases.

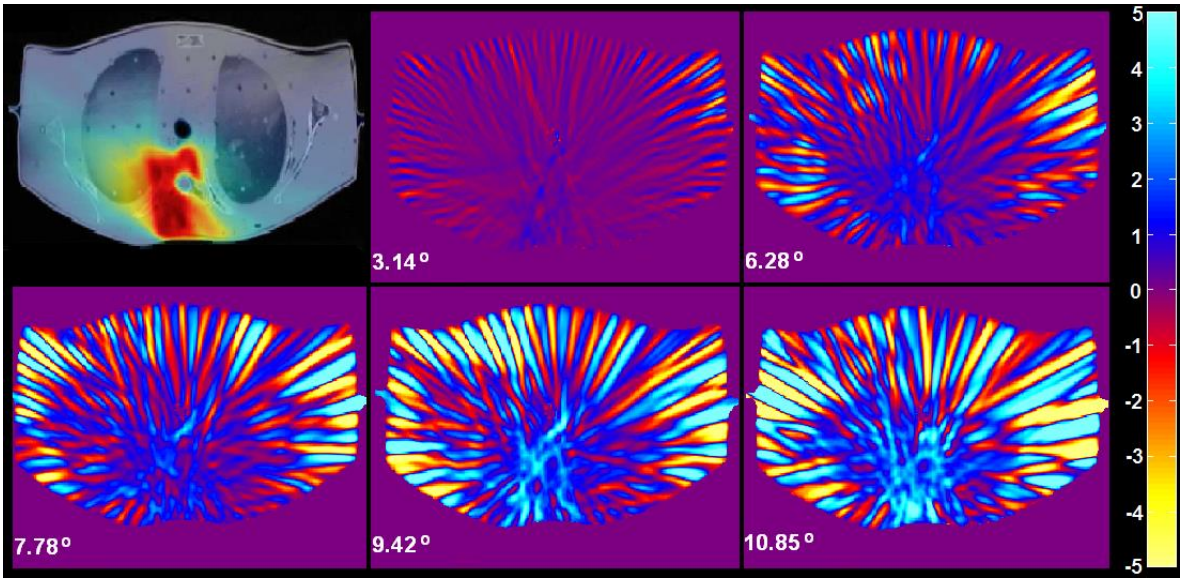

Fig. 6.3 [Frame Averaging Effect]: Dose difference images of CAX transverse slices of the single EPID frame reconstruction minus the frame-averaged EPID dose reconstructions for the SBRT-spine1 plan. The EPID image's angular resolution, $\bar{\theta}_e$, is given in the bottom corner of each difference image. The top left image is the reconstructed dose overlayed on the CT data for anatomical reference. A noticeable increase in reconstruction artefacts are illustrated for $\bar{\theta}_e$'s greater than 3°. An observable error in the target dose was also observed as frame averaging increased.

The target-specific error is likely due to the blurring of MLC motion over the imaging time, and increases with frame averaging. To characterize the MLC motion blurring effect as a function of frame averaging, a simple 5x5 cm^2 MLC-defined field plan was created with the each bank of leaves uniformly sweeping back and forth across the field. Three plan versions contained high speed, low speed, and completely static MLC movement. When the plan with no MLC modulation was delivered, the error observed in the target region from the frame-averaged reconstructions compared to the single frame reconstruction (as seen in Fig. 6.3), was no longer visible, and only the geometric frame averaging error (spokes) was present. The error in the target was largest when the MLC leaf speeds were the fastest. Typically, not all MLC leaves will be moving at the same speed and collectively in the same direction in a plan, but the analysis demonstrates that the faster the MLC leaves travel, the

more blurring per frame-averaged EPID image, and the less accurate our dose reconstruction results are within the target.

To more accurately compare measured and treatment-planned predicted dose volumes, one could attempt a de-blurring of each measured EPID image. However, a de-blurring algorithm will introduce systematic errors and was therefore decided to not implement any additional image processing at this time.

6.3.2 Frame averaging error: non-SBRT VMAT

In order to quantify the errors introduced by frame averaging, each frame-averaged patient reconstructed 3D dose distribution was compared to the single frame reconstructed dose. Fig. 6.4 shows the HDV and LDV absolute mean percentage dose differences with respect to the single frame EPID reconstruction plotted as a function of $\bar{\theta}_e$ for the non-SBRT VMAT plans. The H&N1 plan required the highest EPID image angular resolution with $\bar{\theta}_e$ < 6.0°. The H&N2 plan was within the 1% dose difference tolerance up to 7.8° per EPID image. Two of the prostate plans exhibited minimal HDV dose differences at $\bar{\theta}_e$ = 10°, while another was $\bar{\theta}_e$ = 9.0°. The high-risk prostate plan, which had the largest HDV, required a $\bar{\theta}_e$ < 7.0° in order to remain within the 1% tolerance. The mean percentage dose differences of the HDV's and LDV's of all plans generally increased at a constant rate for larger $\bar{\theta}_e$ and were all within 1% of the single frame result for $\bar{\theta}_e$ < 7.5° except for the HDV region of the H&N1 plan. The high-risk prostate plan exhibited the largest LDV error as frame averaging increased. The optimized non-SBRT VMAT data are summarized in Table 6.2.

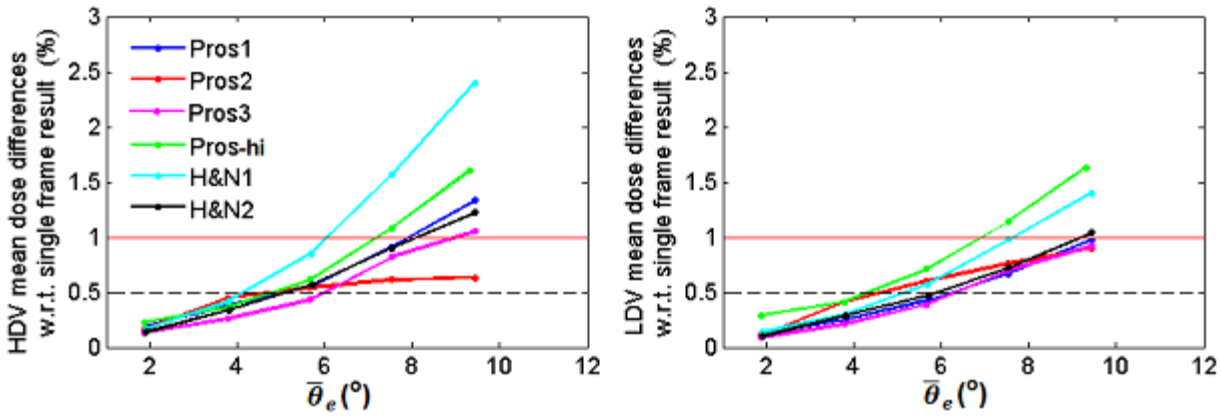

Fig. 6.4 [VMAT Frame-Averaged Dose Differences]: The absolute mean dose differences of the HDV (a) and LDV (b) of each frame-averaged data set compared to the single frame result, plotted as a function of the average angle subtended by the EPID image, $\bar{\theta}_e$, for the non-SBRT VMAT plans. Tolerances of 1% (red solid) and 0.5% (black dash) are given.

6.3.3 Frame averaging error: SBRT-VMAT

Figure 6.5 shows the HDV and LDV mean percentage dose differences between the frame-averaged reconstructions and the single frame reconstruction for the SBRT-VMAT plans plotted as a function of $\bar{\theta}_e$. The HDV data show that the lung plans require an angular resolution of roughly $\bar{\theta}_e$ = 3° per EPID image to remain within 1% mean dose difference of the single frame result. The higher angular resolution needed for the lung plans is also apparent in the both the HDV and LDV mean percentage graphs where they increase in mean percentage difference faster than all the other plans. In general, the spine and prostate plans required comparable angular resolutions of roughly 7° except for the spine1 plan which had a $\langle\bar{\theta}_e\rangle = 6.2°$. The optimized data for the SBRT-VMAT plans are summarized in Table 6.2.

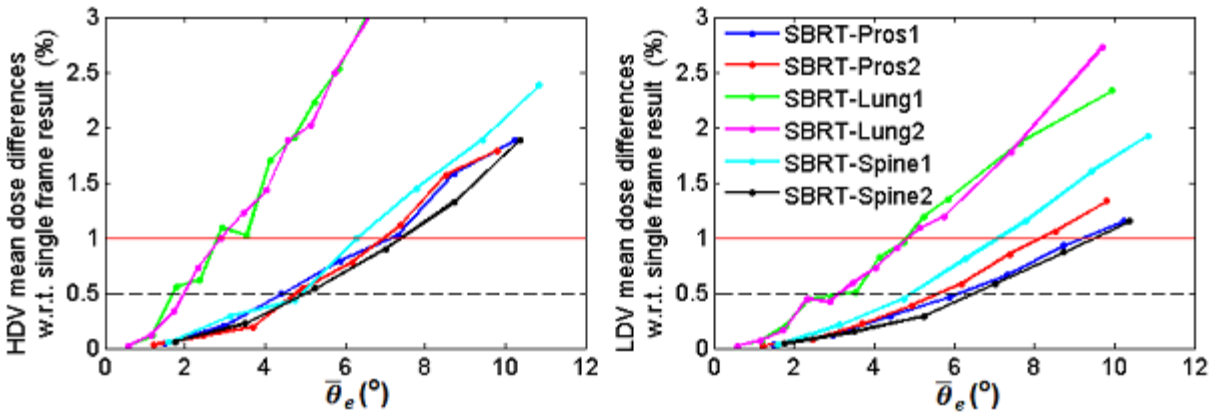

Fig. 6.5 [SBRT-VMAT Frame-Averaged Dose Differences]: The mean percentage dose differences of the HDV (a) and LDV (b) of each frame-averaged data set compared to the single frame result plotted as a function of the angle subtended by the EPID image, $\overline{\theta}_e$, for the SBRT-VMAT plans. Tolerances of 1% (red solid) and 0.5% (black dash) are given.

6.3.4 Optimization of frame averaging at 7.5Hz

From Table 6.2 it can be determined that for a frame acquisition rate of 7.5 Hz, frame averaging numbers of 9 and 11 were acceptable for all VMAT and SBRT-VMAT plans respectively in order to remain within 1% mean dose difference of the single frame result. Alternatively, using a 0.5% tolerance of the mean percentage dose difference in the high dose volume resulted in optimal frame average numbers of 6 and 8 for VMAT and SBRT-VMAT respectively. Furthermore, individual optimized frame averaging numbers can also be determined as a function of the average gantry speed or dose per fraction. In general, the HDV error was larger than the LDV error, that is, if the HDV mean dose difference was < 1% the LDV mean dose difference was <1%.

Table 6.2 Frame Averaging Optimization Results

Plan Type	average gantry speed $\bar{v}_g$ (°/s)	optimized angle per EPID $\langle\bar{\theta}_e\rangle_{1\%}$ (°)	optimized frame average $\langle n_{avg}\rangle_{1\%}$	optimized angle per EPID $\langle\bar{\theta}_e\rangle_{0.5\%}$(°)	optimized frame average $\langle n_{avg}\rangle_{0.5\%}$	Mean MLC leaf speed (mm/s)
prostate1	4.78	8.0	12	5.0	7	7.8
prostate2	4.75	10.0	15	4.4	6	7.6
prostate3	4.75	9.0	14	6.0	9	9.1
prostate-hi	4.74	7.0	11	4.8	7	9.1
H&N1	4.78	6.0	9	4.1	6	10.1
H&N2	4.78	8.0	12	5.0	7	9.4
SBRT-pros1	3.69	7.4	15	4.2	8	5.8
SBRT-pros2	3.10	7.0	16	4.6	11	6.0
SBRT-lung1	1.48	2.8	14	1.7	8	3.0
SBRT-lung2	1.45	2.9	15	2.0	10	2.8
SBRT-spine1	3.94	6.2	11	5.0	9	7.5
SBRT-spine2	4.26	7.3	12	5.0	8	6.3

It is apparent from Table 6.2 that the optimized frame averaging number decreases with increasing average gantry speed. The optimal frame averaging numbers that are within 1% and 0.5% of the mean dose in the HDV are plotted as a function of $\bar{v}_g$ in Fig. 6.6(a) and 6.6(b) respectively. Note that the gantry speed in a plan is determined primarily by the magnitude of the prescribed dose per fraction and, to a lesser extent, the magnitude of MLC modulation (i.e., leaf speed). The prescribed doses per fraction (12, 8, 6, and 2 Gy) for the treatment plans are also shown as colour columns in Fig. 6.6. A frame-averaging optimization curve connecting the most lower bound data points ensures optimal angular resolution of EPID images for all plan types in that dose per fraction region. By using these data, one can determine an optimal frame averaging number based on the average gantry speed determined from the TPS control point data or the dose per fraction. This approach ensures no more than either a 1% or 0.5% loss in the mean percentage dose difference of the

frame-averaged results compared to the ideal, single frame reconstruction. Using a 0.5% tolerance all SBRT-VMATs were acceptable using a frame averaging number of 8 while VMAT plans required 6. Similar optimization curves can be calculated for any chosen frame acquisition rate, *f*, using Eq. 6.2.

We determined a moderate correlation between the average MLC leaf speeds (given in Table 6.2) and the optimized frame averaged numbers (correlation coefficient of -0.62 and -0.54 respectively for a 1% and 0.5% tolerance). The H&N1 plan had the fastest mean leaf speed, 1.0cm/s, and required the lowest frame average number. The prostate3 and prostate-hi plans had similar mean leaf speeds but required different frame averaging. It can be inferred that the error introduced by MLC blurring is complicated and will also depend on factors such as leaf travel direction and anatomical site. Furthermore, our simplified analysis assumes the gantry speed is constant during delivery, which is not always the case for complex deliveries like spine SBRT. However, it is evident from the analysis here and in section 6.3.1, that the greater the MLC leaf blurring, due to faster MLC leaf speeds, the greater the error in our dose reconstruction.

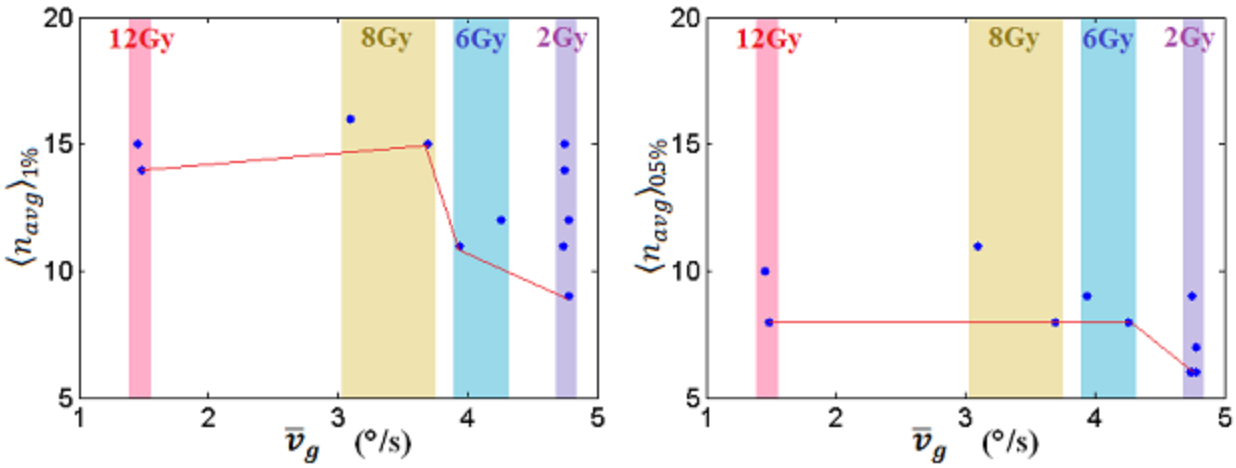

Fig. 6.6 [Optimized Frame Averaging]: The optimized frame average number, $\langle n_{avg} \rangle$, plotted as a function of the average gantry speed, $\bar{v}_g$. The doses per fraction values are given as colour columns. The optimization curves (red lines) ensure mean percentage dose differences will be within 1% (a) and within 0.5% (b) of the single frame reconstruction result.

When comparing the values for $\langle n_{avg} \rangle_{1\%}$ from Table 6.2 to the total number of acquired EPID frames from Table 6.1, the total number of frame-averaged images (from both arcs) of each plan were less than 200 (largest was 144 total images) in order to remain within 1% of the mean dose in the HDV. In order to remain within 0.5% of the mean dose in the HDV, the two SBRT lung plans exceeded the 200 image limit (252 and 212 total images). In these cases, each arc would need to be delivered like a separate plan, i.e., deliver arc 1, close the patient, open the patient, and then deliver arc 2. This work around is more time consuming and inconvenient, but would ensure better accuracy.

6.3.4 Discussion

Characterization of the error introduced by increasing the EPID frame averaging for our 3D, in vivo, patient dose reconstruction model has been carried out. The chosen acceptability requirements allowed for no more than a 1% increase to the mean percentage dose difference in the HDV region (and by implication also the LDV as shown in Fig. 6.4 and 6.5) when

compared to the single frame reconstruction. Using a frame acquisition rate of 7.5 Hz, it was determined that for all non-SBRT VMAT treatments, 9 frames averaged per EPID image was acceptable. No higher than 11 frames per EPID image was determined to be acceptable for all SBRT-VMAT treatments greater than or equal to 6 Gy/fx. Optimized frame averaging numbers were determined as a function of the linac's average gantry speed and dose per fraction. This optimization of EPID angular resolution can reduce calculation time without a significant loss in reconstruction accuracy.

At our facility all VMAT plans deliver the planned dose in two arcs. For other facilities, where a VMAT plan may deliver the dose in only one arc, the processes described here are still applicable. One defines a $\bar{v}_g$ from Eq. 6.1 and then determines a $\langle \bar{\theta}_e \rangle$ dependant on the desired accuracy (1% or 0.5%).

The incorporation of a MLC de-blurring algorithm into our dose reconstruction model may allow for slightly higher frame averaging numbers. However, it is evident from Fig. 6.4 and 6.5 that by using a 1% (or 0.5%) mean dose difference tolerance the geometric frame averaging error, dominating the LDV, becomes comparable to the MLC blurring error, dominating the HDV, when higher frame averaging is utilized. The incorporation of a de-blurring algorithm would also add extra calculation time and systematic errors. Future work will investigate the viability of this type of algorithm.

Two factors deterring the use of a low frame-averaged EPID patient dose reconstruction is the loss of EPID data during beam-on due to computer virtual memory limitations as well

as an increase in calculation time. For this work, MATLAB's parallel processing software was employed to distribute the dose calculations of each frame-averaged data set over 12 cores. The reconstruction time is linearly dependent on the number of EPID images per plan. A typical single frame reconstruction required about 15 hours, which is clinically unacceptable. The reconstruction time using 160-to-180 EPID images per treatment currently takes about 1.5 hours. This time decreases linearly with a decrease in EPID image number. We are also investigating a distributive computer system approach which will incorporate GPU processors to further reduce calculation times, but this will be the subject of a future publication.

6.4 CONCLUSION

An optimization of the EPID image frame averaging required for 3D patient dose reconstructions was performed. A tolerance of no more than a 1% change to the frame-averaged mean percentage dose difference in the high dose volume when compared to the single frame reconstruction result was used. Optimal frame averaging values were determined using a range of VMAT and SBRT-VMAT patient plans currently employed at our facility including prostate, head-and-neck, lung, and spine. The error due solely to frame averaging was determined. The analysis determined that frame averaging values of 9 and 11 provided acceptable differences for the non-SBRT and SBRT-VMAT plans respectively. Optimization curves of the frame averaging number as a function of the average gantry speed of the linac and dose per fraction were developed. The methods described here can reduce the memory load on the treatment computer and reduce the reconstruction model calculation

time without a significant loss in accuracy of the 3D patient reconstructed dose. We have successfully implemented these frame averaging optimization results into our clinical, 3D, *in vivo* and pre-treatment patient EPID dosimetry program.

REFERENCES

1. Otto K., *Volumetric modulated arc therapy: IMRT in a single gantry arc*, Med Phys, 2008, **35**(1), 310-318.
2. Holt, A. *et al*., *Multi-institutional comparison of VMAT vs IMRT for head-and-neck cancer: a planning study*, Radiother Oncol, 2013, **8**(26), doi: 10.1186/1748-717X-8-26.
3. Quan E.M., *et al*., *A comprehensive comparison of IMRT and VMAT plan quality for prostate cancer treatment*, Int J Rad Onc Biol Phys, 2012, **83**(4), p. 1169-78.
4. Abbas, A.S., Moseley, D., Kassam, Z., Kim, S.M., and Cho, C., *Volumetric-modulated arc therapy for the treatment of a large planning target volume in thoracic esophageal cancer*, J Appl Clin Med Phys, 2013, **14**(3), p. 192-202.
5. Peters, S., Schiefer, H., and Plasswilm, L., *A treatment planning study comparing Elekta VMAT and fixed field IMRT using the varian treatment planning system eclipse*, Radiother Oncol, 2014, **9**(153), doi: 10.1186/1748-717X-9-153.
6. McCurdy, B.M., Luchka, K., and Pistorius, S., *Dosimetric investigation and portal dose image prediction using an amorphous silicon electronic portal imaging device*, Med Phys, 2001, **28**(6), p. 911-24.
7. McCurdy, B.M., and Greer, P.B., *Dosimetric properties of an amorphous-silicon EPID used in continuous acquisition mode for application to dynamic and arc IMRT*, Med Phys, 2009, **36**(7), p. 3028-39.
8. Chytyk, K. and McCurdy, B.M., *Comprehensive fluence model for absolute portal dose image prediction*, Med Phys, 2009, **36**(4), p. 1389-98.
9. Chytyk-Praznik, K., van Uytven, E., van Beek, T., McCurdy, B.M. and Greer, P.B., *Model-based prediction of portal dose images during patient treatment*, Med Phys, 2013, **40**(3), p. 031713.
10. vanUytven, E., van Beek, T., McCowan, P.M., Chytyk-Praznik, K., Greer, P.B. and McCurdy, B.M., *Validation of a method for in vivo 3D dose reconstruction for IMRT and VMAT treatments using on-treatment EPID images and a model-based forward-calculation algorithm*, Med Phys 2015, **42**(12), p.6945-54.
11. Piermattei, A. *et al*., *In patient dose reconstruction using a cine acquisition for dynamic arc radiation therapy*, Med Biol Eng Comput, 2009, **47**(4), p. 425-433.
12. Mans, A. *et al*., *3D Dosimetric verification of volumetric-modulated arc therapy by portal dosimetry*, Radiother Oncol, 2010, **94**(2), p. 181–87.
13. Bailey, D.W., Kumaraswamy, L., Bakhtiari, M., Malhotra, H. and Podgorsak, M.B., *EPID dosimetry for pretreatment quality assurance with two commercial systems*, J Appl Clin Med Phys, 2012, **13**(4), p. 82-99.

14. van Elmpt, W., Petit, S., Ruysscher, D.D., Lambin, P., and Dekker, A., *3D dose delivery verification using repeated cone-beam imaging and EPID dosimetry for stereotactic body radiotherapy of non-small cell lung cancer*, Radiother Oncol, 2010, **94**(2), p. 188-194.
15. Liu, B., Adamson, J., Rodriguez, A., Zhou, F., Yin, F.F., and Wu, Q., *A novel technique for VMAT QA with EPID in cine mode on a Varian TrueBeam linac*, Phys Med Biol, 2013, **58**(19), p. 6683-6700.
16. Podesta, M., Nijsten, S., Persoon, L., Scheib, S., Baltes, C., and Verhaegen, F., *Time dependent pre-treatment EPID dosimetry for standard and FFF VMAT*, Phys Med Biol, 2014, **59**(16), p. 4749-4768.
17. McCowan, P.M., Rickey, D., Rowshanfarzad, P., Greer, P.B., Ansbacher, W., and McCurdy, B.M., *Investigation of gantry angle data accuracy for cine-mode EPID images acquired during arc-IMRT*, J App Clin Med Phys, 2014, **15**(1), p. 1-15.
18. Adamson, J. and Wu, Q., *Independent verification of gantry angle for pre-treatment VMAT QA using EPID*, Phys Med Biol, 2012, **57**(20), p. 6587-6600.
19. Varian Medical Systems: On-Board imager® Advanced Imaging, Customer Release Note ver.1.5.18, 2011.
20. Ahnesjö, A., *Collapsed cone convolution of radiant energy for photon dose calculation in heterogeneous media*, Med Phys, 1989, **16**(4), p. 577-592.
21. Ansbacher, W., Swift, C-L., and Greer, P.B., *An evaluation of cine-mode 3D portal image dosimetry for Volumetric Modulated Arc Therapy*, J Phys: Conf Ser, 2012, **250**, p. 012022.
22. Woodruff, H.C., Fuangrod, T., Rowshanfarzad, P., McCurdy, B.M., Greer, P.B., *Gantry-angle resolved VMAT pretreatment verification using EPID image prediction*, Med Phys, 2013, **40**(8), p. 081715.
23. Podesta, M. *et al*., *Measured vs simulated portal images for low MU fields on three accelerator types: Possible consequences for 2D portal dosimetry*, Med Phys, 2012, **39**(12), p.7470-79.

CHAPTER SEVEN: SUMMARY AND CONCLUSIONS

7.1 SUMMARY

Implemented throughout the entire treatment course, *in vivo* patient dose verification represents an important addition that improves treatment quality and patient safety. Radiation treatments have become increasingly more complex with the development of volumetric modulated arc therapy (VMAT) and hypofractionated VMAT including stereotactic body radiation therapy (SBRT). Recently there has been increased clinical use of both VMAT and SBRT-VMAT. VMAT delivers highly conformal dose distributions to tumors, where delivery errors may negatively impact the patient dosimetry which in turn could decrease patient outcome. This impact is magnified for SBRT treatments due to their higher doses per fraction. Treatment plans are created using complex software and have been shown to be susceptible to technical or human errors[1-8], which can be dramatically reduced through the routine use of *in vivo* dosimetry.

Amorphous silicon (a-Si) electronic portal imaging devices (EPIDs) have been shown to be useful dosimetric devices while operated in both the integrated and continuous frame acquisition mode for both intensity modulated radiation therapy (IMRT) and VMAT. The continuous acquisition mode (cine-mode) of the EPID is required in order to measure the time dependant dose information of any treatment, including VMAT. Several groups have utilized the EPID for pre-treatment QA while only one other group has extensive experience

using the EPID for 3D *in vivo* dose verification (the Antoni van Leuenhoek Hospital, Amsterdam, Netherlands). Their approach uses a library of empirical correction data applied to back-projected EPID transmission images in order to reconstruct patient dose. In this thesis, previous work in the CancerCare Manitoba medical physics EPID research lab, where a model-based patient dose reconstruction method was developed, is improved on. Specifically, several technical challenges to large-scale clinical implementation were identified and overcome, some critical parameters were optimized, and the dose reconstruction methods were validated using an SBRT treatment beam. Although focused on *in vivo* application, the methods used here can be applied to both pre-treatment and *in vivo* calculations. The advantage of our model is its robustness via its derivation from the underlying physics of radiation transport, as opposed to purely empirical correction. This is analogous to the advantage of using model-based patient dose calculation algorithms (i.e., convolution/superposition), which are more accurate and robust compared to the previous generation of correction-based patient dose calculation methods (i.e. Batho correction).

The spatial position and orientation of the EPID is needed to ensure accurate geometric alignment of the acquired EPID images with isocentre and therefore with the patient model (i.e. CT data set). This knowledge is crucial in order to utilize the EPID images to accurately reconstruct the *in vivo* dose delivered to the patient. Two geometric effects were investigated: 1) the EPID 'sag', due to gravity, acting on the imager panel and its support-arm, and 2) the EPID image's associated gantry angle, which is recorded in the image's header file. The EPID sag was determined to be a negligible effect in the cross-plane direction (the axis perpendicular to the gantry's axis of rotation) and only exhibited a maximum displacement of

roughly 2 pixels (0.8 mm) in the EPID's in-plane direction (the axis parallel to the gantry's axis of rotation). This effect was characterized on several linacs and was determined to be reproducible and thus correctable. A simple trigonometric equation as a function of gantry angle was derived in order to correct each EPID image for this sag and was incorporated into our dose reconstruction algorithm.

Our *in vivo* dose reconstruction model requires the gantry angle of each EPID image as input. The reconstruction accuracy is directly dependent on the angular accuracy. Several methods were investigated that measured the EPID image's associated gantry angle. Initially, a valid and accurate source for gantry angle data was determined by comparing the linac's internal gantry potentiometer to angle data from an externally mounted high-precision incremental rotary encoder, and also a purpose-built gantry-angle phantom. The phantom was constructed in-house, and produced unique wire intersections in projection EPID images, whose location corresponded to an exact gantry angle. After validating an accurate gantry angle source, a comparison of these data to the angle data from treatment log files and also the EPID image header was performed. It was determined that the gantry angle recorded in the header of each EPID image could differ by as much as ±3° with respect to the true angle. Furthermore, it was determined that a simple box-smoothing of the header angle data (per arc) could be performed in order to reduce noise and adjust all EPID image angles to within ±1° of the true angle. This gantry angle correction step is now incorporated into our dose reconstruction algorithm and has improved χ-pass rates by as much as 5% in the high dose regions (voxels with $\geq$ 80% of the prescribed dose) when compared to the Eclipse dose calculation. The treatment log file data was even more accurate, but unfortunately accessing

it requires manual intervention and is far less convenient than accessing the EPID image header information.

The next section of the thesis discussed the modeling and validation of an EPID-based *in vivo* dose verification model specific to SBRT-VMAT deliveries, which uses a different photon beam compared to non-SBRT treatments. This was performed since SBRT delivers higher doses of radiation over fewer fractions compared to conventional VMAT and would therefore benefit immensely from a full-course dose verification system. Initial modeling was performed using the EGSnrc software package which simulated the dose delivered to a water phantom from various fields by a Varian 6 MV linac operated in SBRT mode. The simulated results were compared to depth-dose and profile measurements made in a water tank using small field diode detectors. The simulations were found to be in agreement with measurements to within 1%. These data provided us with a preliminary set of variables which were used in order to predict both focal and extra-focal fluences. Using our in-house optimizer, written in MATLAB, the SBRT-linac model variables (including focal and extra-focal fluence parameters) were optimized.

Validation of the patient dose reconstruction was carried out by delivering a variety of clinical SBRT-VMAT treatments, including two prostate, three lung, and two spine plans, to an anthropomorphic phantom. Our EPID-based 3D dose reconstruction was calculated using continuous-mode images acquired during beam-on and then compared to the 3D dose calculated by the Eclipse treatment planning software (TPS). Mean dose differences and 2% (dose difference)/2mm (distance-to-agreement) χ-tests were performed for low dose regions

(voxels receiving <80% and >20% of the prescribed dose) and high dose regions (voxels receiving >80% of the prescribed dose) for each plan. Overall, mean dose differences were within 3% in all dose regions for all plans. The χ-comparisons demonstrated a minimum 91% pass rate for the prostate plans, a minimum 88% pass rate for the lung plans, and a minimum 86% pass rate for the spine plans. Using the more conventional (i.e. clinically used) χ-test criteria of 3%/3mm, all pass-rates were better than 93% for all plans. The TG-119 AAPM report suggests that a greater than 90% pass-rate using a 3%/3mm criteria is clinically acceptable. Additionally, to explicitly demonstrate the *in vivo* application, on-treatment data were also acquired for a lung and spine patient (one fraction each). For these two plans, χ-comparisons with the TPS gave better than 86% for the lung and 95% for the spine using a 2%/2mm criteria. Using a 3%/3mm criteria better than 94.6% for the lung and 99.5% for the spine were achieved. Overall, the robustness of this model has been shown while demonstrating clinically acceptable accuracy using the conventional 3%/3mm tolerance.

The last section of this thesis investigated the optimization of EPID frame averaging for continuous-mode images acquired during VMAT delivery. This was performed in order to minimize calculation time of our reconstruction model and image storage requirements while maintaining a minimum required level of accuracy in the dose reconstruction. An unacceptable loss of accuracy was defined as no more than a ± 1% of the mean dose difference in the high dose region (voxels receiving >80% of the prescribed dose). Six VMAT and six SBRT-VMAT plans were delivered to an anthropomorphic phantom and acquired single frame EPID data using a specialized PC with a frame-grabber. For each delivered plan various scenarios of frame-averaged EPID data, in increments of 3 frames

(i.e., 3, 6, 9, etc.), were created. Each frame-averaged data set was used to calculate the *in vivo* dose to the patient and then compared to the single EPID frame *in vivo* dose calculation (the single frame calculation has no frame averaging and therefore has the highest possible angular resolution per EPID image). This type of comparison eliminated any dose algorithm differences between our model and Eclipse. Using a frame acquisition of 7.5 Hz, the optimized EPID frame averaging numbers were determined to be 9 and 11 for all VMAT and all SBRT-VMAT plans respectively. Optimization curves of the frame averaging number as a function of the average gantry speed of the linac, and also the prescribed dose per fraction were also developed. The methods reported can reduce the memory load on the treatment computer and also reduce the reconstruction model calculation time, without a significant loss in accuracy of the 3D patient reconstructed dose. These frame averaging optimization results have been successfully implemented into our clinical *in vivo* and pre-treatment patient EPID dosimetry program.

7.2 CONCLUSIONS

In this thesis an *in vivo* patient dose verification model for SBRT-VMAT using portal dose images was established. This involved characterizing and correcting two geometric errors: EPID imager 'sag' due to gravity, and EPID image angle inaccuracy. Improvements to our existing EPID-based VMAT reconstruction model were performed by creating and validating the model for SBRT-VMAT deliveries. Additionally, optimization of the EPID's frame averaging number, as a function of treatment type (dose per fraction and average

gantry speed), was performed in order to reduce dose reconstruction time while still maintaining a clinically acceptable level of accuracy (as well as avoiding treatment computer crashes). Overall, a robust model-based dose verification system for VMAT and SBRT-VMAT that performs with clinically acceptable accuracy was established. Routine clinical implementation of this dose verification method will be beneficial to both the quality of patient treatments and patient safety.

Presently, we now have an EPID-based, *in vivo* patient dose reconstruction model that can accurately calculate and predict IMRT, VMAT, and SBRT-VMAT dose distributions for patients on treatment. While the primary application of this model is *in-vivo* dose verification, it can also be utilized for pre-treatment patient specific QA, routine linear accelerator QA, and general 3D dosimetry applications. Furthermore, the model is not vendor-specific and can be implemented in any clinic, for any EPID-equipped linac, and for any linac energy.

7.3 FUTURE WORK

Presently our model is an offline algorithm whereby calculations are performed post-treatment. Our software package provides a full set of tools which can utilize the EPID for patient-specific pre-treatment QA, inter-fractional *in vivo* dose reconstruction, and general linac QA. The overall goal of this project is to implement our reconstruction software suite into a fully automated process for both the pre-treatment QA and *in vivo* calculations.

Automation is achievable via network access to the patient database environment. Using our EPID image prediction model, one could also incorporate the detection of real-time delivery errors. Furthermore, derivation of an approach to correct for inter-fractional changes in patient anatomy and alignment would also improve our *in vivo* results. All the above would establish a solid foundation for an adaptive radiotherapy program, which would ultimately provide improved treatment quality. These comments are expanded on in the following paragraphs.

The accuracy and robustness of our SBRT-VMAT dose verification model has been demonstrated. Recently, the model has been successfully implemented into the clinical testing stage for use as a patient-specific, pre-treatment QA tool. Current SBRT pre-treatment QA routines are cumbersome and time consuming in the clinic. Using our EPID-based 'inverse' model, the pre-treatment QA analysis requires only the acquisition of open-field (i.e. without an in-beam phantom or device) cine-mode EPID images, at an optimized frame average number, during delivery of the treatment plan. The EPID data can then be automatically retrieved and used to calculate a 3D patient dose. This is performed by back-projecting the EPID measured fluence to a plane above the patient's intended position (i.e., accounting for only the inverse square intensity drop-off), inserting the patient's planning CT downstream of this fluence, then forward calculating dose to it. This approach eliminates the use (and cost) of any external hardware and setup, the transfer of data from external devices, and any human errors such as phantom alignment errors.

Similar to the approach above, our *in vivo* dose reconstruction model can also be setup to run automatically for every fraction of every treatment course, simply by deploying and activating the EPID imager during treatment. Automation retrieves the EPID data, calculates dose, and emails a dose-per-fraction report and a cumulative dose report to the respective medical physicists and/or radiation oncologists. These may be used to determine whether the fraction or overall treatment was acceptable.

More recently, in conjunction with a collaborative research group located in Newcastle, Australia, a real-time error tracking software, based on our EPID image prediction model (as discussed in Chapter 2.2.4.*i*), has been developed for use with VMAT (and SBRT-VMAT) and IMRT deliveries. The system software is operated via a separate PC with a designated frame-grabber which can acquire single EPID frames continuously. The system can operate during beam-on and compare, in near real-time, predicted and measured EPID images in order to determine, if any, MLC aperture and/or dose delivery errors. A user-friendly live graphical readout displays the comparisons and flags any errors greater than a pre-determined tolerance. This would allow the radiation therapists to stop any treatment that is not within the defined delivery tolerances. Although in testing stages, this system would be beneficial for improved patient safety.

One limitation of our current dose reconstruction model is that each fraction's *in vivo* 3D dose is calculated using the patient's planning CT, which is acquired roughly two weeks prior to treatment. During the course of a treatment (2 to 8 weeks) anatomical changes to the tumor and/or healthy tissue can produce a substantial change in the dosimetry of the patient.

Furthermore, patient set up errors such as pitches, rolls, yaws, and translations, can all lead to additional dosimetric errors.

Recently, it has become common practice to use cone-beam CTs (CBCTs) to align the patient to their planned position prior to treatment. CBCT is a technique utilizing a continuous arc of kV x-rays delivered (in a cone geometry) through the patient and measured by an imaging panel downstream of the patient. It reconstructs the 3D patient anatomy (i.e., density) with less accuracy than a conventional CT due large amounts of patient scatter. In general, the CBCT anatomy is registered to the planning CT, via software, and any corrections to patient positioning are performed prior to the start of treatment.

It would be useful to use the CBCT data set for dose calculation, however, due to the presence of patient scatter, the conversion of CBCT data to patient density is problematic and does not allow for an accurate dose calculation. This shortcoming may be partially addressed through the use of deformable registration algorithms. A deformable registration 'deforms' the planning CT density data and re-maps it onto the CBCT data set via any one of numerous matching techniques (anatomies, intensities, etc.). In general, it maps the Hounsfield units of the planning CT onto the deformed matched anatomy of the CBCT. The deformed CT data, which is a more accurate representation of the current patient anatomy during that fraction delivery, could then be used for an *in vivo* dose calculation as opposed to the planning CT. The resulting estimate of patient dosimetry would be more accurate using this approach, especially if large changes in anatomy or alignment offsets had occurred. This would be a crucial step towards an adaptive radiotherapy program.

Simple and automated pre-treatment VMAT QA, routine *in vivo* patient 3D dosimetry for all treatment fractions, real-time error detection, and adaptive radiotherapy using patient dosimetry estimates are all exciting applications that build on the work of this thesis. The work in this thesis provides a foundation for these and other exciting research avenues.

REFERENCES

1. Valentin, J., *Case histories of major accidental exposures in radiotherapy*, Annals of the ICRP, 2000, **30**, p.23-29.
2. Leveson, N.G., Turner, C.S., *An investigation of the Therac-25 accidents*, IEEE Computer, 1993, **26**, p.18-41.
3. "El accidente del Clínico de Zaragoza, una cadena de fallos humanos única en el mundo, según los expertos". El País (in Spanish). October 12, 1991. Archived from the original on October 10, 2012.
4. *Accidental Overexposure of Radiotherapy Patients in Bialystok*, International Atomic Energy Agency: Vienna. 2004.
5. Bogdanich, W., *Radiation Offers New Cures, and Ways to Do Harm*, The New York Times, January 23, 2010,
6. Borius, P.Y., Debono, B., Latorzeff, I., *et al*. *Dosimetric stereotactic radiosurgical accident: Study of 33 patients treated for brain metastases*, Neurochirurgie, 2010, **56**, p.368-373.
7. Derreumaux, S., Etard, C., Huet, I.C., *et al*. *Lessons from recent accidents in radiation therapy in France*, Rad. Prot. Dosim., 2010, **131**, p.130-135.
8. Gourmelona, P., Bey, E., De Revel, T., *et al*. *The French radiation accident experience: emerging concepts in radiation burn and ARS therapies and in brain radiopathology. Radioprotection*, 2008, **43**, p.23-26.

CHAPTER EIGHT: APPENDIX

8.0.1

The following section describes the basic principles and physics involved in the production and interactions of therapeutic x-rays. This section was documented and presented during my candidacy exam.

8.1 THE PHYSICS OF THERAPEUTIC X-RAYS

8.1.1 X-ray production

When a photon interacts with an atom (or molecule) and has enough kinetic energy to liberate an electron from that atom it is called an *ionizing* photon or x-ray. An x-ray is most commonly produced by either a characteristic transition or through a Coulomb interaction. A characteristic transition occurs when electron vacancies in the lower shells (lower energy) of an atom get filled by electrons from higher shells (higher energy). A characteristic x-ray is emitted in this process and has an energy equal to the energy difference between the two shells. Bremsstrahlung x-rays are the by-products of inelastic Coulomb collisions between charged particles and the nuclei of atoms. We will focus our discussion on bremsstrahlung x-rays generated for therapeutic applications. The charged particle of interest for our discussion is the electron.

Bremsstrahlung radiation (or 'braking' radiation) is produced when an electron (or positron) decelerates during an inelastic collision with an absorbing nucleus's Coulomb field. During this change in velocity a fraction of the kinetic energy (KE) of the electron is lost and emitted as an x-ray. This can be as large as the initial KE of the electron or very small, i.e., a 6 MV electron beam bombarding a tungsten target produces a continuous x-ray spectrum in the range of 0-6 MeV (see Fig. 8.1). In general, the average x-ray energy of a continuous bremsstrahlung spectrum is roughly one third of the maximum electron kinetic energy.

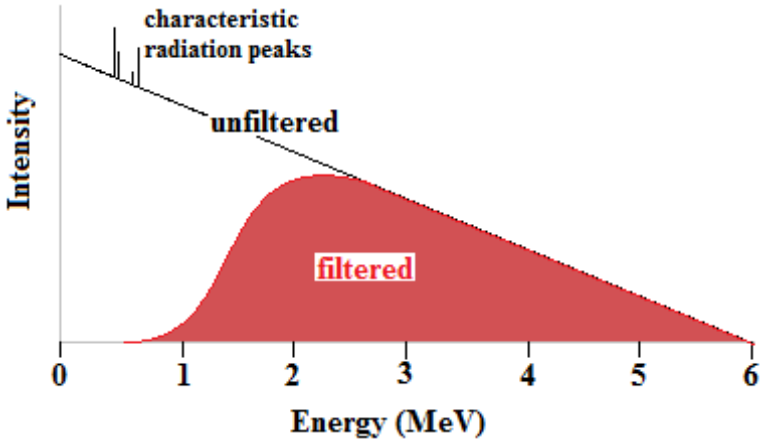

Fig. 8.1 [Bremsstrahlung Spectrum]: A typical 6MeV filtered (red) and unfiltered (black) bremsstrahlung spectrum produced by a linac. The linac's flattening filter and tungsten target produce the filtering.

The intensity (or energy flux) of an electromagnetic field is given by the cross product of the electric field vector, ***E***, and magnetic field vector, ***B***, of the accelerated charges (electrons in our case) and is known as its Poynting vector ***I***.

$$I = \frac{1}{\mu_o} E \times B \qquad [8.1]$$

Since ***E*** and ***B*** are perpendicular to each other, the magnitude of ***I*** is given by:

$$I = |I| = \frac{1}{\mu_o} EB = \frac{\varepsilon_o k^2 a^2 e^2}{c^3 r^2} sin^2\theta \qquad [8.2]$$

where k is Coulomb's electric constant, e is the charge of the electron, a is its acceleration, and r is the distance from the photon production to an observation point, c is the speed of light, and ε_o is the permittivity of free space. From Eq. 8.2 we see that the intensity of the emitted radiation is inversely proportional to r^2, and is maximized at right angles ($\theta_{max} = \pi/2$) to the direction of motion. The angle θ is measured with respect to the velocity vector of the electron just before the collision. By integrating the Poynting vector over the area we find that the power P emitted by the accelerated electron in the form of bremsstrahlung radiation is also proportional to a^2 and e^2. When equating Newton's force with the Coulomb force one finds that the acceleration of the electron is proportional to its charge e and the charge of the target nuclei Ze.

$$F_{net} = m_e a = \frac{Ze^2}{4\pi\varepsilon_o r^2} \qquad [8.3]$$

Furthermore, the acceleration is inversely proportional to the mass of the charged particle. Thus the power of the bremsstrahlung radiation produced is inversely proportional to the square of the mass of the decelerating particle. This is why electrons or positrons are ideal for bremsstrahlung radiation production as opposed to the much heavier protons.

For relativistic speeds, comparable to that of a medical linac, the magnitude of the radiation intensity becomes more forward peaked (i.e. θ_{max} decreases) due to a change in the angular dependence of Eq. 8.2

$$I_{rel} = \frac{\varepsilon_o k^2 a^2 e^2}{c^3 r^2} \frac{sin^2\theta}{(1-\beta cos\theta)^5} \quad [8.4]$$

where β is the ratio of the speed of the electron to the speed of light and is defined as

$$\beta = \frac{v}{c} = [1 - \left(1 + \frac{E_K}{m_e c^2}\right)^{-2}]^{1/2} \quad [8.5]$$

and E_K is the kinetic energy of the electron and m_e is its mass. The $m_e c^2$ term is the rest-mass energy of the electron and is equal to 0.511 MeV. As the acceleration of the electron is increased so is the resulting radiation intensity at θ_{max}. For example, a 6 MeV electron (with a speed of 0.997c) has a θ_{max} equal to 2.3° and roughly 10^5 times more intensity than a 1 MeV electron (v = 0.941c) with a θ_{max} = 10°.

When an electron collides with a target atom, the energy transfer varies depending on how far away the incident electron is from the target atom. Collisional losses, in general, refer to electron-electron collisions ejecting valence electrons in the absorber producing ionization or excitation. Radiation losses refer primarily to bremsstrahlung production. Collisions can be either 'hard' (when the incident electron is within the radius of the target atom), or soft (when the incident electron is far outside the radius of the target atom). Soft collisions account for roughly 50% of the electron's total energy loss into the medium.

The energy lost by the electron depends on characteristics of both the target atom and the incident electron. The rate of energy loss per unit length a charged particle experiences in an absorbing medium is called the linear stopping power. The linear stopping power divided by the density of the absorber is called the total mass stopping power, S_{tot}. The total mass stopping power of an absorber is the sum of the mass collision stopping power, S_{col}, and the mass radiation stopping power, S_{rad}.

$$S_{tot} = S_{col} + S_{rad} \quad [8.6]$$

The radiation stopping power is given as the product of the cross section (probability of emission per cross-sectional area) for the emission of bremsstrahlung radiation σ_{rad}, atomic density N_a (Avogadro's number/atomic mass number, N_A/A), and the initial total energy of the electron, E_i:

$$S_{rad} = N_a \sigma_{rad} E_i \quad [8.7]$$

The cross section is proportional to the square of the atomic number of the absorbing nucleus *Z*. The total energy E_i is a sum of the electron's rest mass and initial kinetic energy. Combining Eq. 8.7 with the well-established Bethe and Heitler result[1] for σ_{rad} gives

$$S_{rad} = \alpha r_e^2 Z^2 \frac{N_A}{A} E_i B_{rad} \quad [8.8]$$

Where α is the fine structure constant (1/137), r_e is the classical electron radius (~2.8 fm), and B_{rad} is a slowly varying function of Z and E_i.

For most stable elements $Z/A \approx 0.5$ and approaches 0.4 for more dense elements like tungsten. Therefore, the radiation stopping power is roughly a function of the absorber's Z, and the larger the Z the greater the radiation yield. The radiation yield, which defines the fraction of initial kinetic energy emitted as radiation, will increase with higher atomic number absorbers and with higher initial kinetic energies of the electron.

Collision stopping power does not depend heavily on Z. It is also remains fairly constant for varying absorber density at relativistic energies (>1 MV). Collision stopping power for electrons and positrons is given as

$$S_{col} = 2\pi r_e^2 \frac{Z}{A} N_A \frac{m_e c^2}{\beta^2}\left[ln\frac{E_K}{I_e} + ln\left(1 + \frac{E_K}{2m_e c^2}\right) + F^{\pm} - \delta\right] \qquad [8.9]$$

where $F^{\pm}$ is a function of E_K, which differs for electrons and positrons, and I_e is the mean ionization/excitation potential of the absorber. Collisions can generate a substantial amount of heat in the medium which may require cooling, depending on the initial energies of the electrons and the application.

When choosing a suitable target material for a medical linac one must account for both the collision and radiation stopping power properties of the absorbing material. Tungsten is a popular choice for linacs due to its high atomic number and thus higher bremsstrahlung

radiation yield for relativistic electron energies. In most cases a layer of copper is attached to the base of the tungsten target in order to help conduct heat away to a water cooling system.

8.1.2 X-ray interaction

Now that we have described how one can produce x-rays we want to look at the physical models characterising x-ray interactions with matter. Similar to the electron interactions discussed previously, x-ray photons can interact with the absorber's nuclei, or their orbital electrons. After the collision the photon is either scattered or absorbed. It can also impart some or all of its energy to an electron and scatter or excite it.

The probability of a particular interaction occurring will depend on the incident photon's energy and atomic number of the absorber. Interactions with the nuclei most commonly involve a photon interacting with the electrostatic field of the nucleus, called pair-production. Another possibility includes a direct high energy gamma ray-to-nucleus interaction, called photodisintegration. However, the high energy requirement of the gamma rays needed for a photodisintegration (~20 MeV) makes this a negligible consideration for routine radiotherapy. Interactions with loosely bound orbital electrons result in the Compton Effect, triplet production, or Thomson scattering. Interactions with tightly bound orbital electrons result in either the photoelectric effect or Rayleigh scattering. A loosely bound electron is defined as having a binding energy E_B much less than the photons energy hv (i.e., $E_B << hv$). A tightly bound electron has a binding energy comparable to the photons energy (i.e., $E_B \approx hv$). The electron binding energy is the energy required to liberate an electron from the atom's electromagnetic field. If an electron or positron is released or produced by any type of

photon interaction, they either deposit their energy in the medium through Coulomb interactions (collision and ionization losses), S_{col}, or can produce secondary bremsstrahlung photons by radiation loss, S_{rad}. These were discussed in the previous section.

The linear attenuation coefficient μ is an important parameter when characterizing photon interactions with a medium. It is a function of both the energy of the photon, *hv*, as well as the atomic number of the absorber, *Z*. It is defined as the probability per unit path length that a photon will interact with an atom within the absorber. The fractional reduction in intensity, $-dI/I$, is proportional to the distance travelled, dx. The proportionality constant is the attenuation coefficient. The intensity at any point within a homogeneous medium is

$$I_N(x) = I_o e^{-ux} \qquad [8.10]$$

while the intensity at any point within a heterogeneous medium is

$$I_N(x) = I_o e^{-\int_0^x \mu dx} \qquad [8.11]$$

where I_o is the initial beam intensity, dx is the absorber thickness, and $I_N(x)$ is the attenuated intensity. These equations are derived for narrow monoenergetic beam geometry, i.e., no scatter or secondary photons are generated in the absorber. In order to account for broader beam geometries a measured buildup factor B is introduced into Eq. 8.10 and 8.11 because secondary photons created in the absorber will increase the exiting intensity, i.e., $I_B(x) = B \cdot I_N(x)$.

The mass attenuation coefficient is μ divided by the density of the absorber ρ. It defines the probability within an area per unit mass that a photon will interact with an absorbing medium. The atomic cross section is μ divided by the number of atoms per volume of the absorber (N_a/V). It defines the probability that a photon will interact with an atom, i.e., the nucleus and/or a tightly bound electron. The electronic cross section is defined as μ divided by the number of electrons per volume of the absorber ($\rho Z N_a/A$). It defines the probability that a photon will interact with an electron (considered free or loosely bound). The terms are conventionally symbolised by μ_ρ, ${}_a\sigma$, and ${}_e\sigma$ respectively. In the following sections we will briefly discuss relevant photon interactions at therapeutic energies.

8.1.2.i Incoherent scattering (Compton Effect)

The Compton Effect involves the elastic collision of a photon and an orbital electron. The photon imparts a fraction of its energy to an orbital electron, which is ejected from the atom with a kinetic energy E_K, and the outgoing scattered photon has a reduced energy. A schematic of the collision and parameters is given in Fig. 8.2.

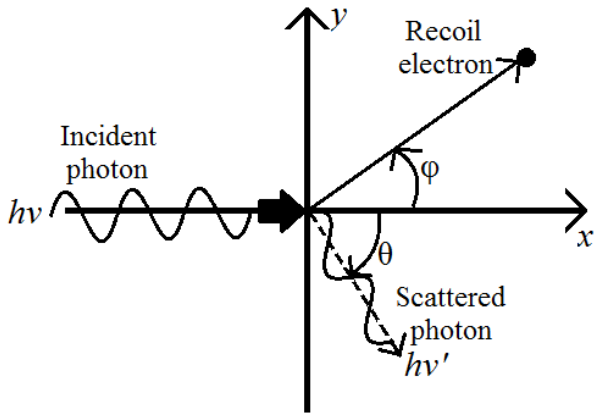

Fig. 8.2 [Compton Scatter Diagram]: A diagram of the Compton Effect for an incident photon of energy *hv*.

$h\nu$ is the initial photon energy, $h\nu'$ is the scattered photon energy, θ is the angle of the scattered photon with respect to the direction of the incident photon, and φ is the recoil angle of the ejected electron.

The energy of the scattered photon is determined by the relativistic Compton wavelength shift equation

$$\Delta\lambda = \lambda' - \lambda = \lambda_c(1 - cos\theta) \qquad [8.12]$$

Where λ' is the scattered photon wavelength and λ_c is the Compton wavelength equal to $h/m_e c$. Eq. 8.12 is derived using the conservation of relativistic energy and momentum and assuming a free electron target. The kinetic energy acquired by the electron is equal to the energy difference between the incident photon and scattered photon. The energy of the scattered photon is greater for smaller values of θ. Using the wave equation, $c = \lambda\nu$ we can also rewrite Eq. 8.12 in terms of photon energies:

$$h\nu' = \frac{h\nu}{1+\varepsilon(1-cos\theta)} \qquad [8.13]$$

where ε is the photon energy normalized to the electron rest mass energy ($h\nu/m_e c^2$). The scattering angle θ can have values between 0 and π. For the special case where $\theta = \pi/2$ (i.e. 90° scatter) and $h\nu$ approaches infinity we find that $h\nu'$ approaches a maximum value of 0.511 MeV (the rest-mass energy of the electron). This is an important finding when considering shielding construction for linac vaults. If $\theta = \pi$ (i.e. perfect backscatter) as $h\nu$

approaches infinity we find that no matter how energetic the incident photon is, the scattered photon can only have a maximum energy of 0.255 MeV.

The probability that a photon will interact with a free electron is derived from the differential Klein-Nishina electronic cross section per unit solid angle[2]

$$\frac{d_e\sigma_c^{KN}}{d\Omega} = \frac{r_e^2}{2}(1 + cos^2\theta) \cdot F_{KN} \qquad [8.14]$$

where r_e is the classical radius of the electron and F_{KN} is the Klein-Nishina form factor which is a complex function of incident photon energy and scatter angle θ. The range of F_{KN} is between 0 and 1. It is only equal to one when $\theta = 0$, for any $h\nu$. When $h\nu = 0$, at any value of θ, this is termed Thomson scattering. For larger photon energies, the value of F_{KN} becomes smaller. As scattering angle increases for all photon energies, the value of F_{KN} decreases.

For low incident photon energies the probability for forward scattering and backscattering are equal and twice as much as for side scattering ($\theta = \pi/2$). As $h\nu$ increases the scattering becomes more forward peaked with less backscattering.

By integrating Eq. 8.14 over the whole solid angle dΩ we can define the Klein-Nishina Compton cross section ${}_e\sigma_c^{KN}$. This is a complex function of the incident photon energy $h\nu$ only. We will look at two extreme cases: when $h\nu << m_ec^2$ the cross section approaches the classical Thomson scattering result of ${}_e\sigma_c^{KN} \rightarrow {}_e\sigma_T = \frac{8\pi}{3}r_e^2$. For very large photon energies, $\varepsilon >> 1$, the electronic cross section can be approximated by using the following equation

$$_{e}\sigma_{c}^{KN} \approx \pi r_{e}^{2} \frac{ln(2\varepsilon)+1}{2\varepsilon} \quad [8.15]$$

It is important to note that this derivation of the electronic cross section for Compton scattering is *independent* of the atomic number *Z* of the absorber because the electron is considered to be free. Although the binding energy is neglected in the derivations of Eq. 8.14 and 8.15 the results are still very accurate for photon energies above 0.3 MeV for absorbers ranging from hydrogen up to lead. For lower energies, additional corrections are needed. The mass attenuation coefficient for the Compton Effect can be calculated by:

$$\frac{\mu_c}{\rho} = \frac{ZN_A}{A} {}_{e}\sigma_{c}^{KN} \approx \frac{N_A}{2} {}_{e}\sigma_{c}^{KN} \quad [8.16]$$

Therefore using Eq. 8.15 and 8.16 we can approximate the Compton mass attenuation coefficient for high energy photons typical of a medical linac.

8.1.2.ii Rayleigh scattering

Rayleigh scattering is the elastic collision of a photon with a tightly bound atomic orbital electron. The atom is neither excited nor ionized and because the electron is tightly bound the atom as a whole absorbs the transferred momentum and its recoil energy is very small. The scattering angles of the photon are small and so is the transferred energy, so that the scattered photon has essentially the same energy as the incident photon. This effect is more probable at very low photon energies (< 10 KeV) and for high *Z* absorbers. The Rayleigh differential atomic cross section per solid angle is similar to Eq. 8.14 except that the F_{KN} form factor is

replaced by a squared dependence of the Rayleigh atomic form factor, which is a complex function of *x*, the *momentum transfer variable* defined as $sin(\theta/2)/\lambda$, and atomic number *Z*. For small scattering angles it is equal to *Z* and it approaches zero for large scattering angles. The higher the incident photon energy, the more forward peaked the photon scattering angle. For photon energies equal to 1 MeV the maximum scatter angle of Rayleigh scattered photons is only 7° for lead and 3° for carbon. These decrease further with increasing photon energy. The scattering angles become broader when lower *hv* energies interact with high *Z* absorbers.

The Rayleigh atomic cross section is proportional to $Z^2/(hv)^2$. Converting to the mass attenuation coefficient we find that $\frac{\mu_R}{\rho} \propto Z/(hv)^2$. Rayleigh scattering is not important for radiation dosimetry as no energy is transferred from the photon to the electron and can be considered negligible for MV radiotherapy. Rayleigh scattering is more predominant than Compton scattering at very low photon energies (< 0.1 MeV for high *Z* absorbers and < 0.01 MeV for low *Z* absorbers). However, both probabilities are considered negligible when compared to the photoelectric effect at low photon energies.

8.1.2.iii Photoelectric Effect

The photoelectric effect involves the collision of a photon and a tightly bound electron. The photon is completely absorbed and the electron is ejected with kinetic energy E_K. For this to occur, the photon energy must be equal to or greater than the binding energy E_B of the electron, i.e., $hv > E_B$. The kinetic energy imparted to the *photoelectron* is then the difference of these two energies, $E_K = hv - E_B$. The scattering angle of the photoelectron decreases with

increasing photon energy. The photon energy may not be enough to liberate the electron but just raise it to a higher energy (shell) causing an excitation of the atom. Either by excitation or ionization the atom will fill the vacancy by emitting a characteristic x-ray or an Auger electron. An Auger electron is a low energy electron sometimes emitted when higher shell electrons fill lower shell vacancies. The Auger electrons will have kinetic energies equal to the differences in their respective binding energies.

The atomic cross section for the photoelectric effect is proportional to roughly Z^5 for relativistic photons and as low as Z^4 for low energy photons. For relativistic photons, relevant to MV radiotherapy, the atomic cross section is given as:

$$ {}_{a}\sigma_{PE} = \frac{1.5}{\varepsilon}\alpha^4 Z^5 ({}_{e}\sigma_T) \qquad [8.17] $$

Plotting ${}_{a}\sigma_{PE}$ as a function of $h\nu$, 'saw-tooth-like' discontinuities can be seen and are due to absorption edges. These arise when photon energies are the same as the binding energies of specific electron shells. As the photon energy increases and approaches a specific binding energy, the cross section decreases until the binding energy is exceeded in which case more photoelectric interactions are possible and the cross section quickly jumps. The energy dependence of the cross section is approximated as $1/(h\nu)^3$ for low photon energies and $1/h\nu$ for high photon energies.

It is dosimetrically important to approximate the mean energy transferred to photoelectrons from a photoelectric event because a fraction or all of this energy will be deposited as dose in the medium. The mean energy transfer $\bar{E}_{tr}^{PE}$ is defined as

$$\bar{E}_{tr}^{PE} = h\nu - \bar{X}_{PE} \qquad [8.18]$$

where $\bar{X}_{PE}$ is the mean fluorescence emissions energy for a given *j*-shell vacancy and defined as the product of the specific shell's binding energy $E_B(j)$, fluorescence efficiency η_j, fluorescence yield ω_j, and probability of photoelectric effect P_j summed over all *j*-shells. The probability of a *j*-shell photoelectric effect is a function of the photoelectric mass attenuation coefficient, $\frac{\mu_{PE}}{\rho} = \frac{N_A}{A}\,{}_a\sigma_{PE}$. The fluorescence yield is the probability of characteristic x-ray emission. The Auger electron emission probability would then be equal to (1 - ω_j). Values for the above variables are well documented in the literature.

8.1.2.iv Pair Production

Pair production can only occur when a photon incident on an absorber atom has an energy greater than twice the rest-mass energy of an electron, i.e., $h\nu \geq 2m_e c^2$. Energy, charge, and momentum must all be conserved for this effect to occur. In order to conserve momentum simultaneously with energy and charge, pair production can only occur in the Coulomb field of the atomic nucleus or orbital electron which can absorb a fraction of the photon's momentum. When the extra momentum is absorbed by the nucleus an electron and positron are ejected from the atom. Because of the large mass of the absorbing nucleus the recoil energy is negligible. Charge is then conserved for pair production. When an orbital

electron absorbs the extra momentum the recoil energy may be large enough to eject it from the atom along with the electron and positron in a process called triplet production. This ionizes or excites the absorber atom. It then refills the shell vacancy using the processes described in the previous section.

The threshold energies for both pair and triplet production can be found by utilizing the relativistic invariant $E^2 - p^2c^2$. The initial and final state of the invariant is equal because the total rest mass of all objects involved is conserved. Furthermore, the final momentum for both cases can be considered negligible when using the centre-of-mass coordinate system after the collision because the atom's recoil is very small. Equating the invariant gives the pair production threshold E_{thr}^{PP} and triplet production threshold E_{thr}^{TP} to be

$$E_{thr}^{PP} = 2m_e c^2 \left(1 + \frac{m_e c^2}{m_A c^2}\right) \quad [8.19]$$

$$E_{thr}^{TP} = 4m_e c^2 \quad [8.20]$$

where $m_A c^2$ is the rest mass of the atom. The first term in the brackets of Eq. 8.19 represents the energy of the electron and positron pair. The second bracketed term is the smaller nuclear recoil term $\frac{2(m_e c^2)^2}{m_A c^2}$ which is needed in order to conserve momentum. The large difference in mass ($m_e << m_A$) makes this term very small. Comparatively, the threshold energy for triplet production is 4 times the rest-mass energy of the electron. $2m_e c^2$ is allotted to the electron positron pair and the remaining $2m_e c^2$ is divided equally to both electrons and the positron in the form of kinetic energy. Any energy above these threshold values would be converted

to extra kinetic energy for the recoiled particles. In other words the total kinetic energy imparted to the pair or triplet particles would be $E_K = hv - 2m_e c^2$. This energy is not necessarily shared equally by all the recoiled light charged particles. As with Rayleigh and Compton scattering, the higher the photon energy the more forward peaked the angular distribution of electrons and positrons.

The derivation of the atomic cross section for pair production is complicated and can be attained using several different approximations[3]. In general it has the form

$$_{a}\sigma_{PP} = \alpha r_e^2 Z^2 P(\varepsilon, Z) \qquad [8.21]$$

where $P(\varepsilon,Z)$ is a complex function of photon energy and absorber atomic number. In general, the atomic cross section for pair production is proportional to Z^2 and linearly proportional to Z for triplet production. The mass attenuation coefficient for pair production is found by multiplying Eq. 8.21 by N_A/A. Using the approximation of $Z/A \approx 0.5$, the mass attenuation coefficient for pair production is linearly proportional to Z and approximately independent of Z for triplet production.

When a positron and electron interact together at rest they annihilate themselves and create two photons of 0.511 MeV each. Theses photons travel away at nearly 180° from each other. An ‘in-flight’ positron, with a non-zero kinetic energy, can also annihilate a tightly bound or free orbital electron. This occurs very rarely with respect to “at rest” annihilations. For a tightly bound electron the atom (nucleus more so) absorbs the recoil momentum and

the annihilation produces only one photon with an energy equal to the total positron energy and the rest-mass energy of the orbital electron. The in-flight annihilation with a free electron creates two photons of varying energy and scatter angles depending on the impact parameters of a two-body elastic collision. The total energy and momentum of in-flight annihilations are conserved.

8.1.3. Photon-Energy Transfer to and Energy Absorption in Matter

Since the attenuation coefficient for a photon is the probability it will undergo some sort of interaction, it can be written as the sum of all the attenuation coefficients we have discussed in the previous section.

$$\frac{1}{\rho}\mu = \frac{1}{\rho}(\mu_{PE} + \mu_R + \mu_C + \mu_{PP}) \qquad [8.22]$$

Similar equations can be determined for the atomic and electron cross sections.

The photoelectric effect is the predominant interaction mode with an absorber at low photon energies. At intermediate photon energies and low Z absorber, the Compton Effect predominates. For water and tissue Compton scattering is the most probable interaction in the range of 0.1 to 20 MeV and is thus the most important interaction of photon beams used for radiotherapy. Pair production dominates for higher energy photons greater than 20 MeV. Rayleigh scattering plays a minimal role in comparison with the other three interactions, except at very low energies.

8.1.3.i Energy transfer

The energy transfer fraction is defined as the fraction of energy that is transferred to a light charged particle(s), either liberated or produced in the absorber, in the form of kinetic energy from various forms of photon interaction, $f_{tr} = E_K/h\nu$. The mean energy transfer fraction is the ratio of the mean energy transferred to the electron divided by the initial photon energy. The total mean energy transfer fraction is the sum of all the individual mean energy transfer fractions multiplied by their probability of attenuation and divided by the total probability of attenuation.

$$\bar{f}_{tr} = \frac{1}{\mu}\left(\mu_{PE}\bar{f}_{PE} + \mu_R\bar{f}_R + \mu_C\bar{f}_C + \mu_{PP}\bar{f}_{PP}\right) \qquad [8.23]$$

As discussed in Section 8.1.2.*ii* there is no energy transfer for Rayleigh scattering, i.e., $\bar{f}_R = 0$. Compton, photoelectric, and triplet production interactions produce electron vacancies in the atoms of the absorber creating a cascade of characteristic photons and/or Auger electrons. Each interaction's mean energy transfer function has the form $E_{tr} = h\nu - \bar{X}$, where $\bar{X}$ is the mean fluorescence emission energy. All three mean energy transfer fractions increase with increasing $h\nu$ (not including the discontinuities of the photoelectric effect), and converge to 1 for large photon energies. Pair production and Compton mean energy transfer fractions have no dependence on the atomic number Z of the absorber but the photoelectric mean energy transfer fraction does.

The Compton Effect dominates for intermediate photon energies and low Z absorbers but is less dominate for higher Z absorbers. For therapeutic energies the Compton Effect has the

highest probability of transferring energy to electrons in a low *Z* absorber. The photoelectric effect clearly dominates the energy transfer at lower photon energies while pair production dominates at higher photon energies. The photoelectric effect is the most dominant for $h\nu \leq$ 50 keV, the Compton effect for 60 keV $\leq h\nu \leq$ 20 MeV and pair production for $h\nu \geq$ 30 MeV for a carbon absorber ($\rho \sim 2.2$ g/cm^3). These effects are comparable for tissue, bone, and fat which have effective densities around 1.1, 1.7, and 0.9 g/cm^3 respectively.

To determine the mean energy transferred one simply multiplies both sides of Eq. 8.23 by the photon energy *hν*. In general, the mean energy transferred to electrons increases with increasing photon energy.

8.1.3.ii Energy absorption

The mean energy absorbed is equal to the difference between the mean energy transferred $\bar{E}_{tr}$ and the mean energy radiated from light charged particles produced by photon interactions $\bar{E}_{rad}$

$$\bar{E}_{ab} = \bar{E}_{tr} - \bar{E}_{rad} \qquad [8.24]$$

This is sometimes written in the following form

$$\bar{E}_{ab} = \bar{E}_{tr}\left(1 - \frac{\bar{E}_{rad}}{\bar{E}_{tr}}\right) = \bar{E}_{tr}(1 - \bar{g}) \qquad [8.25]$$

where $\bar{g}$ is the mean radiation fraction. As discussed earlier, the *radiation* processes that secondary electrons lose their energy are: bremsstrahlung interactions, in-flight annihilations, and characteristic ionizations or excitations. Therefore the mean radiation fraction can be written as a sum of the mean radiation fractions for the individual interactions. The mean characteristic ionization fraction is generally neglected in comparison to the bremsstrahlung fraction which is the predominant radiation-emitting interaction.

For a given photon energy, the mean radiation fraction increases with atomic number of the absorber. For a given atomic number of the absorber $\bar{g}$ also increases with photon energy. The mean bremsstrahlung radiation fraction is the only contributor to $\bar{g}$ for photon energies below $2m_e c^2$, which is the threshold energy for pair production (i.e., positron production). At energies above $2m_e c^2$ the mean radiation fraction is still dominated by the mean bremsstrahlung fraction. At lower photon energies, below 1 MeV for low Z absorbers and below 200 keV for high Z absorbers, $\bar{g} \approx 0$. For larger photon energies $\bar{g}$ increases and $\bar{E}_{ab}$ starts to diverge from $\bar{E}_{tr}$. For a low Z absorber like carbon this divergence is not significant until photon energies are greater than 20 MeV. Lead on the other hand shows significant divergence above 2 MeV. Therefore, if a 6 MV x-ray beam is delivered to human tissue the mean energy absorbed will be approximately equal to the mean energy transferred.

8.2 DOSE IMAGE COMPARISON TECHNIQUES

Before the implementation of highly modulated radiation therapy treatments, a simple percentage difference was used for direct comparison between two independently acquired and/or predicted images. This was sufficient for earlier therapy treatments because the only steep dose gradient zones were the edge of the field in the penumbra area.

Once IMRT was implemented the percentage dose difference was no longer able to characterize the subtle high dose-gradient regions due to MLC modulation. Van Dyk *et al*., proposed a separated approach for dose distribution comparison by defining a lower dose-gradient region (less than 30%/cm), to be analyzed with a conventional percentage difference approach, and a high dose-gradient region (greater than 30%/cm), which would have a defined maximum distance to agreement (DTA) estimate between points[4].

Low *et al*., later defined a combined DTA and percentage difference metric called the γ-evaluation[5]. The theory utilizes a 3D ellipsoid of Cartesian dimensions *x*, y, and *dose* centered on a reference dose, D_r, and reference distance, d_r, (see Fig. 8.3).

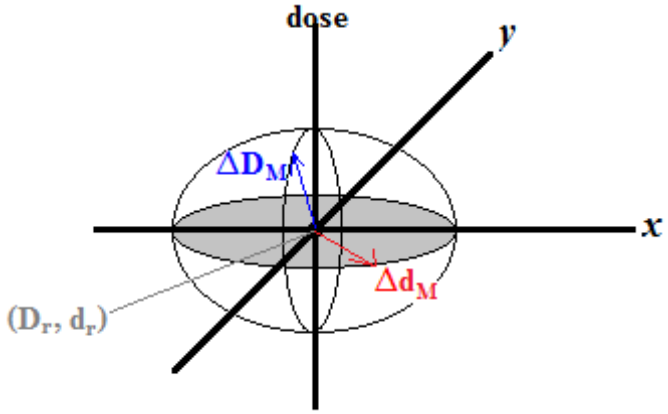

Fig. 8.3 [Gamma-test Geometry]: Low *et al.*, γ-evaluation ellipsoid variables

It has the mathematical form:

$$1 = \sqrt{\frac{\Delta d^2}{\Delta d_M^2} + \frac{\Delta D^2}{\Delta D_M^2}} \qquad [8.26]$$

where ΔD_M is the maximum dose difference and Δd_M is the maximum DTA, Δd is the distance from reference point to comparison point, i.e., $\Delta d = |d_c - d_r|$, and ΔD is the dose difference between the reference and comparison point, i.e., $\Delta D = D_c - D_r$. Each voxel in a 3D dose matrix is evaluated to see if it falls within the defined "acceptance ellipsoid" defined as:

$$\Gamma(d_c, D_c) \equiv \sqrt{\frac{\Delta d^2}{\Delta d_M^2} + \frac{\Delta D^2}{\Delta D_M^2}} \leq 1, \text{ and } \quad \gamma = min[\Gamma(d_c, D_c)] \qquad [8.27]$$

The comparison point agrees with the reference point if γ is less than 1 within the selected criterion of Δd_M and ΔD_M.

The γ-evaluation is very time consuming because it must compare every reference point and every comparison point. Bakai *et al.* introduced a computationally efficient approach called a χ-comparison which is nearly identical to the γ-evaluation[6]. It utilizes continuous "acceptance tubes" around each reference dataset instead of the "acceptance ellipsoids" around each reference point. Much like the γ-comparison, the comparison point agrees with the reference point if it falls within the acceptance criterion of the tube. A χ-comparison uses both the dose gradient of the reference dataset to determine the size of the "acceptance tube" and the dose difference of the full dataset, i.e.,

$$\chi = \frac{D_c(\boldsymbol{r}) - D_r(\boldsymbol{r})}{\sqrt{\Delta D_M^2 + \Delta d_M^2 \cdot \|\nabla D_r\|^2}} \qquad [8.28]$$

The comparison dataset agrees with the reference dataset at a particular point if $\chi < 1$.

There are only slight differences in the results of a γ and χ-evaluation. A χ-comparison will calculate more passing voxels within a high dose-gradient region than the same region analyzed with a γ-comparison. The χ-comparison, aside from its reduced calculation time, does have the advantage of determining the sign of the dose difference (under-predicted or over-predicted) while the γ-comparison cannot. Both have the disadvantage of being susceptible to noise in the reference datasets, potentially producing inaccurate results[7,8] specifically in the high dose-gradient regions of a χ-comparison. Therefore, the reference dataset should be chosen carefully and is usually the theoretically predicted dataset, which has no image noise or artefacts.

There are numerous literature discussing the validity of using a γ or χ-evaluation as a reliable comparative metric. There has also been much literature discussing the optimal acceptable criterion, which can be derived via the radiobiological TCP and NTCP models[9]. Conventionally, a 3% dose difference and 3mm DTA are generally accepted as "good enough". Due to the increased complexity of today's radiotherapy treatments, some studies suggest a more stringent criteria may be required, specifically for VMAT quality assurance testing[10,11]. With improvements in MLC technologies, smaller leaf sizes and faster leaf speeds, as well as the introduction of small field-high dose radiation therapy (i.e., SBRT) the current 3%/3mm analysis may not be robust enough for linac QA.

8.3 VALIDATION OF THE CCMB COLLPASED CONE CONVOLUTION ALGORITHM

Previous work by our group involved dose reconstructions in simple homogeneous media such as water cube phantoms and prostate patients. While validating the CCMB model for more complex disease sites, such as spine and lung, dose errors approaching 5% when comparing to the Eclipse TPS calculated dose distribution were discovered. This prompted an in-depth analysis of our implemented dose calculation algorithm which is based on the work of Ahnesjö's collapsed cone convolution (CCC)[12]. This work was published in the peer-reviewed journal Medical Physics[13].

In general, the collapsed cone convolution method uses an analytical kernel represented by a set of cones, the energy deposited in which is collapsed onto a rayline and distributed respectively to any intersecting voxels defined in the calculating volume. One can choose the number of cones to calculate per voxel and although more cones would give greater accuracy they also increase calculation time. For this thesis, an optimized cone number of 160 was determined to give the best calculation results. More than 160 cones produced no increase in accuracy. Furthermore, Ahnesjö's approach requires both the physical density and relative (to water) electron density as opposed to Eclipse which requires just the relative electron density. The ratios of physical to relative electron densities are 1.01-1.05 for lung and 1.06-1.08 for bone. Our in-house CCC algorithm achieves a more accurate dose reconstruction in heterogeneous media when both densities are incorporated.

Two corrections were implemented into our dose reconstruction code: 1) the calibration curve data of the relative electron density as a function of Hounsfield Units (HU) from Eclipse was added to our code. This ensured that our model's conversion of HU to relative electron density was the same as Eclipse's. 2) Both the relative electron density and physical density data were incorporated into our CCC calculation as opposed to assuming the physical density was the same as the electron density which had been done previously.

In order to validate our CCC implementation a comparison of central axis depth dose curves calculated by our CCC implementation and an EGSnrc Monte Carlo calculation to an Ahnesjö's lung-like phantom (described in reference 12) was performed. The phantom was constructed precisely using exact density and thickness values from the manuscript. A 6 MV 2300ix linac modeled beam was simulated in BEAMnrc for varying square field sizes. The dose distribution in the Ahnesjö phantom was calculated using DOSXYZ. The AAA result was calculated using the same phantom imported into the Eclipse TPS v.10. Results for the 5x5 cm^2 and 10x10 cm^2 fields are given below in the Fig. 8.4 and 8.5 respectively.

In comparison to Ahnesjö's results on the same phantom[12] our CCC results were virtually identical (within 0.5%, except for bone-tissue boundaries which were within 1%). Furthermore, the comparison with the Monte Carlo calculation verified its accuracy. There were some slightly larger over-predictions by CCC in bone, most likely due to the different approaches used in modeling the 6 MV linac beam by Ahnesjö[12], as well as the orientation of cones chosen. Overall, the results proved that our CCC implementation was correct and more accurate than Eclipse's AAA.

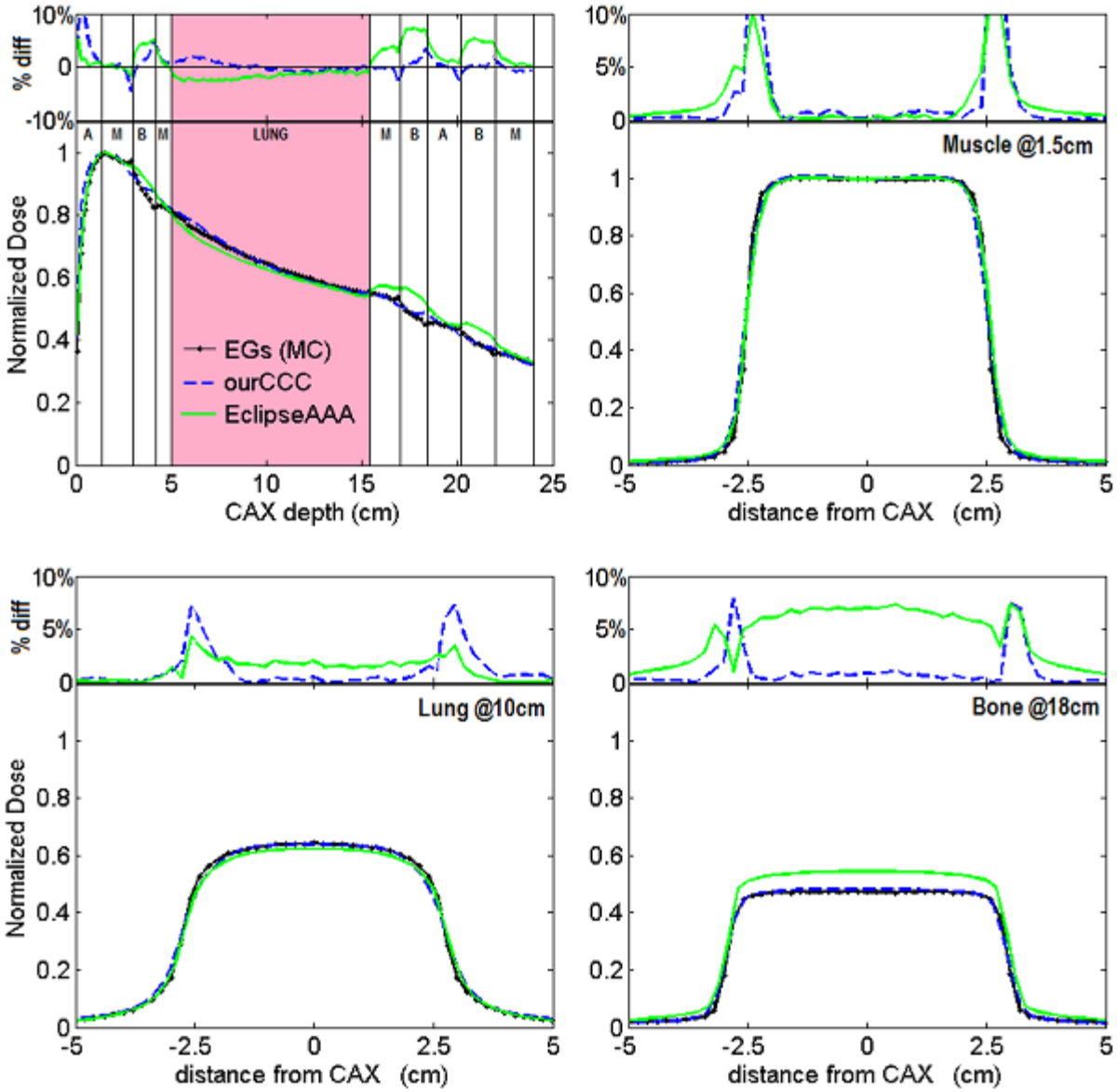

Fig. 8.4 [<u>CCC vs AAA for 5x5 cm^2 Field</u>]: Central axis (CAX) depth dose data for a 5x5 cm^2 6 MV beam delivered to the Ahnesjö lung phantom (top left). Central axis lateral dose profiles for 1.5 cm (top right), 10 cm (bottom left), and 18 cm (bottom right). Percentage differences between both AAA and our CCC with Monte Carlo are given in subplots above each figure respectively (absolute values for the lateral profiles). All show very good agreement between our implemented CCC (blue dash) and Monte Carlo (black dots), specifically within the beam field. They also highlight Eclipse's AAA (green solid) under prediction of dose within the lung and the over prediction of dose in tissue exiting the lung, specifically in bone (A-adipose, M-skeletal muscle, and B-cortical bone).

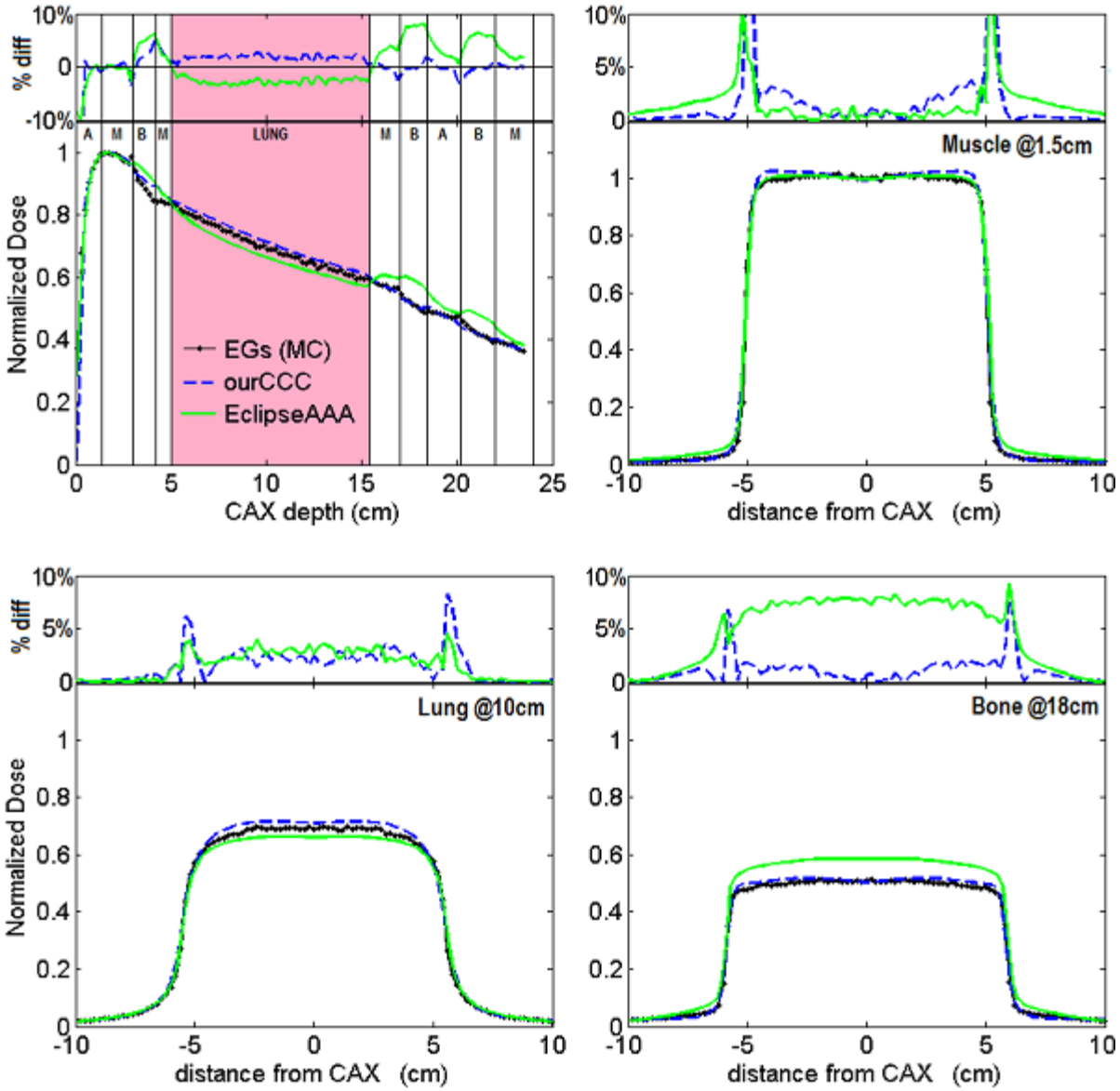

Fig. 8.5 [<u>CCC vs AAA for 10x10 cm^2 Field</u>]: Central axis (CAX) depth dose data for a 10x10 cm^2 6 MV beam delivered to the Ahnesjö lung phantom (top left). Central axis lateral dose profiles for 1.5 cm (top right), 10 cm (bottom left), and 18 cm (bottom right). Percentage differences between both AAA and our CCC with Monte Carlo are given in subplots above each figure respectively (absolute values for the lateral profiles). All show very good agreement between our implemented CCC (blue dash) and Monte Carlo (black dots) while also highlighting Eclipse's AAA (green solid) under prediction of dose within the lung and the over prediction of dose in tissue exiting the lung with respect to our CCC, specifically in bone (A-adipose, M-skeletal muscle, and B-cortical bone).

Differences between AAA and CCC within the lung, bone, and in tissues on the distal side of the lung explain why the spine and lung χ-comparison results with Eclipse (see Chapter 5) had lower than 90% pass rates. Those specific plans had beams traversing through large volumes of lung to a target. The differences in dose to lung and dose to tissues exiting lung calculated by CCC and AAA generally increases for larger field sizes (up to 20x20 cm^2) and remained relatively consistent for fields larger than 10x10 cm^2.

After the implementation a better relative electron density calibration curve and correcting our CCC equation to now include both the physical and relative electron densities, χ-comparison pass rates for most plans (as given in Chapter 5) increased, in some cases as high as 5% in the high dose regions. Incorporating both densities into our algorithm greatly improved our χ results specifically for the heterogeneous plans.

REFERENCES

1. Bethe, H., Heitler, W., *On the stopping of fast particles and on the creation of positive electrons*, Proc. Roy. Soc., 1934, **A146**, p.83.
2. Klein, O., Nishina, Y., *Über die Streuung von Strahlung durch freie Elektronen nach der neuen relativistischen Quantendynamik von Dirac*, Z Phys, 1929, **52** (11-12), p. 853-869.
3. Bethe H., and Maximon, L., *Theory of Bremsstrahlung and pair production. I. Differential Cross Section*, Phys Rev, 1954, **93**(4), p.768-784.
4. Van Dyk, J., Barnett, R.B., Cygler, J.E., and Schragge, P.C., *Commissioning and quality assurance of treatment planning computers*, Int J Radiat Oncol Biol Phys, 1993, **26**(2), p. 261-73.
5. Low, D.A., Harms, W.B., Mutic, S., and Purdy, J.A., *A technique for the quantitative evaluation of dose distributions*, Med Phys, 1998, **25**, p.656-61.
6. Bakai, A., Alber, M., and Nusslin, F., *A revision of the gamma-evaluation concept for the comparison of dose distributions*, Phys Med Biol, 2003, **48**(21), p. 3543-53.
7. Low, D.A., and Dempsey, J.F., *Evaluation of the gamma dose distribution comparison method*, Med Phys, 2003, **30**(9), p.2455.

8. Huang, J.Y., Pulliam, K.B., McKenzie, E.M., Followill, D.S., and Kry, S.F., *Effects of spatial resolution and noise on gamma analysis for IMRT QA*, J Appl Clin Med Phys, 2014, **15**(4), p.93-104.
9. Carver, A., Gilmore, M., Riley, S., Uzan, J., Mayles, P., *An analytical approach to acceptance criteria for quality assurance of intensity modulated radiotherapy*, Radiother Oncol, 2011, **100**, p.453-55.
10. Heilemann, G., Poppe, B., and Laub, W., *On the sensitivity of common gamma-index evaluation methods to MLC misalignments in RapidArc quality assurance*, Med Phys, 2013, **40**(3), p.031702.
11. Nelms, B., Jarry, G., Chan, M., Hampton, C., Watanbe, Y., and Feygelman, V., *Rea-world examples of sensitivity failures of the 3%/3mm pass rate metric and published action levels when used in IMRT/VMAT system commissioning*, J Phys: Conf Series, 2013, **444**, p. 012086.
12. Ahnesjo, A., *Collapsed cone convolution of radiant energy for photon dose calculation in heterogeneous media*, Med Phys, 1989, **16**, p.577-592.
13. van Uytven, E., van Beek, T., McCowan, P.M., Chytyk-Praznik, K., Greer, P.B. and McCurdy, B.M., *Validation of a method for in vivo 3D dose reconstruction for IMRT and VMAT treatments using on-treatment EPID images and a model-based forward-calculation algorithm*, Med Phys, 2015, (accepted).

Supplemental references for section 8.1

i) Podgorsak, E., *Radiation Physics for Medical Physicists*, ©2010, Springer-Verlag Berlin Heidelberg.
ii) Attix, F.H., *Introduction to Radiological Physics and Radiation Dosimetry*, ©2004, WILEY-VCH Verlag GmbH & Co. KGaA, Weinheim.

8.4 GLOSSARY

a-Si – amorphous silicon. This is the composition of an electronic portal imaging device's photodiode layer.

Buildup – is considered to be thickness of material required in order to maintain charged particle equilibrium (CPE). CPE is necessary for accurate dose measurement. The buildup region is at depths less than the depth of dose maximum.

χ-Comparison – a comparison calculation of two datasets that is more computationally efficient than a γ-comparison. It based on criteria of percentage dose differences and distances to agreement (DTA). It incorporates dose gradient regions in its calculation as opposed to point-by-point comparisons.

CAX – central axis. The vector connecting the linac target and EPID while intersecting the linac's mechanical isocentre.

CPE – charged particle equilibrium. When the number of charged particles entering a defined irradiated volume are equal to the number of charged particles exiting that same volume. If this is achieved, then the dose delivered to the volume is equal to the collisional kerma.

CT – computed tomography. A diagnostic imaging technique whereby planar patient density data is acquired using kilo-voltage x-rays delivered over multiple 360° arcs. The planes are acquired at a desired thickness and "stacked" together to create a 3D density data set representative of the patient's anatomy.

Cross-plane – One of the two planar axes that is perpendicular to the linac's axis of rotation.

Dark-field – An EPID image which is acquired with no radiation beam on. This corrects the offset signals of individual pixels.

Dose buildup effect – An effect that occurs at depths less than the depth of maximum dose. This is due to secondary electrons being released by photon interactions between the medium's surface and the depth of maximum dose. These higher energy secondary charged particles can then release other charged particles in a cascading effect thus increasing dose deposition until the depth of maximum dose is reached.

DQE – detective quantum efficiency. A metric which determines how efficient an imaging system utilizes incident radiation to form an image. It is a function of the signal-to-noise ratio.

DTA – distance to agreement. A metric used in γ and χ-comparisons which defines the distance that is comparable between two data points.

EHP – equivalent homogeneous phantom. For each ray-line, the thickness of the EHP from source to target is the water equivalent thickness proportional to the patient's heterogeneous CT data.

EPID – electronic portal imaging device. A 2D planar detector which converts incident radiation into grayscale intensity. X-rays are converted to electrons in a copper layer which are then converted to optical photons via a phosphor layer. Amorphous silicon photodiodes detect the visible photons and integrate the charge until they are readout via triggered thin film transistors.

Flood-field – An image captured during irradiation of the whole active area of any diode array detector (i.e., EPID) which is used to correct for sensitivity differences between pixels.

It corrects the raw image by creating a uniform field but in doing so also removes some dosimetric information such as beam horns and off-axis profile shape.

Fraction – term used to define individual radiation treatments of a whole treatment regimen. In general, a radiation treatment regimen has a total prescribed dose which is delivered over separate small dose fractions, usually one fraction per day. This allows time for irradiated normal tissue to heal thus reducing the normal tissue complication probability.

FWHM – full-width at half maximum. A measure of a peaks width at half of its amplitude.

γ (gamma)-evaluation – a comparison calculation of two datasets based on criteria of percentage dose differences and distances to agreement (DTA). This is performed on a point-by-point basis.

Gantry – The section of the linac which houses the x-ray target and field limiting devices (MLCs and jaws). It can rotate a full 360° around the patient.

Gantry angle – the linac's mechanical angle with respect to the central axis of rotation. 0° is pointing towards the floor perpendicularly, 180° is pointing towards the ceiling, 270° (-90°) is to the patient's right, and 90° is to the patient's left.

Hypofractionated – is the practice of higher than conventional doses per fraction delivered over fewer than conventional fractions. For example a conventional treatment is usually 1-2 Gy in 30-40 fractions while a hypofractionated is 4-12 Gy in 1-8 fractions. This aims to create a specific radiobiological effect at the target.

IMRT – Intensity modulated radiation therapy. A treatment technique utilizing 5-9 optimized static gantry angle delivering MLC modulated radiation beams.

In-plane – one of the two planar axes, that is parallel to the linac's axis of rotation.

Linac – linear accelerator. Generally, it refers to a medical linear accelerator operated at energies suitable for clinical therapies.

MU – monitor unit. A measure of how long the x-ray beam is on. A linac is calibrated for a specific beam-on time in order to deliver a specific amount of dose. This is experimentally done during the commissioning or QA of a linac by delivering fields to a water tank and measuring the dose delivered per beam-on time. This is usually calibrated to 1 cGy/MU.

MV – mega-voltage. Used to define the maximum achievable energy within a polyenergetic spectrum of an x-rays. For example, 6 MeV (mega electron volts) electrons incident on a target will produce a continuous 6 MV spectrum of photons each having an energy within the range of 0 to 6 MeV. In general, roughly a third of the maximum photon energy defines the average energy of a linac produced x-ray spectrum.

OAR – organ at risk. The normal tissue and healthy organs which may be complicated by a radiation treatment beam and require delineation from disease tissue at the treatment planning stage.

Open field image – An EPID image acquired during beam-on with no material between the linac head and imager (i.e., no patient, phantom, or couch).

PDD – percentage depth dose. A measure of the normalized dose as a function of depth within a medium.

Phantom – can be a simplistic or complex design of attenuating material used to emulate simple media like water or more complex media like the human body (anthropomorphic).

SBRT – stereotactic body radiation therapy. A modulated fluence treatment delivered using either VMAT or IMRT using a hypofractionated treatment regimen, i.e., larger doses in fewer fractions.

SDD – source to detector distance.

SRS – stereotactic radiosurgery. SRS traditionally was limited to the skull, due to its' rigid anatomy facilitating reproducible and accurate patient positioning, but recently with improved image guidance tools, it has been applied throughout the body (named SBRT).

TERMA – total energy released per unit mass in an irradiated medium. This is primarily due to primary x-ray interactions.

TPS – treatment planning system. Software that facilitates in the creation, customization, and optimization of patient planning for radiation therapies. It can model the predicted dose delivered to a patient in 3D for a specific plan. It requires both information about the linac beam as well as the patient's CT data.

VMAT – volumetric modulated arc therapy. A complex treatment modality involving the modulation of fluence with MLCs during continuous gantry rotation around the patient. Varian's version of VMAT called RapidArc^{TM} (Varian Medical Systems, Palo Alto, CA, USA) and VMAT (Elekta AB, Stockholm, Sweden) involve the simultaneous control of dose rate, gantry speed, and aperture shaping while the treatment gantry rotates about the patient (Elekta VMAT also includes collimator control). Typically, the term VMAT is used to define any modulated arc delivery whether it is by Varian or Elekta linacs.

8.5 PERMISSIONS FOR COPYRIGHTS

The following is a list of permissions for copyrighted material found within the thesis (when accepted by journal).